AMERICAN UNIVERSITY OF BEIRUT

THE EFFECT OF DAM IMPOUNDED WATERS ON RESERVOIR INDUCED SEISMICITY: CASE STUDIES FROM BISRI, QARAOUN, AND MSEILHA DAMS

by

JANA MAZEN BASBOUS

A thesis
submitted in partial fulfillment of the requirements
for the degree of Master of Science
to the Department of Geology
of the Faculty of Arts and Sciences
at the American University of Beirut

Beirut, Lebanon

December 2022

AMERICAN UNIVERSITY OF BEIRUT

THE EFFECT OF DAM IMPOUNDED WATERS ON
RESERVOIR INDUCED SEISMICITY: CASE STUDIES
FROM BISRI, QARAOUN, AND MSEILHA DAMS

by
JANA MAZEN BASBOUS

Approved by:

_____   Signature

Dr. Tony Nemer, Assistant Professor   Advisor
Geology

_____   Signature

Dr. Mohamed Salah, Associate Professor   Member of Committee
Geology

_____   Signature

Dr. Alissar Yehya, Assistant Professor   Member of Committee
Civil and Environmental Engineering

_____   Signature

Dr. Elsa Maalouf, Assistant Professor   Member of Committee
Chemical Engineering and Advanced Energy

Date of thesis defense: December 9, 2022

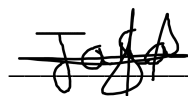# AMERICAN UNIVERSITY OF BEIRUT

THESIS RELEASE FORM

Student Name:
_____Basbous_____Jana_____Mazen_____

             Last   First   Middle

I authorize the American University of Beirut, to: (a) reproduce hard or electronic copies of my thesis; (b) include such copies in the archives and digital repositories of the University; and (c) make freely available such copies to third parties for research or educational purposes:

☐ As of the date of submission

☒ One year from the date of submission of my thesis.

☐ Two years from the date of submission of my thesis.

☐ Three years from the date of submission of my thesis.

_____ December 16, 2022_

Signature   Date

ACKNOWLEDGEMENTS

First and foremost, I would like to express my sincere gratitude to my advisor Dr. Tony Nemer. He supported and guided me throughout every step of the thesis and motivated me to work hard in order to achieve the best possible outcome.

I would also like to say a special thank you to my committee members, Dr. Alissar Yehya and Dr. Elsa Maalouf for their assistance throughout the research, and for the weekly meetings and discussions that guided me and helped me come up with new ideas. Additionally, thank you to my committee member Dr. Mohamed Salah for his constructive feedback and his thoughtful comments and recommendations.

Finally, many thanks to my family and friends for their encouragement and emotional support which was very important to me throughout my journey.

ABSTRACT

OF THE THESIS OF

Jana Mazen Basbous   for   Master of Science

                                                     Major: Geology

Title: The Effect of Dam Impounded Waters on Reservoir Induced Seismicity: Case Studies from Bisri, Qaraoun, and Mseilha Dams

The objective of this thesis is to assess the risk of reservoir induced seismicity due to dam impounded water over or near faults, taking into consideration various effects such as the reservoir-fault location, and the amplitude and period of water-level changes. For this purpose, detailed modeling of different case studies was conducted using COMSOL Multiphysics to estimate the destabilization effect of each reservoir on nearby faults. The coulomb failure stresses (CFS) are plotted along the faults, and their variations are observed in relation to pore pressures, normal, and shear stresses. Positive CFS values indicate destabilization of the faults thus a higher probability for seismicity, while negative values indicate stabilization. On one hand, initial seismicity can be seen as an increase in CFS resulting from the initial impoundment of the reservoir as well as diffusion of pore pressure and can prevail for months or few years. On the other hand, protracted seismicity appears after the initial effect of the reservoir filling has diminished and can persist for decades, which presents a serious risk. As such, reservoir induced seismicity is studied for the planned Bisri reservoir and the existing Qaraoun and Mseilha reservoirs, and a comparison among them is made to understand how the location and size of the reservoir with respect to the nearby fault can lead to different results. This thesis aims at providing an understanding of the risks of building dams and impounding water in certain areas without taking into consideration the presence of faults, so that more informed and safe decisions can be made in choosing future dam locations.

TABLE OF CONTENTS

ILLUSTRATIONS

7

8

TABLES

ABBREVIATIONS

MPa	Megapascal
g	Acceleration due to gravity
ρ	Rock density
z	Depth below surface
CFS	Coulomb Failure Stress
τ	Shear stress
f	Coefficient of friction
σ_n	Normal stress
p	Pore pressure
σ_1	Maximum principal stress
σ_3	Minimum principal stress
θ	Angle between the direction of σ_1 and the normal to the fault surface
asl	Above sea level
m	Meter(s)
km	Kilometer(s)
M	Magnitude
ML	Local magnitude
Ms	Surface wave magnitude
Mw	Moment magnitude
3D	Three dimensional
2D	Two dimensional

CHAPTER 1

INTRODUCTION

Faults are ruptures in the Earth's crust along which earthquakes occur. These structures originally form along plate boundaries due to the relative motion of one plate with respect to another. Whether the plates are moving towards each other, away from each other, or past each other, there will be accumulation of stresses along the plate boundaries, a process known as tectonic loading. At some point, when these stresses overcome the strength of the rocks that host them, the rocks break, and the strain energy is released as an earthquake, which is described by the elastic rebound theory.

Failure along plate boundary faults is quasi-periodic as those faults are subject to continuous stresses along their planes. After stresses accumulate high enough with time, they get released by a series of seismic events making the hosting faults active. In addition, faults away from plate boundaries also exist. This is due to stresses that can load regions at large distances from the plate boundaries, which can cause ruptures along "intracontinental" faults (e.g. Liu et al., 2011). Whether faults are intracontinental, along plate boundaries, active, or dormant, when high enough stress is applied on them, they can break and generate earthquakes of varying magnitudes. The importance of understanding the mechanism of fault failure is by emphasizing the fact that such structures are critically stressed, which means that varying the stresses applied on them may lead to large earthquakes (Mulargia and Bizzarri, 2014).

Several anthropogenic activities were found to disturb the background stresses of nearby faults leading to what is known as human induced seismicity (e.g. Doglioni, 2018;

Gupta, 1992; McGarr et al., 2002). The induced seismic events can vary from microseismic events ($M < 3$) to high magnitude earthquakes ($M > 5.5$; e.g. Davies et al., 2013; Gupta and Combs, 1976; Majer et al., 2007).

There are several types of seismicity that fall under the broad term "induced seismicity" which generally refers to earthquakes caused by anthropogenic activities that perturb the natural background stresses (Mulargia and Bizzarri, 2014). When the perturbations are of comparable magnitudes to those of shear stresses capable of causing slip along a fault, the term "induced" is used (McGarr et al., 2002). In this case, large local stresses arising from activities such as hydraulic fracturing or drilling (that creates fractures) induce low magnitude seismic events ($M < 3$) that in general do not present a major threat to humans and properties (Mulargia and Bizzarri, 2014). However, "triggered" seismicity is associated with small magnitude stresses that build up over time until they become high enough to cause slip and produce large earthquakes ($M > 5.5$; McGarr et al., 2002). Among the human activities causing such incremental stress changes is the construction of dams and the impoundment of water behind them, which has been linked largely to a phenomenon known as "reservoir induced seismicity" (RIS). Although it should be referred to as "reservoir triggered seismicity" (RTS; Gupta, 2021), for simplicity and following the convention of the Committee on Induced Seismicity Potential (Hitzman, 2013), the general word "induced" will be used throughout this thesis instead of "triggered" (e.g. Gupta, 1992; Gupta and Combs, 1976; Kuang et al., 2022; Pavlin and Langston, 1983; Ramasamy et al., 2019; Talwani, 1997; Talwani and Acree, 1984).

The Human-Induced Earthquake Database (HiQuake) is the most up-to-date database that combines all documented cases of triggered and induced seismicity around

14

the world and it is available at www.inducedearthquakes.org (HiQuake, 2022). Last updated on 11 June 2022, HiQuake contains 1235 projects reported to have caused seismic events. According to the analysis of Wilson et al. (2017) of the available HiQuake database, water impoundment behind dams has been found to be among the most common activities associated with induced seismicity: the number of earthquake sequences related to hydraulic fracturing constitutes 33% of human induced seismicity cases, followed by mining at 25%, and water reservoir impoundment at 15% (Appendix I). In effect, 191 cases of reservoir induced seismicity have been reported, of which the largest and most destructive seismic event is the M_w 7.9 Wenchuan earthquake that occurred in 2008 after the impoundment of the Zipingpu reservoir in China (Ge et al., 2009).

In Lebanon, the growth of the population has increased the demand for fresh water, and the National Water Sector Strategy (NWSS) was launched by the Lebanese government in an attempt to provide a sustainable water supply (Haidar et al., 2022). Dams and artificial lakes have been proposed by the NWSS, and they aim at storing the surplus in water for use when needed. One of the planned dams is the Bisri dam that is proposed to be constructed in the Bisri valley. That area is proved to be critical as one active fault is present directly beneath the would-be impounded water of the future lake, intersecting another major active fault (the Roum fault) nearly one km away from the dam site (Nemer, 2019).

The objective of this thesis is to shed light on the importance of assessing the risk of induced seismicity before proceeding with the dam projects in Lebanon, especially in areas with high seismic potential and critical geological conditions where active faults are present. As such, the case of the Bisri dam is studied as it fits the criteria for reservoir-induced seismicity, as well as two other cases: the Quaraoun and the Mseilha dams.

CHAPTER 2

GEOLOGICAL SETTING

The Dead Sea Transform Fault (DSTF) is a 1000-km nearly north-south striking plate boundary separating the Arabian and African plates (Figure 1a). It has a left-lateral strike-slip movement whereby 105 km of displacement has been documented along its southern section (Freund et al., 1970). The DSTF forms a restraining bend that trends NNE in Lebanon where the plate boundary splits into five major faults: the Yammouneh Fault, Roum Fault, Serghaya Fault, Rachaya Fault, and Hasbaya Fault (e.g. Khair et al., 1993; Figure 1b). The so-called Lebanese Restraining Bend (LRB) has caused mainly transpressional movements that gave rise to the different geomorphological features in Lebanon including two mountain ranges, Mount Lebanon to the west and Anti-Lebanon to the East, separated by the Beqaa Valley (Beydoun, 1977; Dubertret, 1955; Khair et al., 1993). In addition, throughout history the LRB has been the site of several large-magnitude earthquakes that affected the eastern Mediterranean region with long recurrence periods (e.g. Khair, 2001).

2.1. Major faults and historical seismicity in Lebanon

The Yammouneh Fault is the main branch of the DSTF along which most of the left-lateral slip is accommodated within the LRB (Nemer et al., 2008a; Figure 1). Precisely, 10 km of displacement have been documented along this active fault (Hancock and Atiya, 1979), with a slip rate of about 5 mm/year (Nemer et al., 2008b). Seven fault-
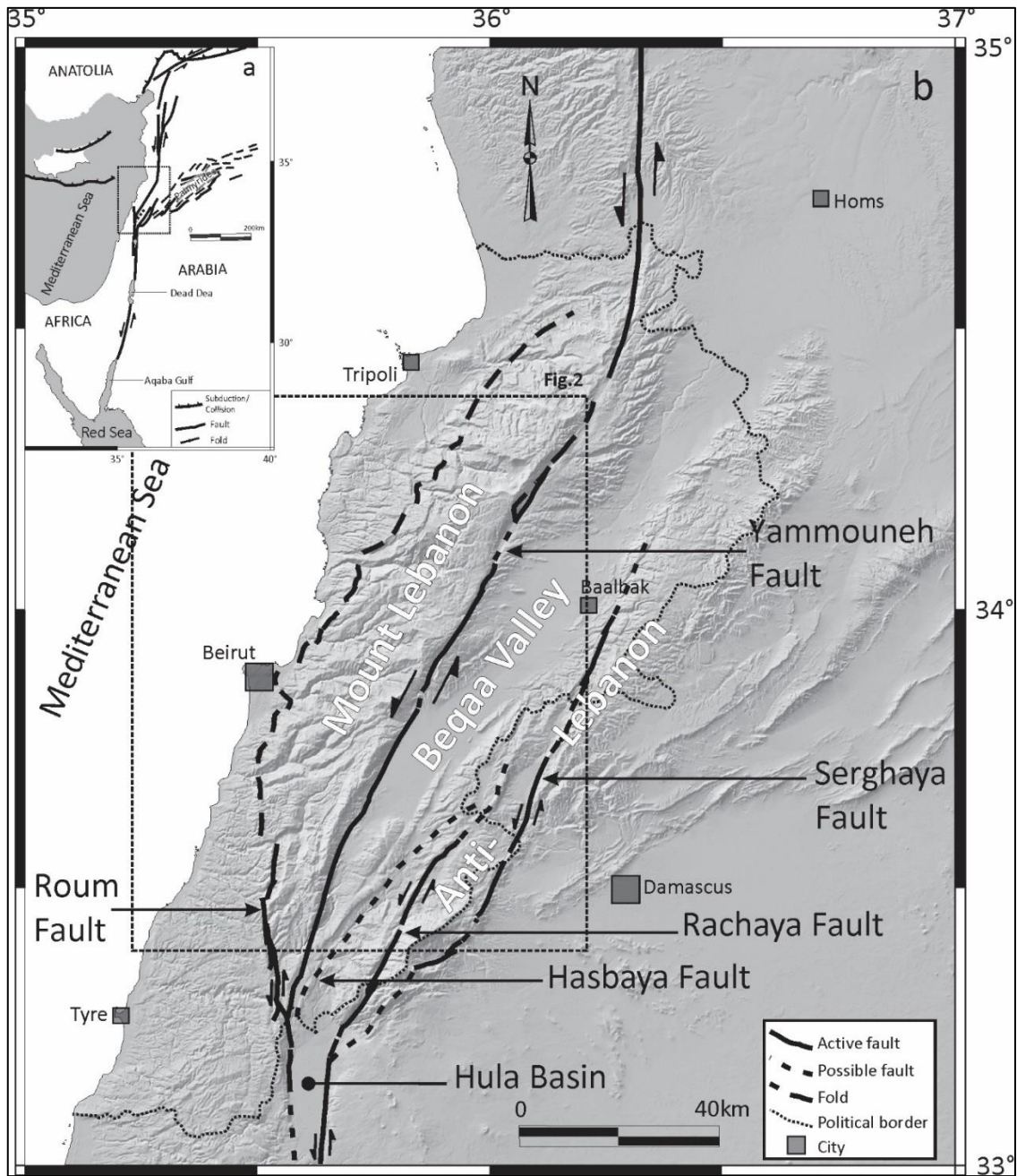
Figure 1. (a) Arabia and Africa separated by The Dead Sea Transform Fault. (b) Shuttle Radar Topography Mission 90-m-resolution digital elevation model of the Lebanese Restraining Bend showing the main units and structures: Hula basin, Hasbaya Fault, Rachaya Fault, Roum Fault, Serghaya Fault, and Yammouneh Fault. The box delineates the location of Figure 2. Modified from Nemer (2019).

related basins are displayed along the strike of the Yammouneh Fault. These basins seem

to be actively evolving, whereby five faulting events have occurred during the past 4500

years (Nemer et al., 2008a). The last large earthquake that was documented to have taken place along the Yammouneh Fault is the M = 7.6 event that occurred on May 20, 1202 (Nemer et al., 2008a).

The Rachaya and Serghaya Faults extend for 45 km and 100 km, respectively, along the western and eastern flanks of Anti-Lebanon Range (Figure 1b). Gomez et al. (2003) studied the movement along the Serghaya Fault in the Holocene period. The main conclusions they came up with are as follows: (1) the motion along this fault takes up to 25% of the slip along the DSTF with a slip rate of about 1.4 mm/year; (2) five rupturing events, mainly involving left-lateral displacements with an average of 2 m per event, were associated with the Serghaya Fault and took place during the past 6500 years; (3) the historical seismicity of this fault suggests that it is a potential source for earthquakes with magnitudes larger than 7 and a recurrence period of 1300 years (Gomez et al., 2003). Nemer et al. (2008b) conducted geomorphologic and paleoseismologic investigations on both the Rachaya and Serghaya Faults. The conclusions of their study are as follows: (1) the two faults are active and the sources of 2 large magnitude earthquakes (Ms = 6.6 and 7.4) that took place in 1759 causing extensive damage; (2) the two structures may be interconnected where the slip on one fault could trigger slip on the other; (3) for any seismic hazard assessment in the region, this fault system must be taken into consideration due to its high seismogenic potential (Nemer et al., 2008b).

The Hasbaya Fault is a 50 km fault branch that extends along the southern margin of Mount Lebanon and Anti-Lebanon chains. No evidence of tectonic activity or major faulting events is apparent along this fault, which suggests that it is not active and not a source of seismic hazard within the LRB (Nemer and Meghraoui, 2020).

The Roum Fault extends for about 35 km from north of the Hula basin to the Awali (Bisri) river. It is mainly a strike-slip fault that displays both horizontal left-lateral movement and some vertical movement (Nemer and Meghraoui, 2006). This fault was the source of the 1 January 1837 (M = 7.1) earthquake, and the 16 March 1956 (M = 5.8) earthquake. With a slip rate of 0.86-1.05 mm/year, the displacement along this fault accommodates about 14% of the plate boundary motion within the LRB (Nemer and Meghraoui, 2006). The Roum Fault is obviously an active fault, and its recurrence rate of moderate seismic events is around 40-50 years (Khair, 2001).

2.2. Geology of the study areas

In this thesis, three dams are studied, namely the Bisri dam, the Qaraoun dam and the Mseilha dam. The known and well documented stratigraphic units present at each dam location, as well as the nearby faults, are described in this section (Figure 2).

2.2.1. The Bisri dam (Bisri Valley)

The proposed Bisri dam is located on the Bisri River that is formed by the Barouk River from the north and merging with Aaray River from the south (Figure 2). The exposed stratigraphic section in this area is comprised of the Cretaceous formations, namely the clastic fine grained Chouf Formation (C1) that is the most widely spread, along with the Abieh (C2a), Mdeirej (C2b), Hammana (C3) and Sannine (C4) formations forming interbedded limestones and marls.
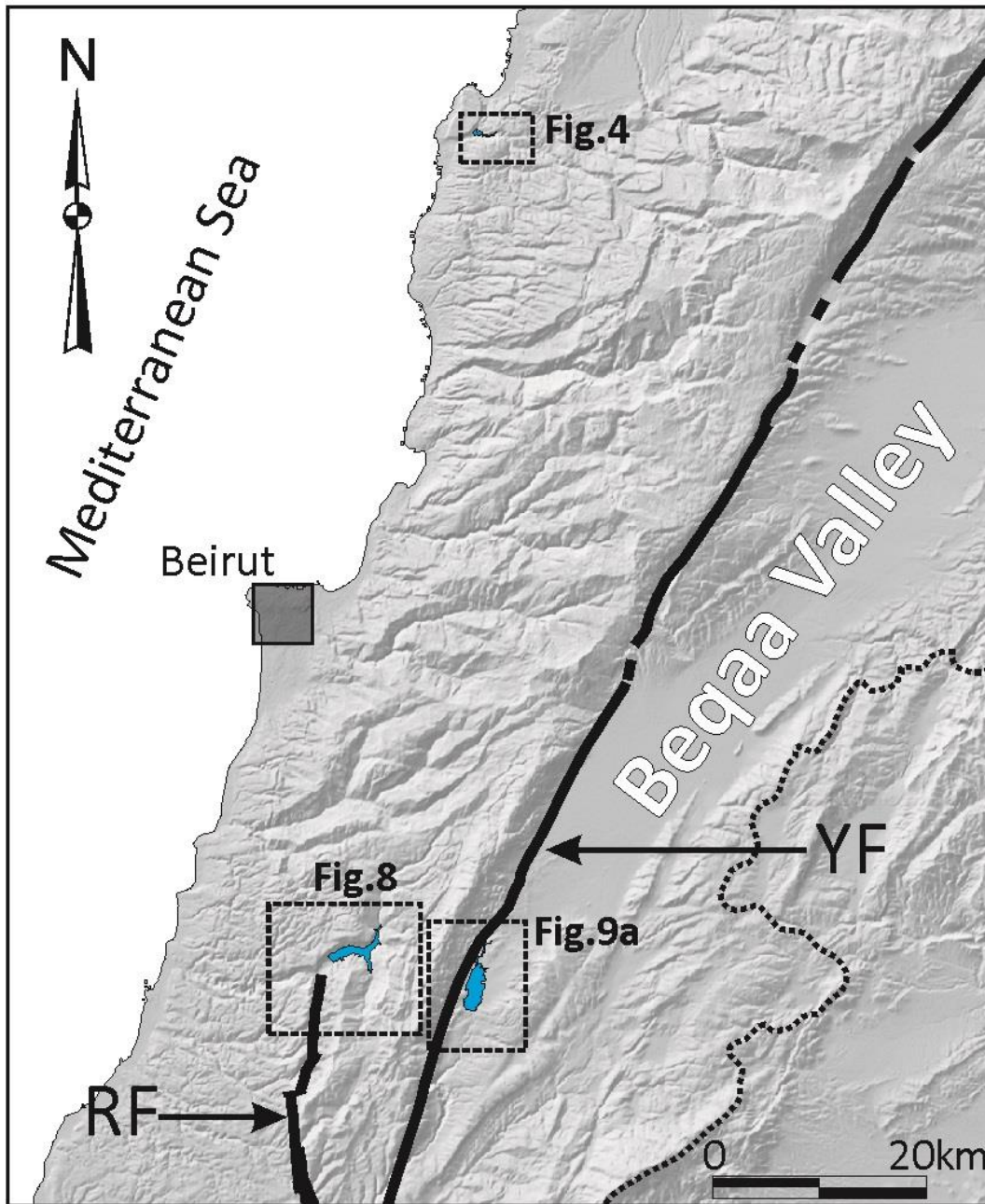
Figure 2. Shuttle Radar Topography Mission 90-m-resolution digital elevation model showing the location of the Bisri dam (Figure 8), the Qaraoun dam (Figure 9a), and the Mseilha dam (Figure 4). Refer to Figure 1 for the legend. Modified from Nemer (2019).

The Jurassic formations are exposed in limited parts of the area shown in Fig. 2 of Nemer (2019), and they consist of the Bikfaya (J6) and Bhannes (J5) formations consisting mainly of micritic limestone, and the Kesrouane Formation (J4) formed of cliff

forming limestones and dolostones. The exposed limestone rocks are found to be highly fractured and karstified (Council for Development and Reconstruction, 2014).

The geology of the Bisri Valley suggests the presence of the Bisri Fault that was validated by a geophysical electrical resistivity survey as reported in Nemer (2019). The Bisri Fault is not a major fault, but it is interconnected with the Roum Fault through block faulting, which makes it active as any displacement along the Roum Fault will physically lead to displacement along the Bisri Fault and vice versa (Nemer, 2019; Figure 3). The epicenter of the 16 March 1956 (M = 5.8) occurred in the area of interconnection of the two faults, which makes it a geologically complex area with a high and critical seismic hazard (Nemer, 2019).
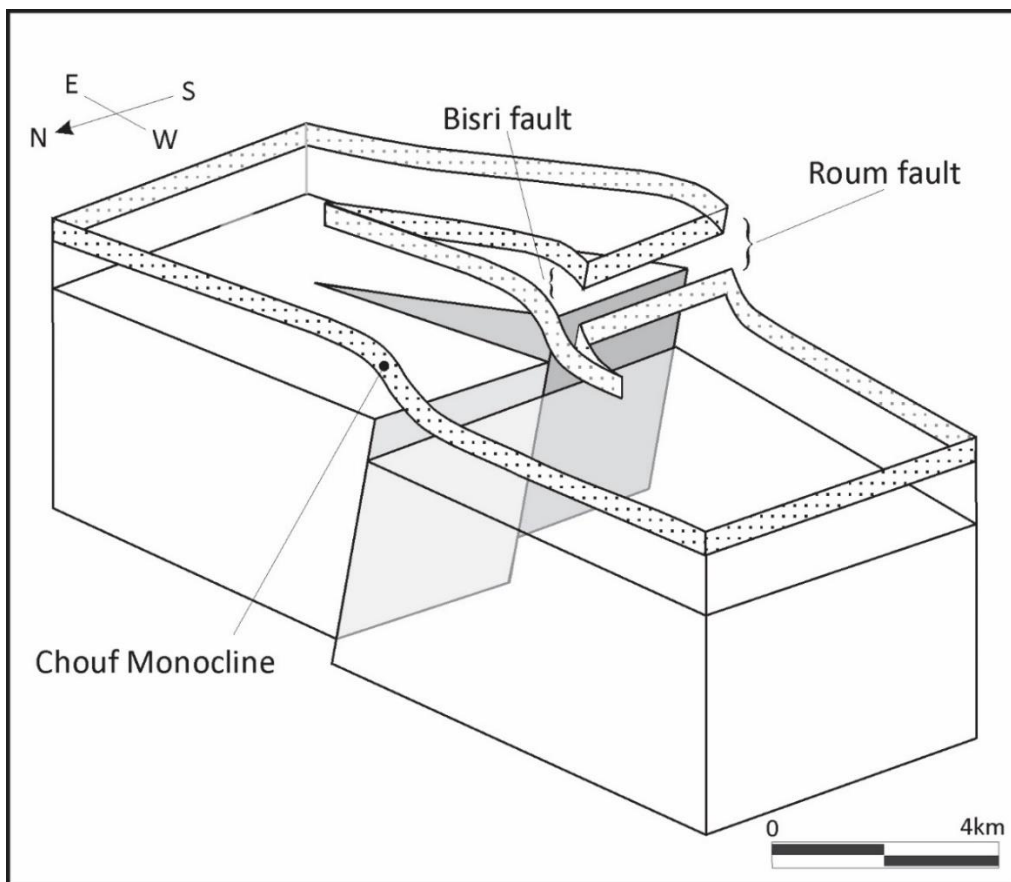
Figure 3. Schematic representation of the 3 dimentional relationship between the Roum Fault and the Bisri Fault. Modified from Nemer (2019).

21

2.2.2. The Qaraoun dam (Beqaa Valley)

The Qaraoun dam was built in the southwest of the Beqaa Valley, Lebanon (Figure 2). The exposed geologic formations in the area display a great offset due to the Yammouneh Fault that is located at approximately 2.4 km west of the Qaraoun Lake. To the west of the fault, the karstic limestones of the Kesrouane Formation are exposed, and adjacent to it to the east of the fault, the Mdeirej Formation is mainly exposed.

2.2.3. The Mseilha dam (Batroun area)

The Mseilha dam was built downstream of Nahr El-Jawz in the Batroun area, Lebanon (Figure 2). The exposed stratigraphic section at the location of the Mseilha dam consists of 3 Cretaceous formations: The Sannine Formation (mentioned above), the Maameltain Formation formed of marls and marly limestones, and the Chekka Formation formed of chalks and marly chalks.

The Batroun Fault limits the southern edge of the dam site and reservoir, where part of the dam directly overlies part of the fault's damage zone (Figure 4). This fault is a dextral strike-slip fault extending for 46 km from offshore Batroun to the Yammouneh Fault. 2 low magnitude seismic events ($2.5 < M < 3.5$) occurred along the fault zone (year not available), and an earthquake of magnitude 3.4 occurred in 1992 at a distance of 3 km north from the fault, suggesting that the fault is active (Gedeon, 1999).

Figure 4. Arial view of the Mseilha dam reservoir and the Batroun Fault (blue line) captured from Google Earth in April of 2020 when the dam was filled. The red line represents the location along which the 2D section in Figure 13 was taken.

CHAPTER 3

BACKGROUND OF INDUCED SEISMICITY

In this chapter, a review of all anthropogenic activities causing induced seismicity is presented with an emphasis on reservoir induced seismicity.

3.1. Human induced seismicity

Seismic events can be induced by natural processes such as plate tectonics, snow loading or melting, groundwater loss, the unloading of sediments, or fluid migration in the crust to hypocentral depths (Foulger et al., 2018). However, many anthropogenic activities similar to the ones related to the oil and gas industry, were found to also trigger seismic events, several of which were destructive and threatened the safety of people, properties, and infrastructure. In order to distinguish between natural and induced seismicity, different researchers have performed statistical analyses on special clustering of seismic events, correlated the timing of the events to those of the anthropogenic activities, and compared the present seismicity rate to the historical rate of the corresponding regions (e.g. Keranen and Weingarten (2018) and references therein). With the development and rise in number of industrial projects, the rate of induced seismicity has increased rapidly and become widespread especially since 2008 (Keranen and Weingarten, 2018). Significant seismic events have occurred after 2011, including two Mw 5.0 earthquakes near Prague in Oklahoma that have caused extensive damage to local homes, among many other earthquakes in that region (Keranen and Weingarten, 2018). This notable surge in induced seismic events became a major source of concern and the

subject of many studies that aimed at understanding the mechanism of such seismicity and assessing the risks of undertaking different anthropogenic activities.

Lithostatic pressure, also known as overburden pressure, is defined as $\rho g z$ where ρ is rock density, g is the acceleration due to gravity, and z is depth below surface. As a result, this pressure increases with depth by 23 to 27 MPa per km depending on the overlying rock density. Hydrostatic pressure is related to pore fluid pressure that is opposite to the lithostatic pressure. In any tectonic setting, natural conditions of lithostatic and hydrostatic pressures prevail whereby critically stressed pre-existing faults are stabilized. The different anthropogenic activities can cause incremental stress changes that cause a deviation from the natural lithostatic and hydrostatic conditions (Doglioni, 2018). As such, pre-existing faults and fractures become no longer under stable conditions, and may fail and get reactivated with time.

The coulomb theory states that the change in Coulomb Failure Stress (CFS) associated with earthquake nucleation is

$$\Delta CFS = \Delta \tau + f(\Delta \sigma_n + \Delta p) \qquad (1)$$

where $\Delta \tau$ is the change in the shear stress, f is the coefficient of friction, $\Delta \sigma_n$ is the change in applied normal stress (which is considered positive when tensile), and Δp is the change in pore pressure. A positive change in CFS indicates a high probability for failure, while a negative change in CFS indicates fault stabilization (Figure 5). Therefore, activities that alter the pore pressure, shear stress, and normal stress have the potential to either stabilize pre-existing faults by decreasing the CFS or destabilize them by increasing the CFS. Precisely, increasing the shear stress, decreasing the normal stress, or increasing the pore pressure have the effect of destabilizing faults and increasing CFS.
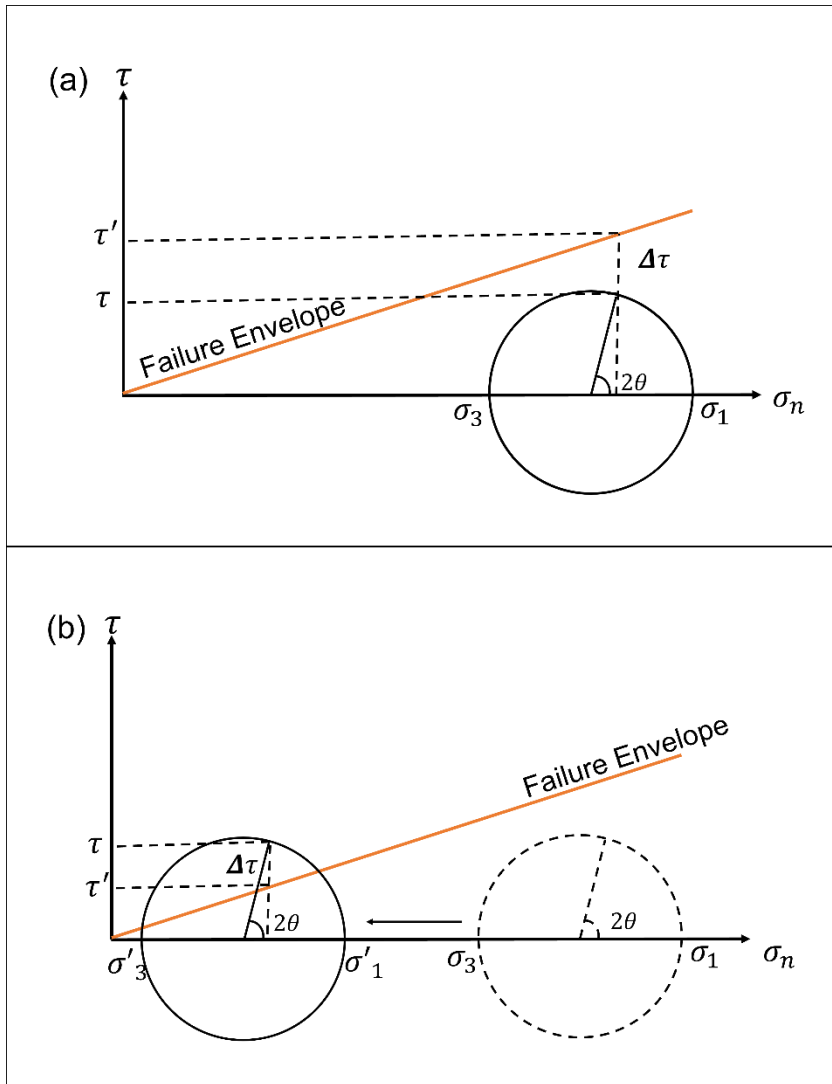
Figure 5. The CFS is represented by the difference in shear stress $\Delta\tau$ between the Mohr circle and the envelope of failure. σ_1 is the maximum principal stress, σ_3 is the minimum principal stress, θ is the angle between the direction of σ_1 and the normal to the fault surface, τ is the shear stress, $\sigma'1$, $\sigma'3$, and τ' are the new maximum principal stress, minimum principal stress, and shear stress after the Mohr circle has shifted; the internal cohesion of the rock is not included since it is negligible for pre-existing faults (Steffen et al., 2015). (a) The CFS is negative indicating that the Mohr circle does not intersect the failure envelope thus no risk of fault slip. (b) The Mohr circle shifted to the left due to a decrease in the effective normal stresses that can be caused by a pore pressure increase. Here the CFS is positive indicating that the Mohr circle intersects the failure envelope revealing a higher probability of failure.

3.1.1. Groundwater extraction induced seismicity

Long-term groundwater pumping can lead to seismic hazard alteration due to the stress changes it causes to the ambient field (González et al., 2012) . These activities can cause an increase in shear stress on critically stressed faults leading to their reactivation (Cueto-felgueroso, 2020). Pressure depletion of the aquifer from groundwater extraction as well as the unloading due to water table drop are the two main mechanisms that cause the destabilization of nearby faults. The decrease of pore pressure in the aquifer as water is extracted causes an increase in the effective normal stress leading to the compression and subsidence of the aquifer. On the contrary, the unloading of the basement for instance due to the drop in water weight in the overlying aquifer causes the basement to expand elastically (Tiwari et al., 2021). The latter case indicates that the tensile stresses in the basement increase, which has a destabilizing effect on the pre-existing basement faults. Therefore, such activities may present a big threat. For instance, the regular low magnitude seismic events that have been recorded in the Aravalli Delhi fold belt in India since the beginning of this century may have been related to the alarming groundwater extraction rate in the surrounding area (Tiwari et al., 2021). In addition, the M = 5.1 earthquake that struck the city of Lorca, Southeast Spain in May of 2011 has been associated with groundwater pumping. This event left hundreds injured, nine deaths and extensive property damage (González et al., 2012).

3.1.2. Injection induced seismicity

Injection of fluids and gases into subsurface formations has been a widely used technique to improve the efficiency of oil and gas wells, as well as to dispose of waste

products such as salt water (Murray and Holland, 2014). However, many seismic events have been detected near injection wells and correlated with them (e.g. Barbour et al., 2017; Davies et al., 2013; Schultz et al., 2020; Schultz and Wang, 2020; Verdon and Stork, 2016). In this section, different fluid injection operations that may induce seismicity are introduced.

3.1.2.1. Hydraulic fracturing

Enhancing the production of oil and gas in some reservoirs calls for unconventional practices such as hydraulic fracturing (also known as fracking) which aims at increasing the permeability to accelerate the flow of hydrocarbons into the well (Peduzzi and Harding, 2013). Compared to other anthropogenic activities, hydraulic fracturing can induce more frequent seismic events of much smaller magnitudes due to the low volume of the fracking fluid; nevertheless, many cases of felt seismicity have been reported especially in Canada, USA, and UK (Davies et al., 2013). This well stimulation method has been adopted since the 1940s, and it involves drilling a vertical well that is deviated to become strata-parallel in the needed formation, and then injecting water, chemicals, and proppants to this formation (Figure 6), a process that is carried out in several stages (Davies et al., 2013). The fluid pressure must surpass both the tensile strength of the rock as well as the in situ compressive stresses in order to create fractures as a means to enhance the connectivity between the pores and increase the surface area connected to the wellbore (Valco and Economides, 2001). The proppant, which is generally sand, serves the purpose of keeping the fractures open. Several mechanisms can be responsible for induced seismicity in this case (Davies et al., 2013):

1- Fracking fluid or formation fluid can flow into a pre-existing fault zone
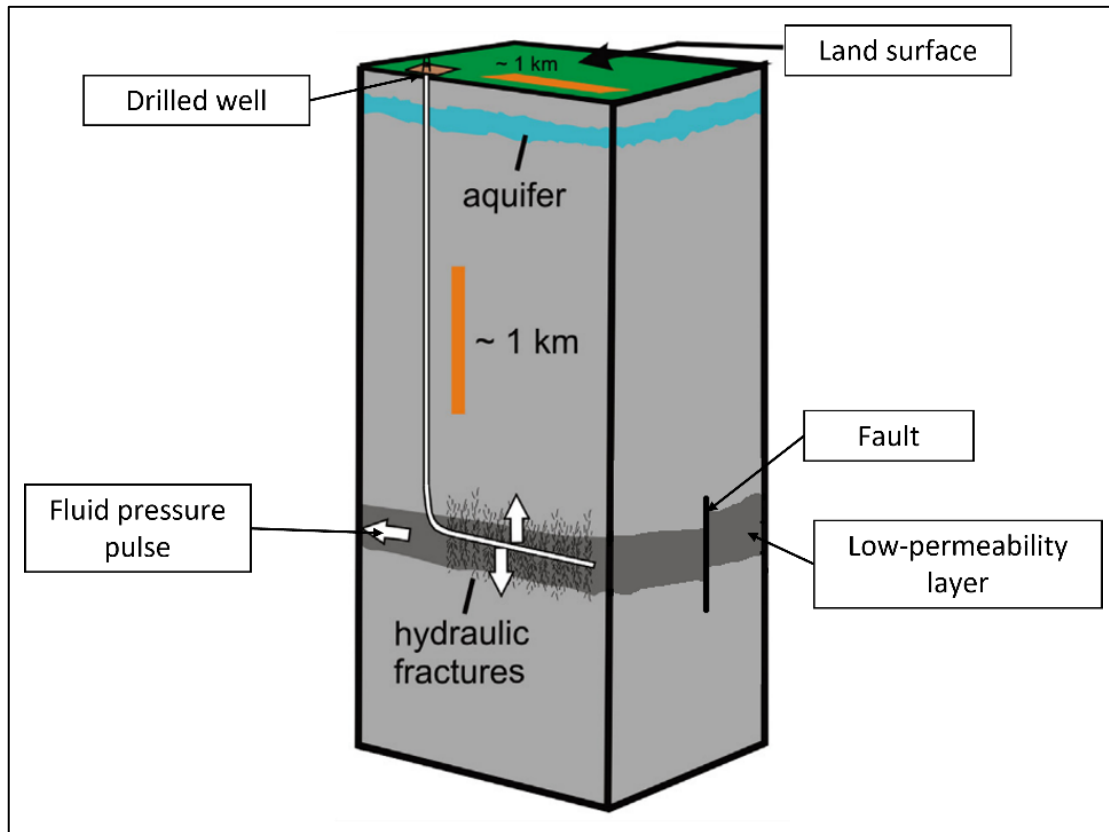
Figure 6. Schema of a vertically drilled well that is deviated horizontally at depth to run parallel to a low-permeability layer. The fluid pressure (represented in white arrows) resulting from the injected material through the well induces hydraulic fractures and can travel to a nearby fault. Modified from (Davies et al., 2013).

2- Fluid can be directly injected if the treatment well intersects a fault or via hydraulic fractures

3- Deformation and stress alterations can be induced due to the poroelastic response of the rocks.

These mechanisms have the effect of destabilizing preferably oriented pre-existing faults. In effect, the increase in the fluid pressure due to diffusion in fault zones and the increase in the tensile normal stresses as a result of the elastic response of the

rock both cause the increase in the shear stresses along faults leading to fault slip. This change in the state of faults may persist and can be observed by continued seismicity months after the stop of fracturing activity (Bao and Eaton, 2016). Of the first reported cases of induced seismicity due to hydraulic fracturing was the ML 3.8 earthquake in the Horn River Basin, Canada that is bordered by the Bovie Fault system to the West. It was one of a series of earthquakes that were induced over two years (Keranen and Weingarten, 2018; Schultz et al., 2020). In addition, the Duvernay Formation in Alberta, Canada has been the subject of multiple studies correlating clusters of induced seismicity with hydraulic fracturing (Bao and Eaton, 2016; Schultz et al., 2020).

3.1.2.2. CO_2 sequestration and injection

The concentration of carbon dioxide in the atmosphere has increased to an alarming level where it has started to cause problems associated with global warming such as ice sheet melting (Firoozabadi and Cheng, 2010). Thermal power plants are the main producers of CO_2 by burning fossil fuels to generate electricity. As a result, practices aiming at inhibiting CO_2 produced from burning of fossil fuels from escaping into the atmosphere are being conducted. In effect, CO_2 can be captured and stored into suitable geologic formations underground, which is known as carbon capture and sequestration (CCS), and it has been used to limit greenhouse gas emissions. However, this process has been found to induce seismicity (Verdon and Stork, 2016). This seismicity not only can affect the wells and infrastructure, but also it can affect the ability of the cap rock to seal the sequestered CO_2, which may fail and cause the escape of the gases back to the surface and into the atmosphere (Vilarrasa et al., 2019). Similarly, CO_2 can be injected into

hydrocarbon reservoirs to enhance oil recovery. In all cases, injected gases into the subsurface increase the pore pressure along faults, which can bring them to instability (Foulger et al., 2018).

3.1.2.3. Saltwater and wastewater disposal

Injecting saltwater or hazardous wastewater, mostly from oil and gas operations, into deep formations in the subsurface has been a low cost alternative to other disposal methods such as landfilling or chemical treatment (Saripalliab et al., 2000). However, this procedure has proven to induce seismic events by reducing the stability of pre-existing faults in the vicinity of the injection wells (e.g. Brudzinski and Kozłowska, 2019; Hincks et al., 2018; Langenbruch and Zoback, 2017; Murray and Holland, 2014). The main mechanism that causes this instability is the diffusion of pore pressure that decreases the effective stresses acting on the fault. In addition, the coupled poroelastic response entails variations in the normal and shear stresses due to the elastic deformation of the solid matrix (Barbour et al., 2017). Wastewater injection has increased the rate of seismicity in Oklahoma and was the cause of many earthquakes since 2009, the most important of which is the 2006 M_w 5.8 Pawnee earthquake (Hincks et al., 2018). This event occurred after an increase in injection rate. Barbour et al. (2017) ran a simulation to understand the cause of the Pawnee earthquake and found that injection at variable rates triggers failure, while injection of the same volume at a steady rate delays the effect as the loading on the fault is gradual.

3.1.2.4. Geothermal heat production

The heat generated from geothermal systems is a renewable environmentally friendly source of energy that has the potential to contribute greatly to the global power supply (Gong et al., 2020). The process of geothermal production requires that the hydrothermal systems be highly permeable and fractured in order for the heat stored in them to be transferred to the surface; however, such systems are not always available or may not be economically feasible (Majer et al., 2007). For that reason, enhanced geothermal systems (EGS) come to place, where deep hot dry rocks are hydraulically fractured in order to create conduits through which water can circulate to transmit heat (Zang et al., 2014). In addition, water can be injected into those stimulated systems via injection wells to further improve the permeability. Both fluid injection and hydraulic fracturing are the causes of EGS- induced seismicity by the same mechanisms of increased pore pressure and decreased effective stresses explained in the previous sections. The larger the injection volume and the longer the injection time, the larger the magnitude of the events. EGS operations were found to induce larger seismic events than regular hydraulic-fracturing for enhanced oil recovery (Zang et al., 2014). Thousands of microseismic events below $M_L = 2$ have been induced because of EGS stimulation; however, a number of felt earthquakes were also documented (Zang et al., 2014). For example, in Basel, Switzerland 3 seismic events were induced, the first $M_L = 2.6$ occurred in 8 December 2006 after the maximum rate of injection was reached, and two other events of $M_L = 2.7$ and $M_L = 3.4$ occurred in the afternoon and evening of the same day after the injection was stopped for safety reasons (Deichmann and Giardini, 2009).

3.1.2.5. Water injection for enhanced oil recovery

Similar to gas injection (section 3.1.2.2 above), water injected into reservoirs to maintain the pressure or to enhance oil recovery has been correlated with elevated seismic activity (Scanlon et al., 2019).

3.1.3. Hydrocarbon production

Apart from the seismicity induced by oil production procedures, such as hydraulic fracturing and wastewater injection, depleting oil fields in itself affects seismicity and can trigger earthquakes. A "graviquake" can occur due to subsidence as a result of fluid extraction that causes voids to contract, and later the overlying layers to collapse, which can cause fault reactivation (Doglioni, 2018). For example, a fluid-extraction induced subsidence that reached 9 m in 30 years was encountered at the Wilmington petroleum field in Los Angeles, California (Segall and Lu, 2015). In addition, Pennington et al. (1986) proposed 3 models explaining how withdrawal of fluids from the subsurface can lead to seismicity:

1- Rocks neighboring the compacting formation become highly stressed and may eventually fail

2- As fluid is extracted, pore pressure drops causing the confining pressure to increase. This leads to the compression of the reservoir rocks, which is accommodated by slip along a bounding fault

3- There can exist active faults in the vicinity of the reservoir which mode of displacement may change from aseismic creep to slip that is seismogenic, due to depressurization.

3.1.4. Mining and mass removal

Seismic events have been associated with mining activities and documented worldwide such as in China, Canada, Germany, and South Africa (e.g. Bischoff et al., 2010; Hasegawa and Gendzwill, 1989; Li et al., 2007; Milev and Spottiswoode, 2002). Temporal and spatial correlations have been noted with an increase in seismicity and mining operations, where clusters of seismic events were observed near active mining sites, and a decrease in seismicity when mining operations cease (Bischoff et al., 2010). Excavation of rock masses related to tunneling and mining can cause the disruption of the stress field in the underground, leading to the reactivation of pre-existing faults and fractures or the formation of new ones (Li et al., 2007). Locally, in the mining area, induced-seismicity is associated with fractures that form at the faces of the openings made to extract ore (Thoms, 1974). In addition, rock burst is a commonly known phenomenon encountered in mining. It is described as a violent and abrupt rock failure event that occurs after the shear strength of the rocks underground is overcome due to the accumulation of stress during excavation (Manchao et al., 2015). These local seismic events are of low to medium magnitude; however, larger events may occur and are related to mining-induced waves that trigger the failure of critically stressed pre-existing faults at some distance away from the mining site (Thoms, 1974). With a similar mechanism, the excavation of rocks from the surface during quarrying has been reported to induce seismicity in 16 cases (Foulger et al., 2018). The largest earthquake associated with mass removal is the 18 June 2003 $M_L = 6.1$ earthquake in Kuzbass, Russia. It was induced by coal mining activities where excavation reached 320 m in depth (Emanov et al., 2014).

3.1.5. Adding mass

Several anthropogenic activities that involve adding mass on or near critically stressed faults can induce seismicity. The added load can increase the shear and normal stresses on the fault plane, thus facilitating slip (Foulger et al., 2018).

3.1.5.1. Erecting tall buildings

Induced seismicity caused by erecting tall buildings is very rare, and it has been observed in a single case documented by Lin (2005). After the construction of the Tapei 101 building, in the Tapei Basin in Taiwan, an increase in seismic activity has been recorded. This building, standing at 508m, is known to be one of the tallest buildings in the world. Upon the completion of the building in 2003, this area, previously considered non-active seismically, was subject to two earthquakes of magnitudes $M = 3.8$ and $M = 3.2$ in October of 2004 and March of 2005, respectively, together with three aftershocks. The occurrence of these seismic events right after the building was constructed, and the location of the epicenters directly below the building lead to the assumption that the Tapei 101 building induced this seismicity. In fact, the earthquakes were associated with a blind normal fault present beneath the building. The vertical load caused by this megastructure might have induced the activation of this fault, especially since the fault is favorably oriented with a dip of 58° (Lin, 2005).

3.1.5.2. Coastal and land gain

Another rare case of induced seismicity is one associated with geoengineering land gain. One reported incident is the 2007 $M = 4.2$ earthquake that took place in Folkestone, Kent, UK which was considered as an aseismic region. Klose (2007) argued

that the artificial accumulation of sand and gravel that has been ongoing since 1806 may have been the trigger of this earthquake. The main mechanism driving failure in this case is the increase in tensile normal stresses and shear stresses, which was estimated at 0.001 MPa to 0.03 MPa along favorably oriented normal and strike-slip faults (Klose, 2007).

3.1.6. Nuclear explosions

Nuclear tests have been associated with induced seismicity as they have caused clear deformation and movement along nearby faults (Foulger et al., 2018). For example, in Amchitka, Alaska a visible displacement of 1 m vertically and 15 cm horizontally on faults up to 8 km in length was caused by nuclear tests (McKeown and Dickey, 1969). The vertical displacement was found to be in the same direction as previous slip caused by natural tectonic activities; the horizontal displacement on the other hand occurred with no previous such movement along the faults. As such, it was interpreted that the additional stress caused by the explosions induced the release of tectonic strain (McKeown and Dickey, 1969).

3.2. Reservoir induced seismicity

Reservoir induced seismicity is a phenomenon that presents a serious risk for the regions near dams. The large volumes of water that can be held behind dams put a very high pressure on the substratum. This pressure can diffuse for several kilometers depending on the properties of the rock layers. In addition, the weight of the water causes changes in the background elastic stresses. This can trigger seismic events in case faults

are present nearby, since such structures are stable under certain stress conditions, and if these conditions are altered, the faults can be reactivated.

In 1935, the first case of reservoir induced seismicity was recorded and documented. It took place after the impoundment of the artificial Lake Mead behind the Hoover dam (Arizona-Nevada, USA), where the water level reached 110 m on average with 15 m of annual fluctuations (Roeloffs, 1988). A peak in seismic events were observed at peak load; however, when the water level remained stable, no change in frequency of seismicity took place. After this instance, multiple cases were recorded, some with high magnitude destructive earthquakes, making this phenomenon a growing interest for researchers after it was found that dams can be potential seismic hazards.

The mechanism associated with fault failure due to the impoundment of water behind dams is related to the added weight of the water as well as to pore pressure diffusion. According to Bell and Nur (1978), impounded reservoirs cause incremental strength changes (ΔS) along fault planes defined by:

$$\Delta S = \mu_f\left(\Delta\sigma_n - \Delta P_p\right) - \Delta\tau \qquad (2)$$

where μ_f is the coefficient of friction along the fault, $\Delta\sigma_n$ the change in normal stress, ΔP_p the change in pore pressure, and $\Delta\tau$ the change is shear stress. Any increase in pore pressure, shear stress, or tensile normal stresses reduces the strength along the fault leading to failure.

Talwani (1997) divided RIS into two categories:

1-   The first category is initial seismicity caused by the instantaneous effect of the water weight as well as the delayed effect of pore pressure that diffuses slowly and builds up over time.

2-   The second category is prolonged seismic activity for many years after impoundment, which is also known as "protracted seismicity".

Concerning the first category, it is related to the elastic stress changes on the fault plane due to the water load. It is associated with the initial filling of the reservoir, or to large water level changes. The highest seismic event typically occurs when the maximum water level is attained or after the water level increases beyond previously reached levels. This type of seismicity prevails for months to few years after which it decreases to background levels as the stress changes caused by the coupled response to initial filling stabilize (Talwani, 1997).

As for the second category, several reservoirs have experienced prolonged seismic activity even tens of years after impoundment. This seismicity is the result of the poroelastic response of the substratum to yearly fluctuations in water level. The mechanism associated with protracted seismicity is largely pore pressure diffusion. It commonly prevails in reservoirs where lake-level changes are large, usually where the fluctuations are a big fraction of the minimum water depth, and where the lag period between minimum and maximum water levels is long (around a year) (Talwani, 1997). It is also highly dependent on the hydraulic properties of the underlying layers (e.g., diffusivity) that control the rate of pore pressure diffusion and the distances it can reach and therefore affect. Another important factor that plays a role in protracted seismicity is the location of the reservoir with respect to nearby existing faults as well as the nature of

these faults (Talwani, 1997). In effect, large reservoir-induced events were typically associated with normal and strike-slip faulting (Roeloffs, 1988; Simpson et al., 1988). In some cases, reservoirs can contribute to stabilizing nearby faults, in other cases they can destabilize them and lead to elevated seismicity (Roeloffs, 1988; Figure 7).
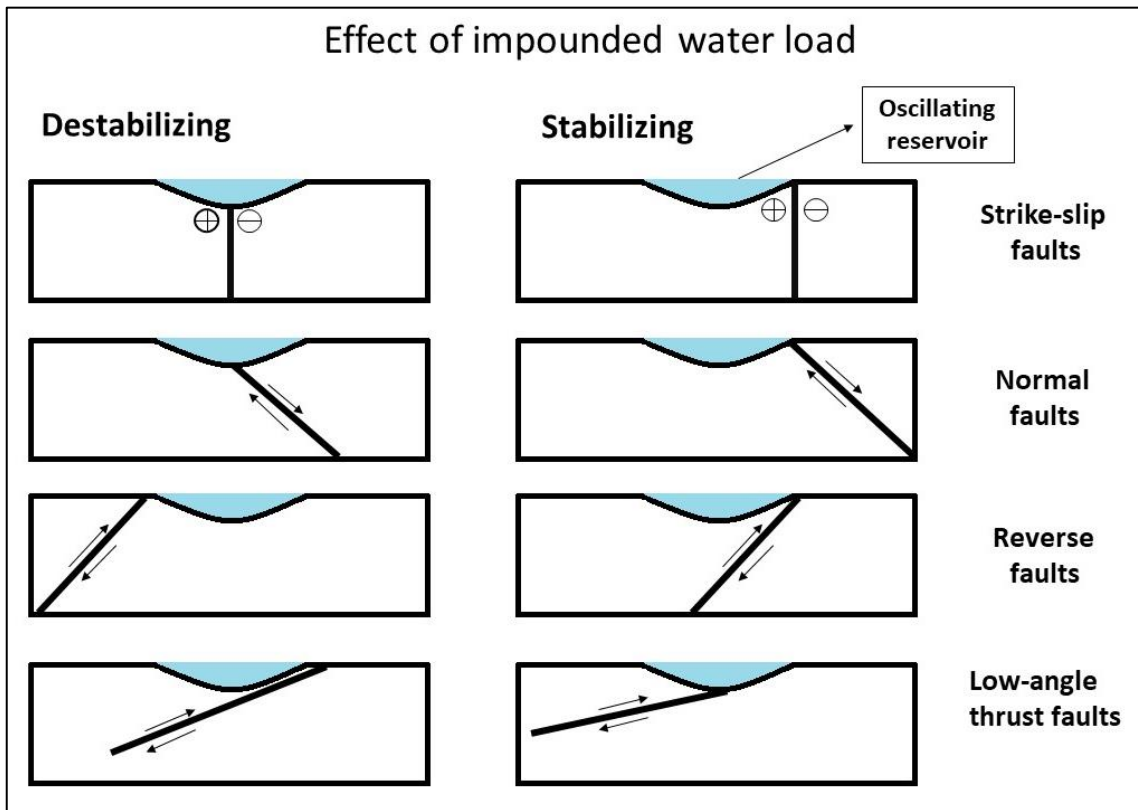
Figure 7. Stabilizing or destabilizing effect of oscillating water-load on nearby fault depending on the position, the nature and the orientation of the faults with respect to the reservoir. Based on Roeloffs (1988) and Talwani (1997).

Some important or recently studied cases of reservoir induced seismicity are presented below:

- Lake Kariba:

Lake Kariba located in southern Africa is known to be one of the largest artificial lakes in the world. It was first impounded in 1958, after which about 2000 tremors were observed (Cough and Gough, 1970). These epicenters were all located in the rift

valley of the middle Zambezi leading to the assumption that the impoundment of that lake has induced the failure of preexisting faults present at that location. 200 of these tremors took place at a proximity to the lake and were associated with the reactivation of a critically stressed fault due to either stress changes or pore pressure increase. On the other hand, 50 tremors recorded at distances between 15 and 65 km away from the lake were attributed to incremental increases in elastic stresses due to the load of the water rather than pore pressure diffusion, since pore pressure cannot reach to such distances (Cough and Gough, 1970).

- Koyna reservoir:

One of the most prominent cases of reservoir induced seismicity is the Koyna dam in India. This region was considered aseismic prior to the construction of the Koyna dam (Gupta and Combs, 1976). Soon after the start of the filling of the reservoir in 1962, an elevated seismic activity was reported, which was attributed to initial seismicity (Talwani, 1997). This seismicity depended on the rate of filling, the maximum water level reached, and the duration for which this level was retained (Gupta and Combs, 1976). The largest earthquake to take place in the region was of magnitude 6.3, and it occurred in 1967. However, there is an ongoing seismicity at the vicinity of the Koyna reservoir, making it a case of protracted seismicity, which is affected primarily by lake level fluctuations (Talwani, 1997). In effect, to date, the seismicity at the Koyna reservoir has not stopped. 22 tremors of magnitudes around 5, 200 tremors of magnitudes around 4, and thousands of smaller events have taken place so far (Gupta, 2022). This case shows the importance of studying the risk for induced seismicity before proceeding with any dam or artificial lake project, since the damage can be prominent and last for decades.

- Xinfengjiang (XFJR) reservoir:

A recent article by Kuang et al. (2022) suggested that the increase in seismicity after the impoundment of the XFJR reservoir, southeast China in 1959 was due to the added water load. As previously mentioned, higher magnitude events can be observed after the water level increases beyond any level reached thus far, and that this is related to initial seismicity. This is clear in the case of the XFJR reservoir, since earthquakes of Ms magnitudes 3.1, 4.3, and 6.1 occurred right after water levels reached 58 m, 81 m, and 110.5 m, respectively. The Ms = 6.1 earthquake damaged the dam itself causing small cracks in the wall (Foulger et al., 2018). The region was also subject to protracted seismicity as induced events are ongoing today, after more than 6 decades. These events include more than 30 earthquakes with magnitudes larger than 4, and thousands of smaller tremors. It is important to note that the geological structure of the area is a key factor for the induced seismicity as it contains multiple fault systems. Stress changes along these critical structures is at the root of all the tremors. A correlation between the earthquakes cycle and water level change cycle suggests that the oscillating water load is what is causing this ongoing seismicity, which agrees with Talwani (1997) on the fact that protracted seismicity is related to yearly fluctuations in water level.

- Zipingpu reservoir:

The largest, most destructive reservoir induced seismic event is the 2008 M = 7.8 Wenchuan earthquake (China) that most probably was caused by the impoundment of the Zinpingpu reservoir in 2005 (Wilson et al., 2017). Ge et al. (2009) studied the stress changes caused by the reservoir in order to understand the mechanism of

occurrence of the earthquake. Coulomb stress changes in the order of 0.01 MPa to 0.05 MPa were estimated along the active critically stressed Longmen Shan Fault. The natural rate of loading on this fault is less than 0.005 MPa/year, and the recurrence rate of an earthquake with a magnitude similar to that of the Wenchuan earthquake is about 2000 years (Ge et al., 2009). The above suggests that the impoundment of the Zipingpu reservoir has accelerated the occurrence of such a big seismic event, since it increased the load applied on the causative fault and brought it to failure earlier than expected.

- Aswan High dam:

The Aswan High dam in Egypt contains the highest volume of water in the world, with a water level of 111 m (Foulger et al., 2018; Gupta, 2021). This dam was impounded in 1964, and the largest corresponding induced earthquake took place in 1981 with $M = 5.7$ (Gupta, 2021). Incremental increases in pore pressure and Coulomb stress on a nearby active fault, the Kalabsha Fault, reaching values of 0.1 MPa at the hypocenter of the $M = 5.7$ earthquake led to the assumption that the Aswan High dam was the trigger (Gupta, 2021). What's uncommon and unique about this dam is that the induced seismic events were particularly deep. The earthquakes occurred at two distinctive zones, one extending from the surface till 10 km, and the other from 15 to 25 km. In fact, the hypocenter of the $M = 5.7$ earthquake was at a depth of 18 km (McGarr et al., 2002).

CHAPTER 4

METHODOLOGY

We built three fully coupled two-dimensional (2D) finite element poroelastic models. One model contains the Bisri Fault and the planned Bisri reservoir, the second model contains the Yammouneh Fault and the Qaraoun dam, and the third model contains the Batroun Fault and the Mseilha dam. We also built a fully coupled three-dimensional (3D) finite element poroelastic model containing the Bisri reservoir, the Bisri Fault, and the Roum Fault. The coupled model simulates the feedback between fluid flow and rock deformation to estimate the change in the overall Coulomb stresses, evaluate the rate of seismicity, and estimate the maximum earthquake magnitude.

4.1. Description of the dam projects

In this section, a description of each dam project is provided including information such as dam location, dimensions, water level, water volume, use of the dam, and date of construction.

4.1.1. The Bisri dam

The Bisri dam project is planned to secure clean water for the Greater Beirut and Mount Lebanon area residents (who account for over 1.6 million people), and to reduce their water expenditure. As such, they would no longer need to use alternative water resources like wells, which will in turn decrease coastal salt-water intrusion and restore

Beirut's groundwater. In addition, the locals will benefit from many projects and new sources of income like ecotourism and others (The World Bank, 2021). The dam is located about 35 km south of central Beirut, and the reservoir is expected to extend about 4 km upstream of the dam axis. Above the dam, the water surface catchment area extends to about 215 km^2. The maximum height of the dam is 73 m, and the length of the reservoir is 6 km with two 2-km branches, and its width is about 1 km (Figure 8). The area to be inundated is around 4.34 km^2 where the expected maximum water level is at 467 m asl, and the minimum water level is at about 420 m asl, with an average storage volume of 125 million m^3 (Council for Development and Reconstruction, 2014).
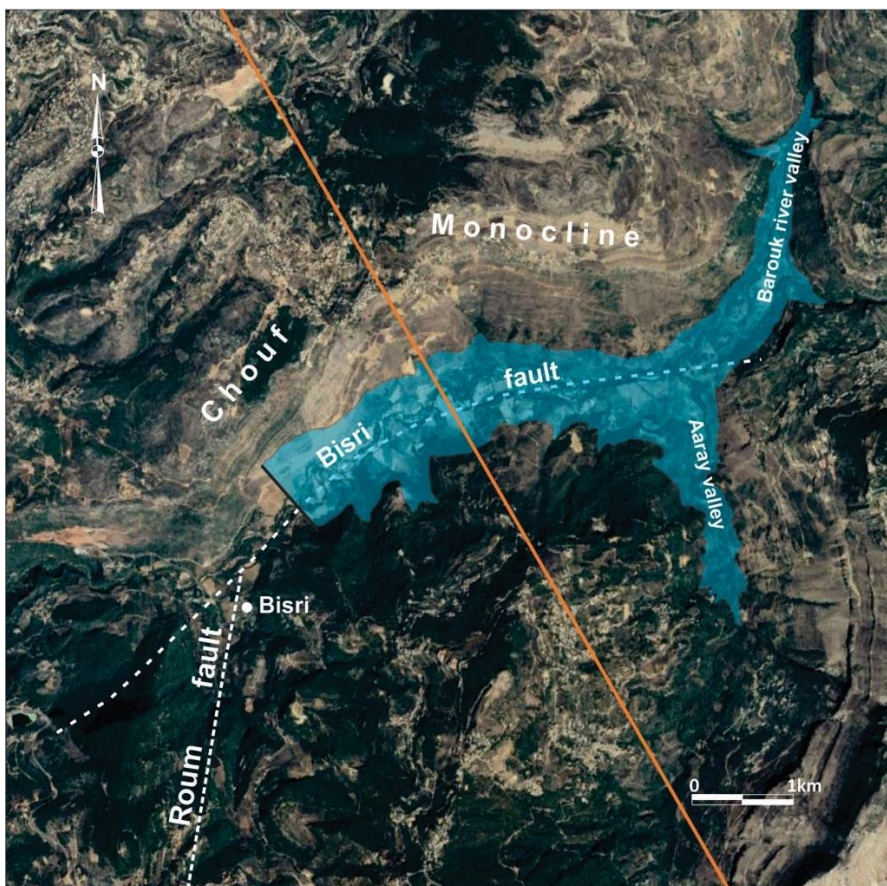
Figure 8. Aerial view of the Bisri Valley showing the proposed Bisri reservoir, as well as the Roum, and Bisri Faults modified from Nemer (2019). The orange line represents the location along which the 2D section in Figure 10 was constructed.

4.1.2. The Qaraoun dam

The Qaraoun dam was built in 1959 at an elevation of about 800 m asl. The maximum water level of the Qaraoun Lake is at 858 m asl with a maximum storage of 222 million m^3, and the minimum water level is at 838 m asl with a minimum storage of 53 million m^3 (The Litani River Authority, 2021). The dam has a length of 1090 m, a width of 162 m, and a height of 60 m (The Litani River Authority, 2021; Figure 9).

4.1.3. The Mseilha dam

The Mseilha dam was built in order to ensure potable water for the residents of Batroun and Koura regions, as well as provide irrigation and industrial waters. The construction of the dam commenced in 2013, and it has a height of 35 m and a length of 400 m, with a storage capacity of 6 million m^3 (Figure 4). The construction was finalized in 2019, and the dam was supposed to start filling up. The maximum water level that can be reached in this dam is around 71.5 m asl (26.5 m of water), which was attained for a short period of time in 2020. However, this lasted for a few days after which water started to leak until the dam was completely empty. The dam was filled again to its full potential in May 2022, but the same scenario re-occurred where water was held for a short time before the dam was emptied. The Ministry of Energy and Water reported that the dam was under testing, which might explain why its reservoir is still empty to date.

4.2. Model Constructions

In this section, we provide a detailed description of how the models were built using COMSOL Multiphysics, including the parameters used and assumptions taken.
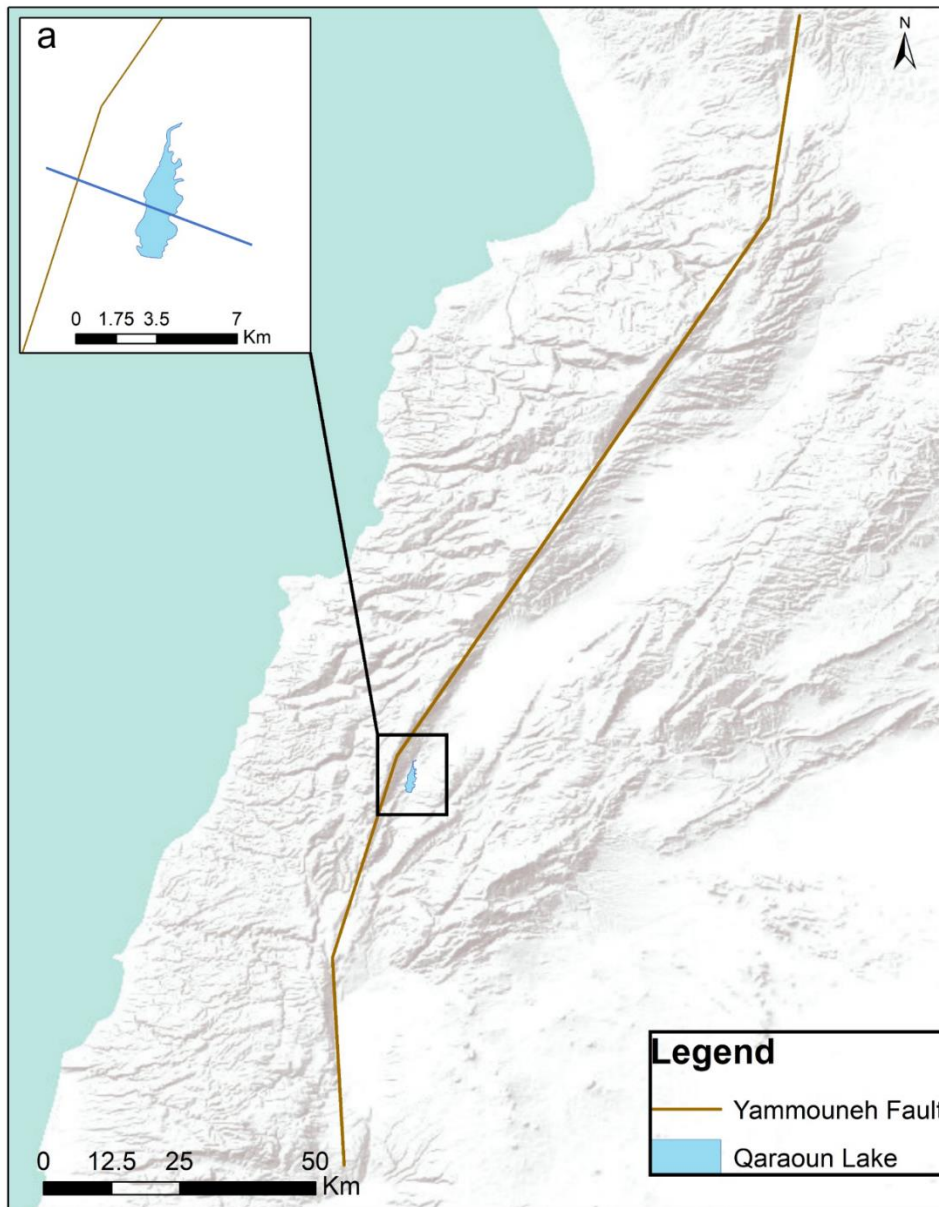
Figure 9. Digital elevation model of Lebanon showing the Yammouneh Fault and the Qaraoun Lake. The blue line in (a) represents the location along which the 2D section in Figure 12 was constructed.

4.2.1. 2D models

The lithologies of the layers below the Kesrouane Formation were taken from the general chronostratigraphic chart of the Levant margin (Nader et al., 2018), and the parameters used were approximated from acoustic and petrophysical investigations done on core samples collected from different exposed formations at several locations in Lebanon (Salah et al., 2020a, b, c, 2018). The parameters for the deep marine siliciclastic rocks were taken from layers with similar lithologies in the Levant Basin (Marlow et al., 2011), and the parameters for the evaporite layers were taken from Jackson and Hudec, (2017). Since no local information were available on such rock types. Fan et al. (2019) divided the layers of the region into caprock, overburden and reservoir rocks having a Biot coefficient between 0.7 and 0.79, and crystalline rocks having a Biot coefficient of 0.44. As such, due to the lack of available information for this model, the Biot coefficient is taken as 0.75 for all the sedimentary layers except for the evaporite layer since it is composed of crystalline rocks where the Biot coefficient is taken as 0.44. The simulation parameters used in our 2D models are gathered in Table 1.

Generally, fault cores are surrounded by high permeability damage zones that are highly deformed and fractured (Mitchell and Faulkner, 2009). This is a plausible assumption for active faults if microcrack healing, which is usually thermally enhanced and fluid-assisted (Yehya and Rice, 2020), did not occur during the inter-seismic cycle (Yang et al., 2021). According to the Council for Development and Reconstruction (2014), fractured and well jointed limestones are present in the vicinity of the proposed dam, which suggests that the Bisri Fault has a damage zone. As for the rocks at the vicinity of the Qaraoun Lake, they are found to be extremely fractured, jointed, and friable, indicating a damage zone that is a few kilometers wide. A limitation of our model is that

the joints and fractures present in the damage zones are not explicitly added, rather, we use average porosity and permeability values, which are taken higher in the damage zones relative to the host rocks. We assume that the cracks within the damage zone partially close when the effective normal stress increases. Therefore, we assume that the permeability of the damage zone decreases with depth. In all the models, the porosity of the damage zone is taken as 18% and the permeability as 2 mD, both decreasing linearly with depth to reach the value of the surrounding host rocks. However, for active faults there could be open fractures along the fault that will locally increase the permeability and enhance diffusion, and further increase the estimated risk of seismicity. In addition, rocks in the damage zone are characterized by a lower Young's modulus than the adjacent country rocks due to higher fracture density (Gudmundsson, 2004; Yehya et al., 2018), therefore, this parameter was decreased by 5 GPa for the damage zone rocks with respect to their corresponding host rocks (Cappa and Rutqvist, 2011; Faulkner et al., 2006; Yehya et al., 2018). The shape of the fault damage zone follows a flower like structure, where the width and fracture density decrease as we go downwards (Ampuero and Mao, 2017; Stefanov and Bakeev, 2015).

After building the 2D models, a sensitivity analysis on the model mesh and the model size are performed. The analysis of the simulation results gives an initial assessment for the risk of induced seismicity associated with the dam project, which is necessary for the safety of the surrounding region.

4.2.1.1. The Bisri 2D model

Figure 10 shows a 2D cross-section including the Bisri Fault, its damage zone, the Bisri reservoir, and the successive lithologic layers mentioned in section 2.2.1. To simulate the oscillating dam reservoir, minimum and maximum pressures are applied at the surface corresponding to 13 m and 60 m water levels, respectively, with a lag time of six months in between (Figure 11).

The pressures are calculated by $p = \rho g h$, where p is the pressure of the water column, ρ is the density of water that is 997 kg/m3, g is the acceleration due to gravity that is 9.8 m/s2, and h is the height of the water column. The dam reservoir is expected to fill up naturally during the rainy season that extends for six months (winter and spring), and the accumulated water is to be used during the dry season over the following six months (summer and fall) (Council for Development and Reconstruction, 2014). Hence, the lag time is taken to reflect this assumption.

4.2.1.2. The Qaraoun 2D model

Figure 12 shows a 2D cross-section including the Yammouneh Fault, its damage zone, the Qaraoun Lake, and the successive lithologic layers mentioned in section 2.2.2. To model the oscillating Qaraoun Lake, the time lag is assumed the same as the Bisri reservoir case, but with minimum and maximum water levels of 38 m and 58 m, respectively.
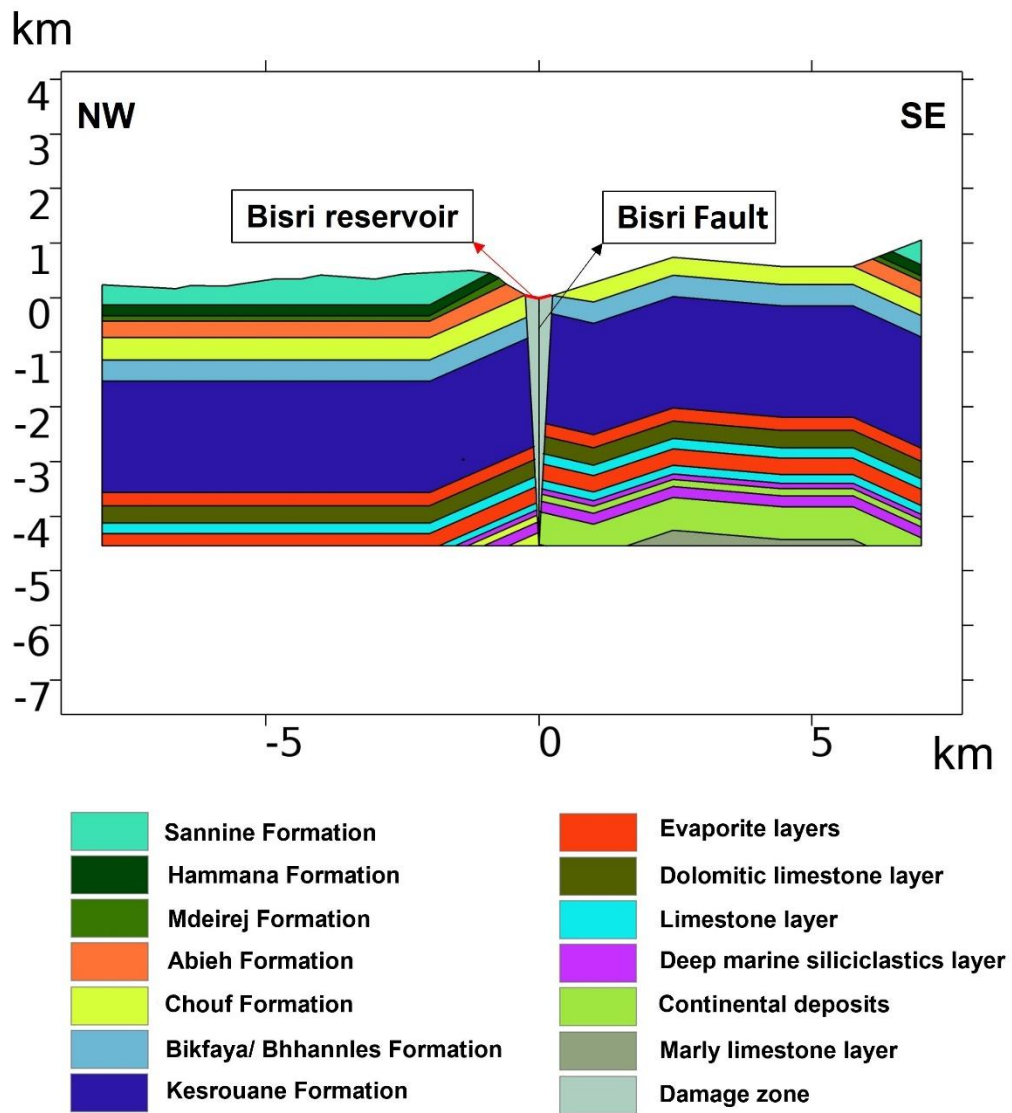
Figure 10. 2D cross-section taken along the orange line in Figure 8, and showing the Bisri Fault, its damage zone, and the adjacent country rocks. The origin is taken at the surface where the Bisri Fault is located so that the negative values on the x-axis indicate the distance Northwest of the Bisri Fault, positive values indicate the distance Southeast of the Bisri Fault, and the negative values on the y-axis indicate the depth below the surface.
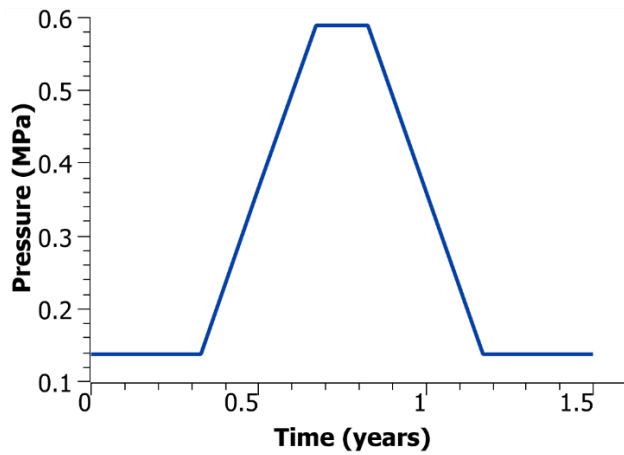
Figure 11. Change of pressure with time representing the oscillating water level of the Bisri reservoir. 1 cycle is shown in this figure and is repeated throughout the entire simulation (60 years).
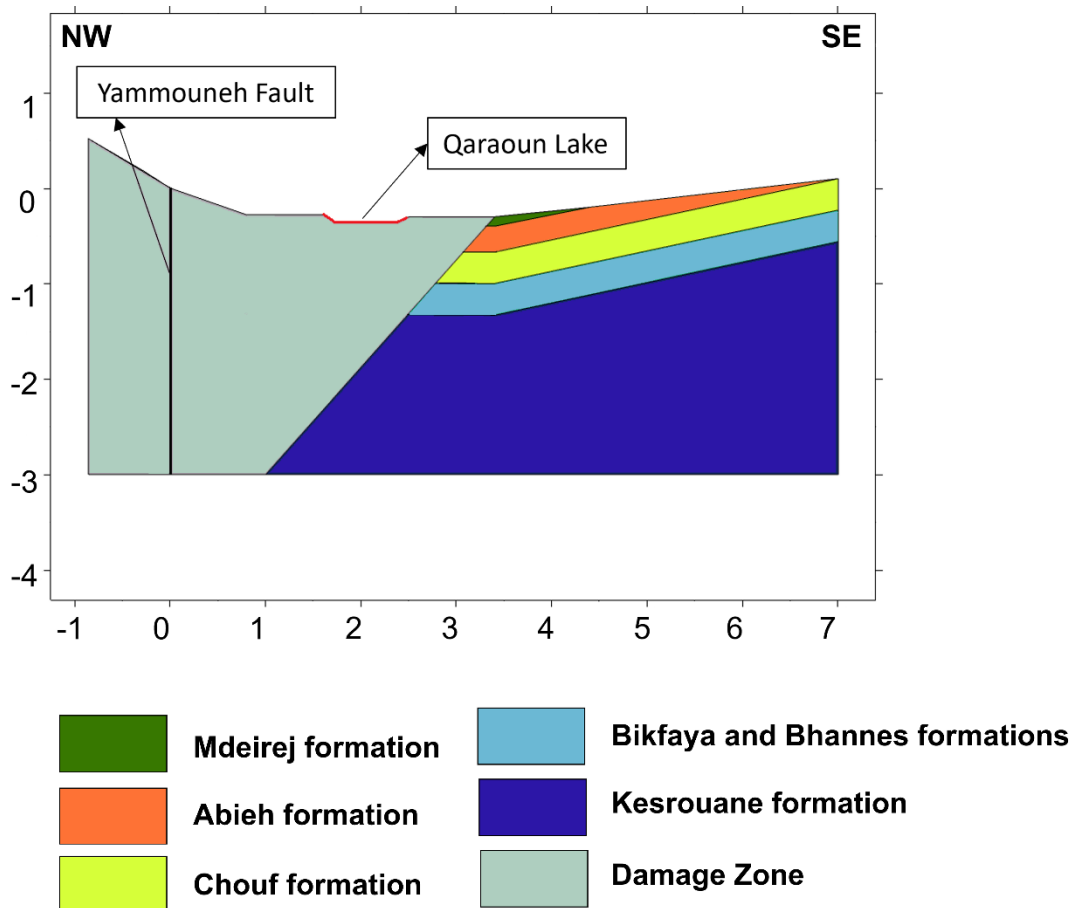
Figure 12. 2D cross-section (taken along the blue line in Figure 9a) showing the Qaraoun reservoir in red, the Yammouneh Fault, its damage zone, and the adjacent country rocks.

Figure 13 shows a 2D cross-section including the Batroun Fault, its damage zone, the Mseilha reservoir, and the successive lithologic layers mentioned in section 2.2.3. The time lag between maximum (26.5 m) and minimum (16 m) water levels is also taken as 6 months.
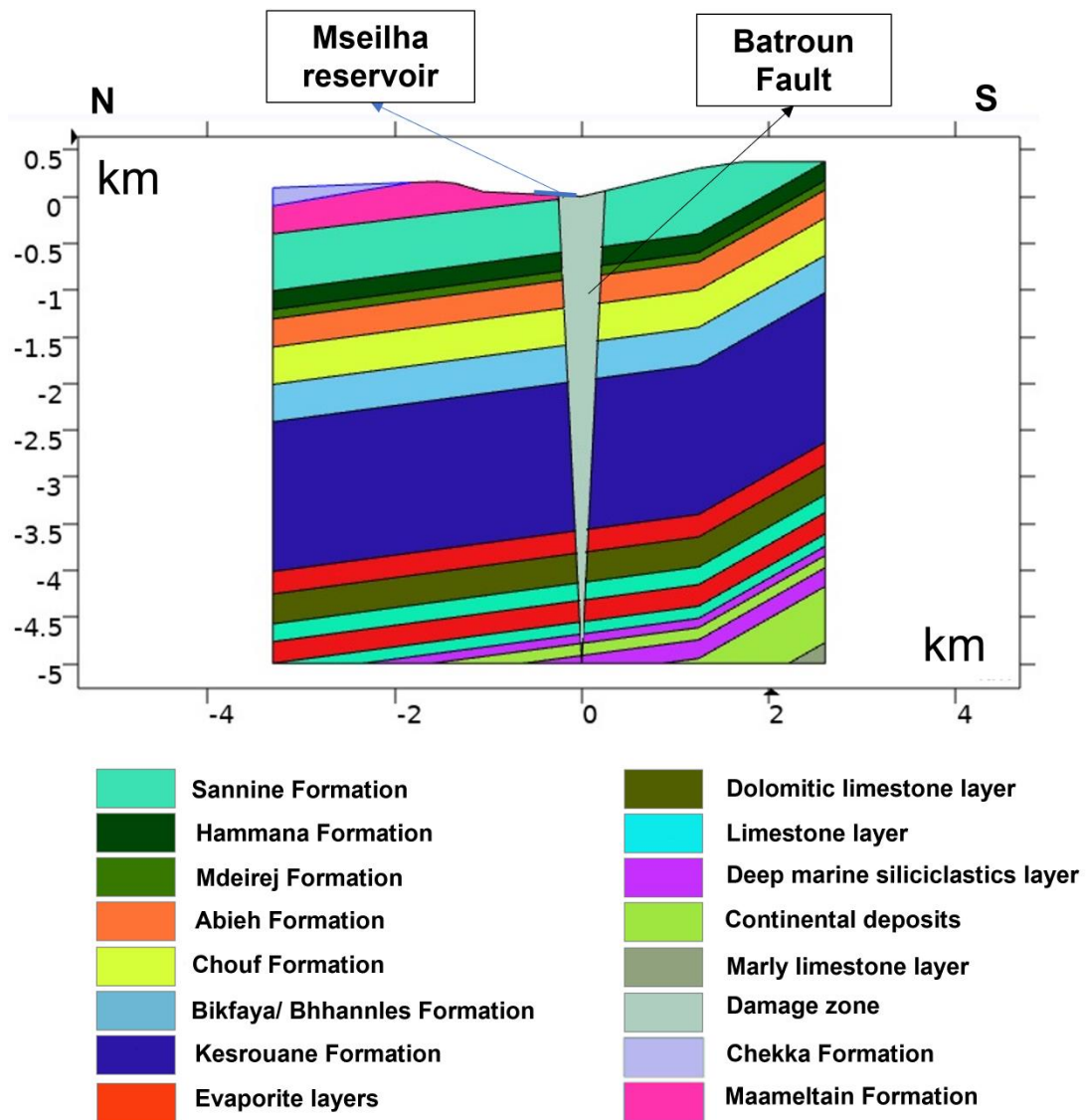
Figure 13. 2D cross-section taken along the red line in Figure 4, and showing the Batroun Fault, its damage zone, and the adjacent country rocks.

Table 1. Hydro-mechanical properties of the lithologic layers present at the dam sites (Jackson and Hudec, 2017; Marlow et al., 2011; Salah et al., 2020a, b, c, 2018).

Sedimentary Layers	Porosity (fraction)	Permeability (mD)	Bulk Density (kg/m^3)	Drained Poisson's Ratio	Young's Modulus (GPa)
Chekka Formation	0.04	0.0029	1871	0.222	14.8
Maameltain Formation	0.04	0.0016	2290	0.245	35
Sannine Formation	9.40E-04	0.01	2487	0.26	38
Hammana Formation / marly limestone	1.80E-03	0.04	2315	0.24	25.2
Mdeirej Formation / shallow marine limestone	0.15	1.75	2630	0.24	70
Abieh Formation	0.07	0.25	2544	0.235	60
Chouf Formation / continental deposits	0.15	1.75	2487	0.26	45
Bikfaya / Bhannes Formations	0.023	0.043	2660	0.31	61
Kesrouane Formation / dolomitic limestone	0.033	0.07	2715	0.2	30
Deep marine siliciclastic rocks	0.001	1.00E-02	2460	0.26	20
Evaporites	0.0075	1.00E-05	2165	0.265	44.4

4.2.2. 3D model

3D modeling in COMSOL Multiphysics has many limitations that did not allow us to recreate the topography, the formations and their dips as in reality. Since we faced multiple errors in the mesh, it was not possible to run a 3D model with a relatively complicated geometry having many thin layers. Therefore, the model was simply divided into 3 parts, two fault zones and a host rock (Figure 14), in order to minimize the number of elements needed and therefore reduce the errors and the required computational power. Nevertheless, in order to model the different layers, the same parameters that were used for the Bisri 2D model (section 4.2.1.1.) and presented in (Basbous et al., 2022) were averaged and entered as functions so that their values change with depth (Table 2). As such, the parameters are allocated as accurately as possible to the different parts of the model. As for the damage zones of the two faults, a porosity of 18% and a permeability of 2 mD were assigned for the rocks near the surface. These values decrease linearly with depth to the value of the surrounding host rocks. This assumption was taken based on the fact that fault cores are surrounded by highly fractured and deformed zones due to the fault's activity (Mitchell and Faulkner, 2009). As such, higher porosity and permeability with respect to the surrounding rocks can be assigned to damage zones, assuming that microcrack healing did not take place during inter-seismic cycles (Yang et al., 2021). In addition, a sensitivity analysis for these values is later conducted in section 5.2.2.

Concerning the mesh, several mesh sizes were tested for the 3D model with a smaller size each time until the results converged. The mesh size is small along the fault zones and becomes larger away from them. Similarly, different dimensions for the 3D model were tested, whereby the width and length of the model were increased until the boundary effects were eliminated.
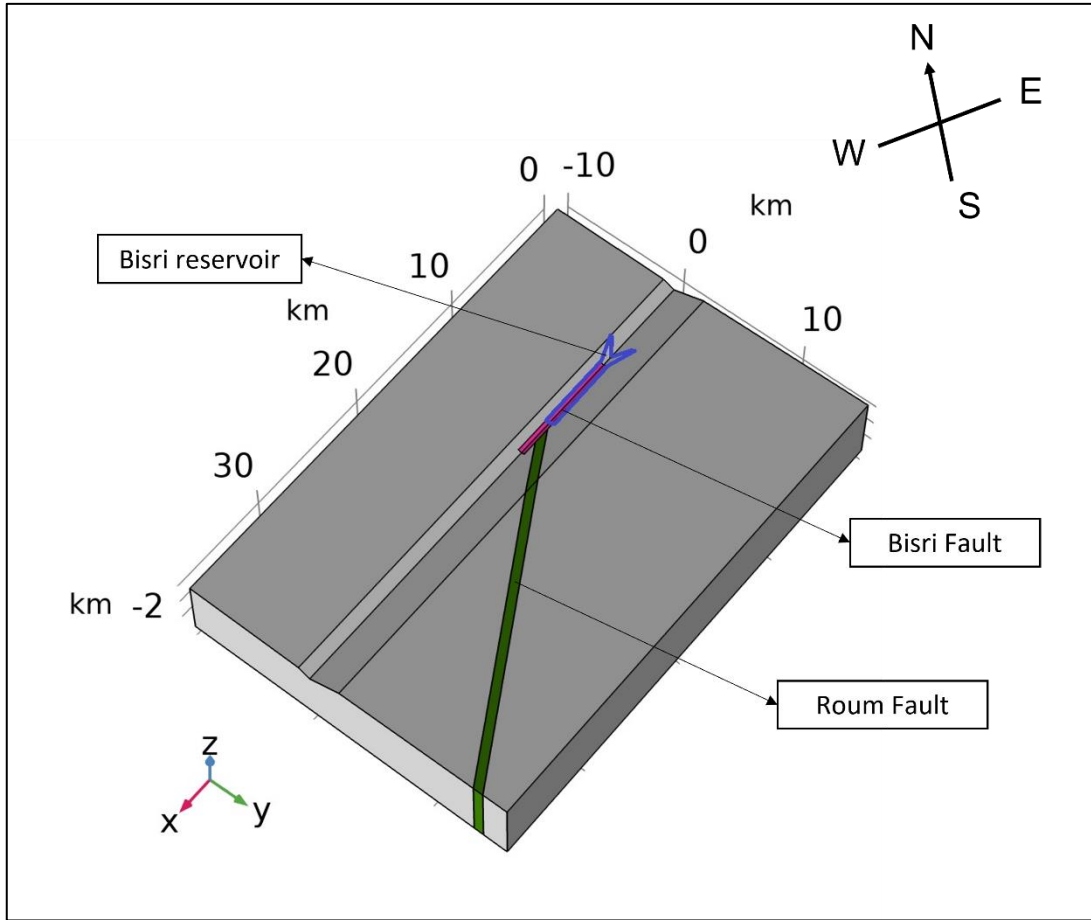
Figure 14. 3D diagram including the Roum Fault colored in green, the Bisri Fault colored in pink, and the Bisri reservoir delineated in dark blue.

Similar to the case of the 2D model, the pressure p applied at the reservoir is calculated as p = ρgh, using the oscillating water level h between 13 m and 60 m, the density of water ρ = 997 kg/m^3, and the acceleration due to gravity g = 9.8 m/s^2. A time lag of 6 months was assumed between maximum and minimum water levels to reflect the alternating rainy and dry seasons that both commonly last for 6 months in Lebanon. The water is expected to accumulate in the dam reservoir during winter and spring (6 months), and to be used during summer and fall (6 months) (Council for Development and Reconstruction, 2014).

Table 2. Allocation of the hydro-mechanical properties with respect to depth to represent the difference in lithologies (cf. Table 1).

From depth (km)	To depth (km)	Permeability (mD)	Porosity	Young's modulus (Gpa)	Poisson's ratio	Density (kg/m^3)	Biot coefficient
-4.5	-3.07	1.31134	0.11244	20	0.26	2460	0.79
-3.07	-2.77	1.00E-05	0.0075	44	0.26	2165	0.44
-2.77	-2.26	0.69588	0.07659	45	0.21	2683	0.79
-2.26	-2.02	1.00E-05	0.0075	44	0.26	2165	0.44
-2.02	0.02	0.07	0.033	30	0.20	2715	0.79
0.02	0.41	0.043	0.023	61	0.31	2660	0.79
0.41	1.14	1.19	0.12	54	0.25	2738	0.79
1.14	1.64	0.025	0.1	32	0.25	2401	0.79

4.3. Poroelastic model and governing equations

4.3.1. Coulomb stress changes

In general, the failure criterion for rupture initiation is expressed by the change in Coulomb Failure Stress expressed in equation (1). Faults in the subsurface are commonly critically stressed, thus any alteration in the pore pressure, normal stress, or shear stress can reactivate them, which is reflected by a positive ΔCFS indicating an increase in the risk for induced seismicity (Segall and Lu, 2015). In other words, any activity that causes

an overall positive change in the CFS could induce fault slip leading to an earthquake (Figure 5).

4.3.2. Coupled poroelastic model

The coupled poroelastic model describes the response of a saturated porous elastic medium to changes in stresses and pore pressure. This model states that any variation in the pore pressure can alter the poroelastic stresses of the medium, which is referred to as fluid-to-solid coupling, and vice versa, the solid-to-fluid coupling where any change in stresses affects the pore pressure (Biot, 1941; Rice and Cleary, 1976; Segall and Lu, 2015; Wang, 2000). The equilibrium equation under quasi-static condition and no additional body forces gives:

$$\nabla.\sigma = 0 \qquad (3)$$

The constitutive equation for a fluid-saturated poroelastic medium, with the approximation of elastic isotropy, can be written as:

$$G\nabla^2\mu + \frac{G}{1-2\nu}\,\nabla\epsilon - \alpha\nabla p = 0 \qquad (4)$$

where G is the shear modulus, μ is the velocity field, ν is Poisson's ratio, ϵ is the volumetric strain, α is Biot coefficient, and ∇p is the applied pressure gradient.

The pore fluid mass conservation equation can be written in terms of the fluid density ρ, the medium porosity $\emptyset$, and the fluid mass source Q_m as:

$$\frac{\partial}{\partial t}(\emptyset\rho) + \nabla.(\rho u) = Q_m \qquad (5)$$

Darcy's Law describes the fluid flow in a porous elastic medium by the equation:

$$u = -\frac{\kappa}{\mu}(\nabla p + \rho g \nabla z) \qquad (6)$$

where u is Darcy's velocity, κ is the permeability of the medium, μ is the fluid viscosity, and ∇z is the difference in elevation.

In addition, the poroelastic storage coefficient S is given by:

$$\frac{\partial}{\partial t}(\emptyset \rho) = \rho S \frac{\partial \rho}{\partial t} \qquad (7)$$

Then, the mass conservation equation can be re-written as:

$$\rho S \frac{\partial \rho}{\partial t} + \nabla \cdot (\rho u) = Q_m = -\rho \alpha \frac{\partial \epsilon}{\partial t} \qquad (8)$$

The increase of the rate of change of the volumetric strain $\frac{\partial \epsilon}{\partial t}$ causes the fluid to sink since there is more space for the fluid to diffuse, hence the negative sign in the mass source term. The equations are solved in 2D, with a plane strain assumption, using COMSOL Multiphysics finite element method. We couple the flow in porous medium module, which solves Darcy's law (equation (6) with the solid mechanics module, which solves the equilibrium equation under quasi-static conditions (equation (3). The poroelastic coupling is done through introducing the Biot coefficient in the constitutive law (equation (4) and the volumetric strain in the mass conservation equation (equation (8). This approach has practical limitations such as: (1) hydraulic and mechanical properties are averaged along domains, (2) the model is not dynamic which means that the hydraulic and mechanical properties remain unchanged throughout the simulation. In reality, the occurrence of seismic events would alter these properties along with the stress state of

the fault. Nonetheless, using a coupled poroelastic model is an effective approach to assess the potential for induced seismicity.

4.4. Initial and boundary conditions

The same initial and boundary conditions are assumed for all the models. Initially, the displacement vector is assumed null, and the pore pressure is at hydrostatic conditions. For the solid mechanics equations, a roller boundary condition is applied to the left and right sides of the domain prohibiting deformation normal to the boundary. A fixed constraint condition is assigned to the bottom boundary, while a free condition is set to the top boundary making it free to move in all directions (traction-free) (Fan et al., 2016; Segall and Lu, 2015). Figure 15 shows how the boundary conditions are allocated for the Bisri model. For the fluid flow equations, a no-flow boundary condition (the velocity component normal to the boundary is zero) is assigned to the bottom of the model. The width of the domain was chosen large enough so that there is no pressure build-up at the side boundaries that would affect the pressure at any of the studied faults. Then, a no-flow boundary condition is assigned to the left and right sides of the domain. As for the upper boundary, where the reservoir is located, a pressure boundary of oscillating values reflecting the minimum and maximum water levels with a 6-month lag is assigned. Outside of the reservoir location, a no-flow boundary condition is applied (e.g., Figure 15).
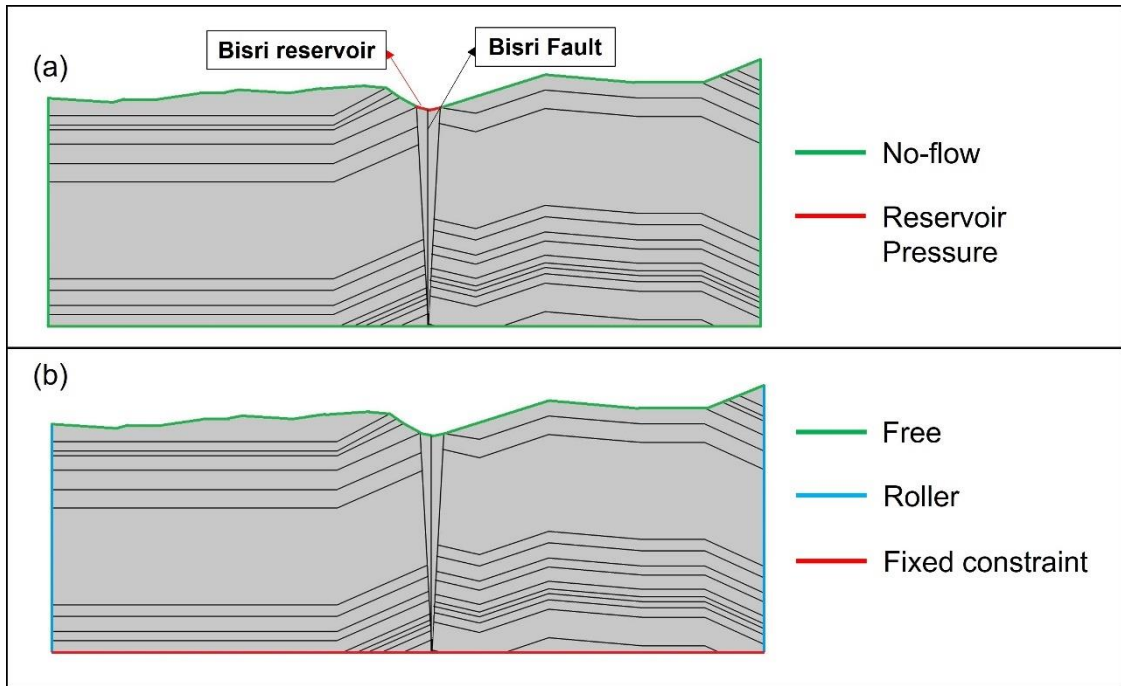
Figure 15. (a) Fluid flow boundary conditions; no-flow ($-n. \rho u = 0$) reservoir pressure (as per Figure 11). (b) Solid mechanics boundary conditions; roller ($n. u = 0$), fixed constraint ($u = 0$), where n is the vector normal to the boundary.

CHAPTER 5

RESULTS AND DISCUSSIONS

In this chapter, we discuss the effect of the location of the planned Bisri reservoir on the stability of the faults in the region for both the 2D and 3D models. In addition, a comparison is made with the effect of the location of the Qaraoun reservoir, which is located behind an existing dam, on the Yammouneh Fault. The comparison is made to answer the argument raised by the Bisri project planners that the Qaraoun reservoir has not witnessed induced seismic activity since its construction in 1959 despite its proximity to a major active fault. We will highlight the difference between the two cases and why the Qaraoun dam does not create a major risk for induced seismicity. Lastly, we discuss the effect of the Mseilha dam on the Batroun Fault assuming the dam is fully functional.

5.1. The Bisri dam 2D model

Fractures in fault damage zones represent the dominant flow pathways in rocks, allowing the pressure to diffuse to deeper layers (Yehya et al., 2018), and they cause the rock mass to become less stable (Witherspoon and Gale, 1977). Figure 16 shows the diffusion of the pore pressure, caused by the oscillating pressure from the supposed Bisri reservoir, and due to the presence of the damage zone, which causes an increase in pressure along the Bisri Fault. The pressure remains high in the shallower layers, even after pressure diffuses to deeper layers, due to the continuous pressure load of the oscillating water level of the reservoir.
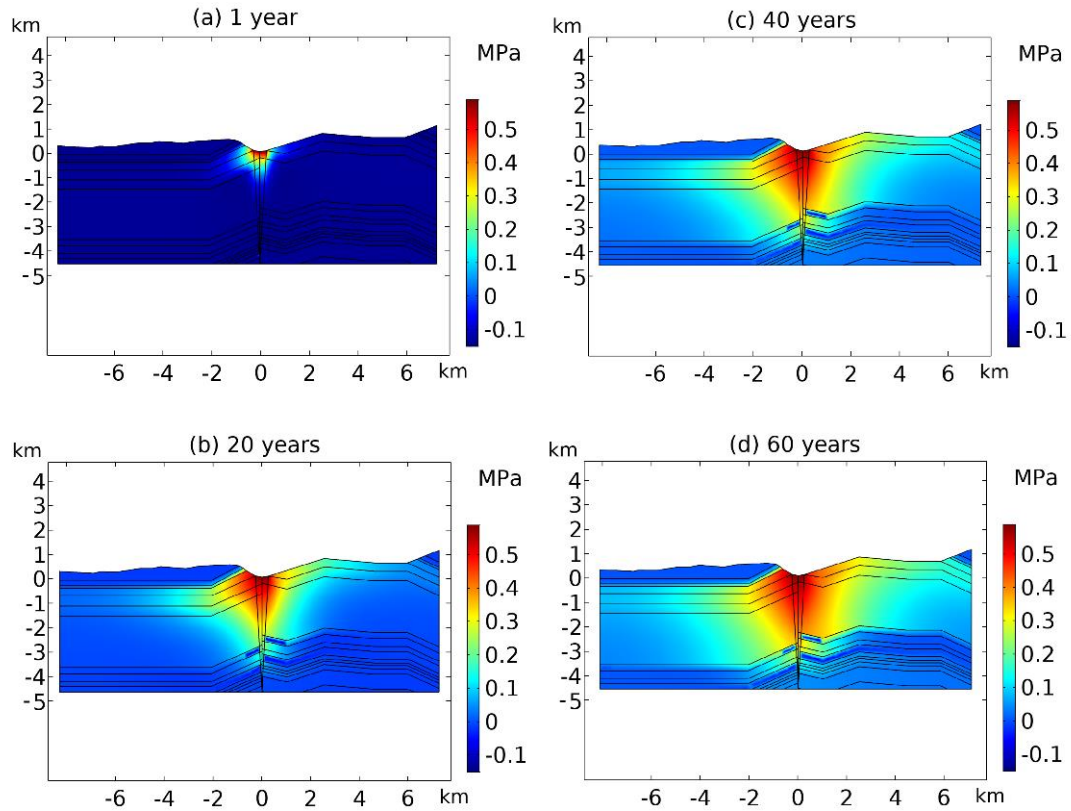
Figure 16. The change in pore pressure (relative to the initial hydrostatic condition) along the 2D section shown in Figure 10, after 1 year (a), 20 years (b), 40 years (c), and 60 years (d) from impoundment.

In Figure 17a, we notice the instantaneous increase in pore pressure at the shallow layers due to the initial impoundment. As the maximum water level is reached after 0.75 years, the pore pressure increases greatly at shallow levels. After 1.25 years, the water level decreases to its minimum, but the pore pressure keeps increasing. At the shallow levels, this increase is due to the undrained effect where the additional pore pressure caused by the reservoir still needs more time to diffuse. Whereby at the deep levels, this increase is due to the delayed effect of pore pressure diffusion from the previous water level. In addition, at a depth of -4.2 km (deep layers), there is a noticeable increase in the pore pressure, because of the initial undrained effect since at this level the porosity and permeability of the rocks become very low. Diffusion is relatively a slow process, hence

Figure 17. (a) Variation of the pore pressure with depth at the start of the impoundment (blue curve), 0.75 years after impoundment when the maximum water level is reached (green curve), 1.25 years after impoundment when the water level has reached the minimum (red curve), and 1.75 years after impoundment where the water level is maximum (pink curve). (b) Variation of the pore pressure with depth after 10 years (blue curve), 20 years (green curve), and 30 years (red curve) from impoundment where the water level is average. (c) Variation of the pore pressure with depth after 40 years (blue curve), 50 years (green curve), and 60 years (red curve) from impoundment where the water level is average.

a pressure perturbation on the surface needs a specific time to create a response at different levels. The time scales are governed by the hydraulic and poroelastic properties of the geologic formations. After 1.75 years of impoundment, at -4.2 km, we notice a decrease in pore pressure with time whereby it reaches values below hydrostatic (negative). This decrease is due to the drained effect where the diffusion of pore pressure

outward is greater than the additional pore pressure coming from the reservoir to this depth. Figure 17b shows the duration between 10 and 30 years after initial impoundment, and indicates that after 10 years, the pressure at the surface does not vary because the additional pore pressure has dissipated. Comparing the three curves we notice that the increase in pore pressure with time is greater in the deeper layers than that in the shallow layers. This is due to the delayed response where the pressure diffuses and builds up at the deeper levels over time near the low permeability basement. Figure 17c shows the duration between 40 and 60 years after initial impoundment. The pressure increases, however, at a slower rate in the shallow layers and at the same rate in the deeper layers due to pore pressure diffusion. We observe a smaller variation of pressure between of -3.5 and -4 km for all curves because the evaporite layer has very low porosity and permeability. In summary, the pore pressure tends to have a destabilizing effect on preexisting faults since it decreases the effective normal stress facilitating failure (Figure 5). This implies that the reservoir has an increasingly and continuously destabilizing effect on the Bisri Fault.

Figure 18a shows that the normal stresses are positive indicating tensile stresses that have a destabilizing effect on faults, since it places faults under an extensional load. The stresses increase but at a slower rate with time (Figure 18b). After 30 years, the stresses start to stabilize with little increase (Figure 18c). The horizontal fluctuations in the curves are representatives of the different layers with different mechanical and hydraulic properties.
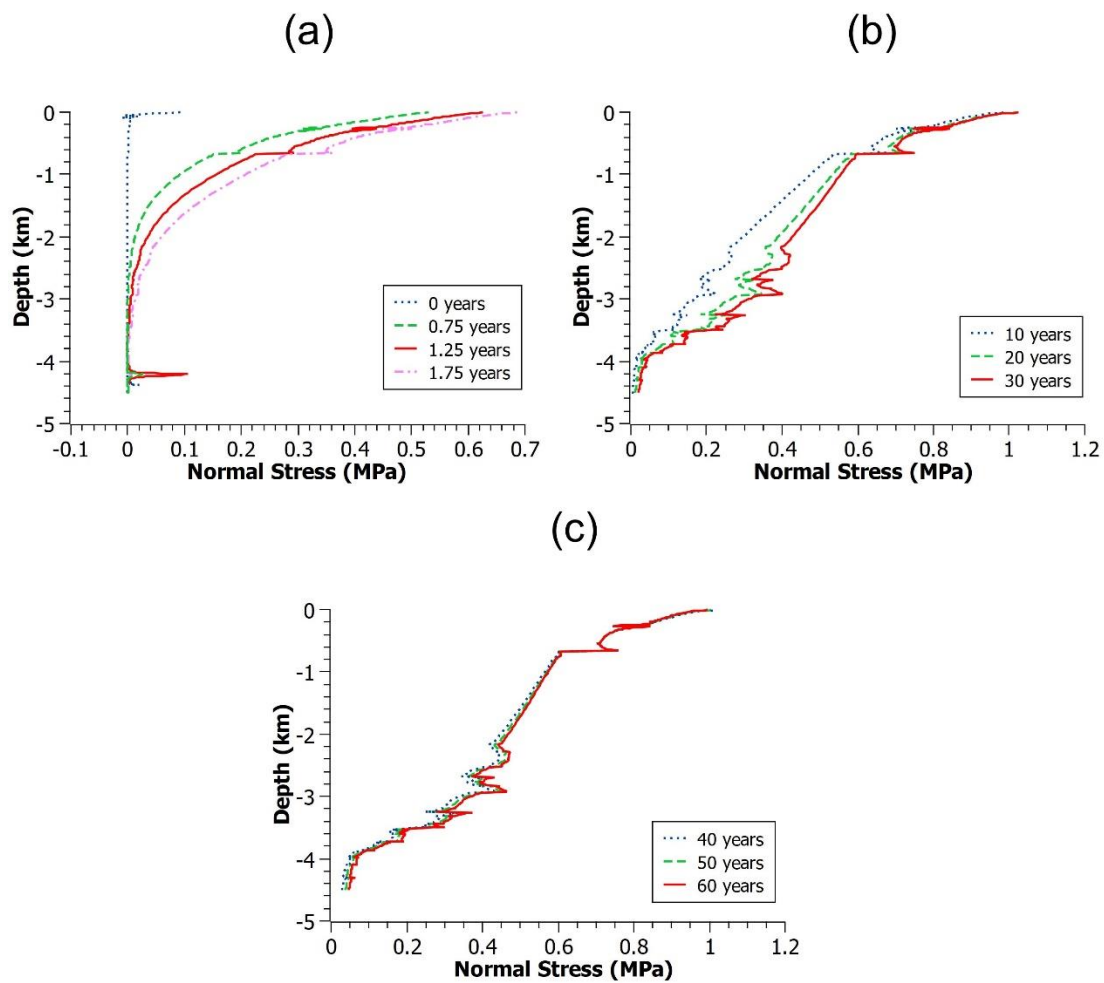
Figure 18. (a) Variation of the normal stress with depth after the start of the reservoir impoundment (blue curve), 0.75 years after impoundment (green curve), 1.25 years after impoundment (red curve) and 1.75 years (pink curve) after impoundment. (b) Variation of the normal stress with depth after 10 years (blue curve), 20 years (green curve), and 30 years (red curve) from impoundment. (c) Variation of the normal stress with depth after 40 years (blue curve), 50 years (green curve), and 60 years (red curve) from impoundment.

Both the pore pressure and the positive normal stresses have a destabilizing effect on the fault, which is evident in the positive values of the CFS that exceed 0.1 MPa. It is noted from the study on the anthropogenic effect on induced seismicity by Mulargia and Bizzarri (2014) that an increase of 0.1 MPa in the overall stresses can lead to failure in critically stressed faults. This value of 0.1 MPa is considered a conservative threshold

above which all faults at the vicinity of anthropogenic activity must be assumed to fail (Mulargia and Bizzarri, 2014). The CFS values increase with time because of the combined effect of the pore pressure and tensile normal stresses (Figure 19). As such, the CFS curves follow the trend of the normal stress curves but with a higher value due to the additional effect of the pore pressure. For example, after 40 years (Figure 19c) the CFS values stabilize at the shallow layers owing to the limited increase in the normal stresses but increase with depth because of the pore pressure diffusion. This relation is better seen in Figure 20 that shows the variation of the CFS, pore pressure, and normal stress with time in parallel at 3 different depths. The CFS values keep increasing for decades indicating protracted seismicity.

To further investigate the effect of the overall Coulomb stresses, we evaluate the change in the seismicity rate. Besides calculating the change in the overall Coulomb Failure Stress along faults, predicting the rate of seismicity is another way to assess the potential for induced seismicity (Chang and Yoon, 2018; Segall and Lu, 2015; Wenzel, 2015). Dieterich (1994) developed a seismicity rate model relating the rate of earthquake nucleation to changes in coulomb stress and governed by rate and state friction. In the absence of any stress perturbation, the rate of seismicity will remain constant with time, otherwise under stress perturbation, an increase in this rate is expected. The rate of seismicity R can be calculated relative to a background stressing rate by:

$$\frac{dR}{dt} = \frac{R}{t_a} \left(\frac{\dot{\tau}}{\dot{\tau}_0} - R \right) \qquad (9)$$

$\dot{\tau}_0$ being the background stressing rate, $\dot{\tau}$ the Coulomb stressing rate, and $t_a \equiv a\frac{\bar{\sigma}}{\dot{\tau}}$ the characteristic relaxation time, where a is the constitutive parameter in the rate state friction law quantifying the direct effect on slip.

66
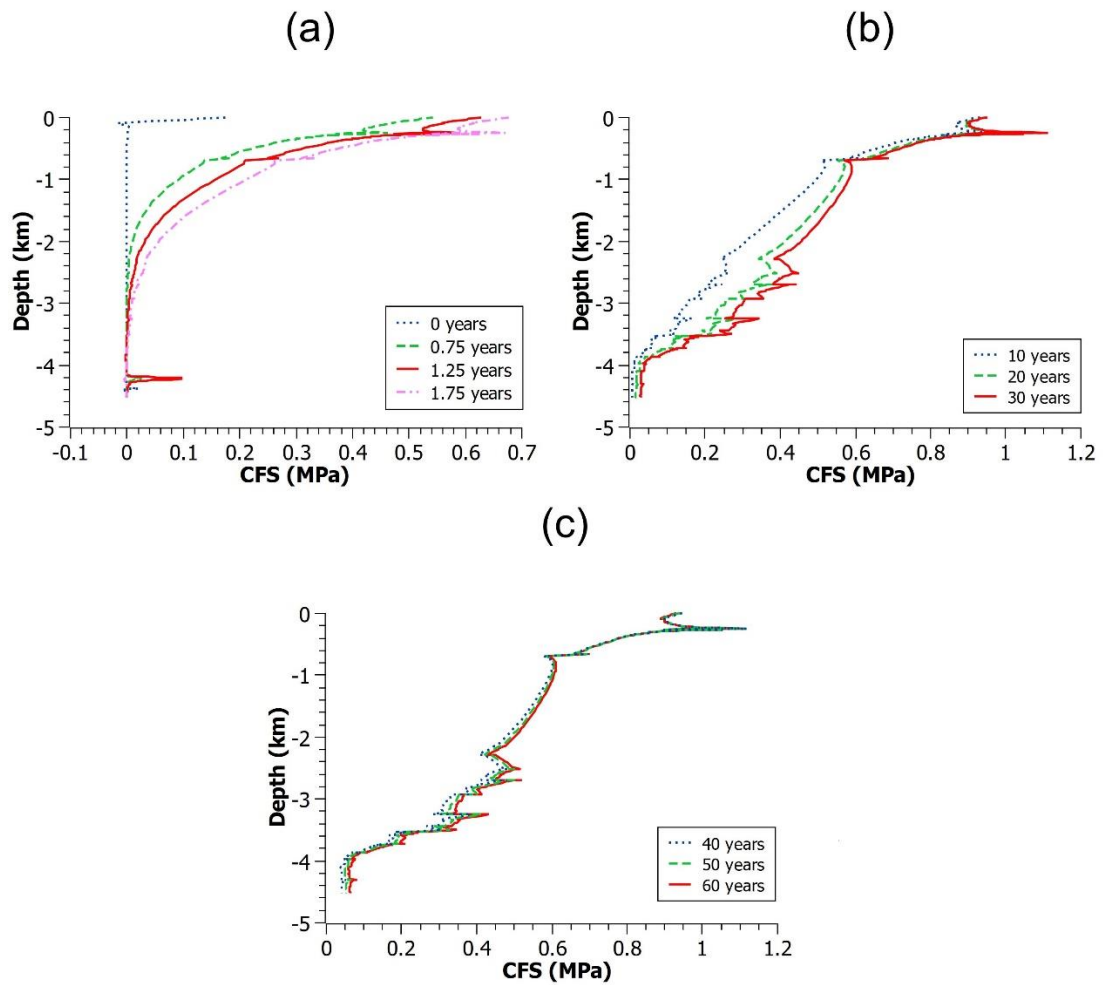
Figure 19. (a) Variation of the CFS with depth after the start of the reservoir impoundment (blue curve), 0.75 years after impoundment (green curve), 1.25 years after impoundment (red curve) and 1.75 years (pink curve) after impoundment. (b) Variation of the CFS with depth after 10 years (blue curve), 20 years (green curve), and 30 years (red curve) from impoundment. (c) Variation of the CFS with depth after 40 years (blue curve), 50 years (green curve), and 60 years (red curve) from impoundment.

In this study, $\bar{\sigma}$ is taken as 18.8 MPa (Markou and Papanastasiou, 2018), $\dot{\tau}$ as 0.001 MPa/year corresponding to a cumulative stress drop of 1 MPa every 1000 years, and a as 0.003 (Chang and Yoon, 2018; Segall and Lu, 2015). The resulting characteristic relaxation time t_a becomes 56.4 years which is comparable to the simulation duration for this study. However, we will discuss other values of the relaxation time to highlight the sensitivity of R to this parameter, and how that affects the risk assessment.
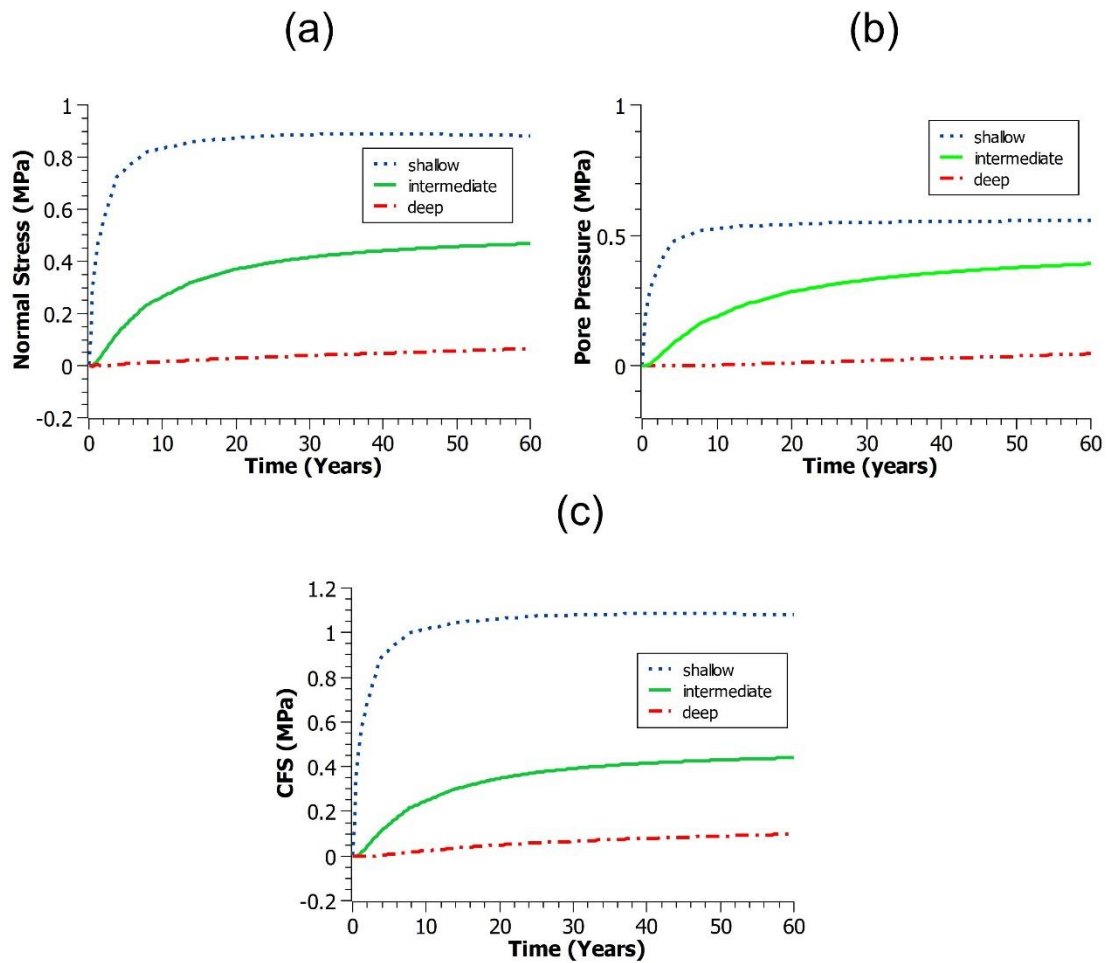
Figure 20. Variation with time of the normal stress (a), the pore pressure (b), and the CFS (c), at shallow (-0.3 km), deep (-4.1 km), and intermediate (-2.2 km) depths. The negative sign indicates depth below the surface.

The initial value of R is 1 and from equation (9), R returns to this value when time t is much greater than t_a ($t \gg t_a$). The higher the value of R, the higher the stressing rate relative to the background stressing rate, which increases the probability to induce earthquakes. Figure 21 shows the results for equation (9) for three points along the Bisri Fault, taken at three distinct depths: shallow, intermediate, and deep. At a shallow depth we find that the rate of induced seismicity rises rapidly to very high values, which is expected due to the initial effect of reservoir impoundment as well as the early undrained

response, but then decreases gradually to steady state after around 20 years as the pore pressure diffuses to deeper levels. As we go deeper along the fault,

(a) (b)

(c)
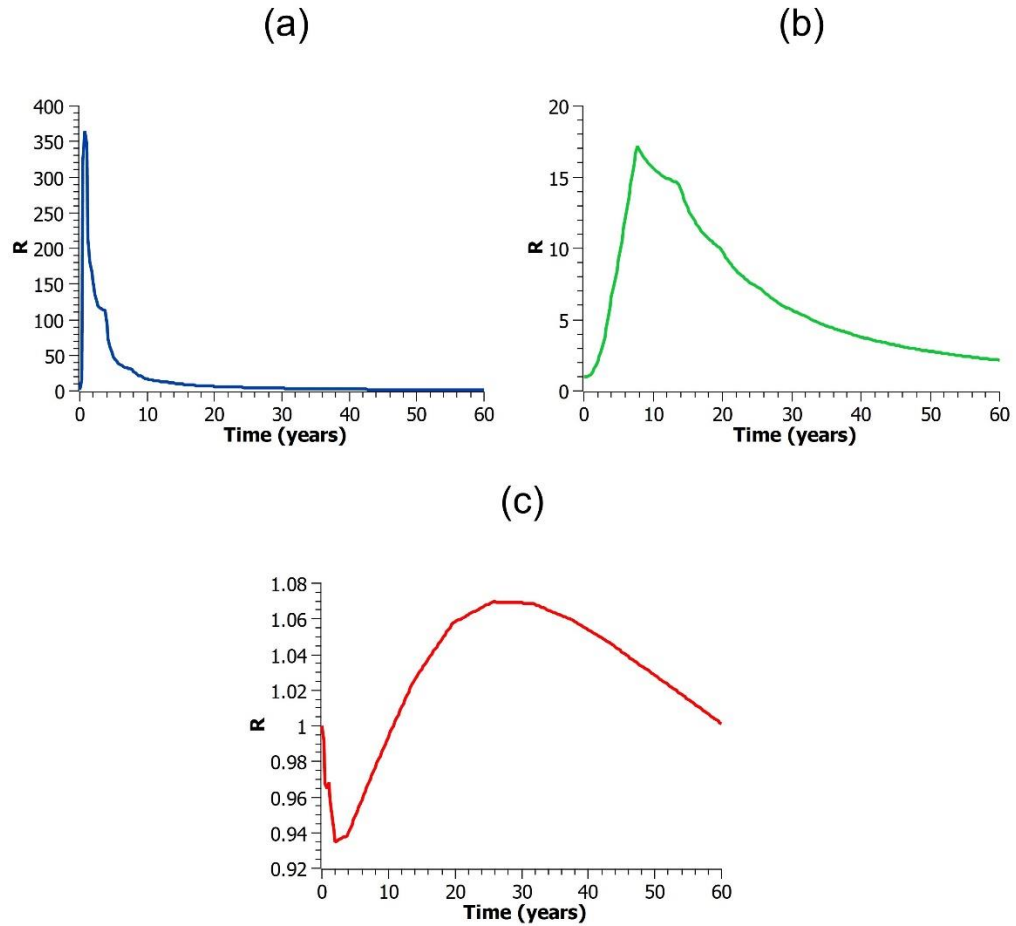
Figure 21. Variation of the induced rate of seismicity with time at three different depths along the Bisri Fault: (a) at -0.3 km, (b) at -2.2 km and (c) at -4.1 km.

the values of R decrease but take a longer time to restore back to steady state which is due to the delayed effect of pore pressure diffusion. We note that in very deep regions the rate of seismicity is close to the initial rate, which is set to 1, and this indicates that the potential of seismicity becomes higher in the shallower regions. Also, at times much greater than t_a, the rate of seismicity will decay to reach 1. Equation (9), thus, reaches a steady state solution and shows Omori-like decay when rapid change in stress occurs

(Segall and Lu, 2015). However, its limitation is its inability to predict the earthquake magnitude, but it can give a good indication on the potential for induced seismicity for the Bisri Fault. Hence, the risk for induced seismicity for the shallow regions of the Bisri Fault is mainly in the first 10 years, however, the risk in the deeper regions near the stiff basement, which can lead to higher magnitude earthquakes, is after 10 years of its initial impoundment and continues to several decades later. When R is calculated for the Qaraoun case, no increase in the rate of seismicity is obtained because there is no stress perturbation rate above the background stress rate.

For a comparative analysis for the Bisri Fault response, we take different assumptions for the relaxation time (Figure 22), and we find that a lower t_a (30 years) leads to a higher seismicity rate, but the seismicity restores back to steady state faster. On the other hand, if we consider a higher t_a (175 years), the seismicity rate takes much longer to restore back to steady state, but the values of R are lower. In all cases, building the Bisri dam disrupts the steady state of the existing Bisri Fault, and it would need many decades to be restored.

The dip angle of the Bisri Fault was taken as 90° in this study, but changes in fault orientation can influence the calculated CFS values. A geophysical electrical resistivity survey conducted in the Bisri Valley provided that the shallow part of the Bisri fault is probably vertical with little information about its deep part (Bureau Technique pour le Developpement, 1983). However, from the geological point of view, and from studying the displacement and structures associated with this fault we can infer that this fault is vertical (Nemer, 2019). Despite that, we can evaluate the effect of orientation. Larger orientation in the dip (lower dip angle) will slow the pressure diffusion process to deeper

regions and affect the CFS values, and hence the rate of seismicity. So, it is more likely to decrease the rate of seismicity.
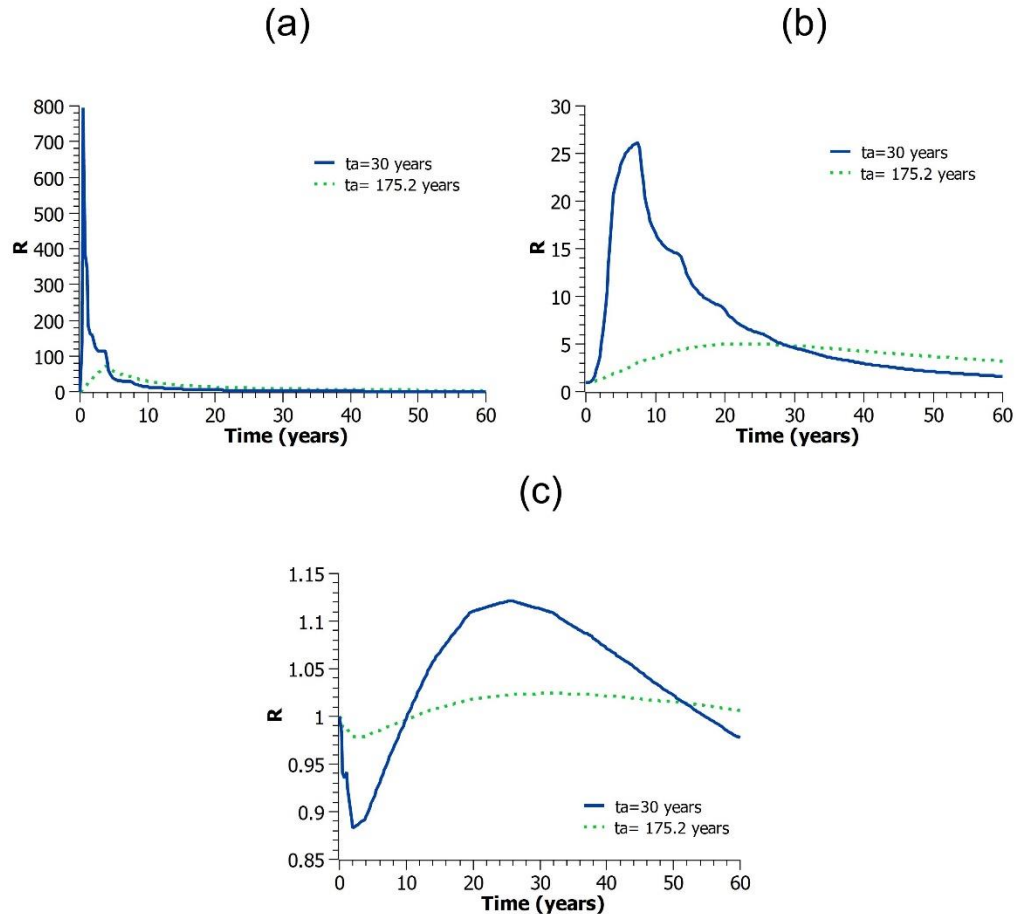
Figure 22. Variation of the seismicity rate with time considering two characteristic times (ta = 30 and ta = 175.2 years) at three different depths along the Bisri Fault: (a) -0.3 km (shallow), (b) -2.2 km (intermediate) and (c) -4.1 km (deep).

This section was published in Basbous et.al (2022) (Appendix II).

5.2. The Bisri dam 3D model

In section 5.1 we discussed the possibility of induced seismicity caused by the Bisri dam based on a 2D model. The model gives good insight and prediction of the

seismic risk of building the dam. However, it does not take into consideration the 3-dimensional distribution of stresses and propagation of the pore pressure, nor the effect of the Bisri reservoir on the nearby Roum Fault.

5.2.1. The Bisri Fault

In order to compare the results of the new 3D model with those of the 2D model (taken along the same section across the Bisri Fault), an altered 2D model was created in the interest of overcoming the limitations discussed in section 4.3. In this new 2D model, all the layers were simplified into one layer, and the parameters were input as functions similar to those of the 3D model. The results of this new model were compared to those of the initial 2D model (section 5.1; Figure 23); although those results were not exactly the same, they provided a good idea about any over- or underestimation in the parameters of the 3D model. It is important to note that the 3D model is a better approach than the 2D model as the former takes into consideration the distribution of stresses as well as the diffusion of pore pressure in 3 dimensions, even when simplifications were made.
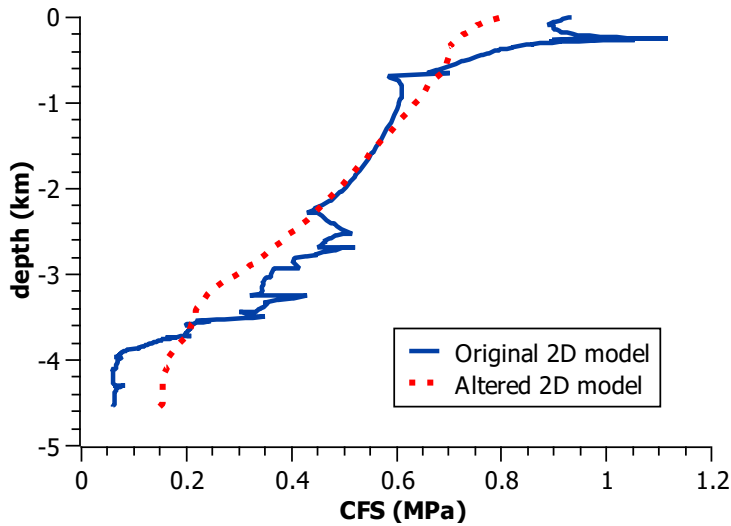
Figure 23. Comparison of the CFS results of the original 2D model (blue curve) and the new altered 2D model (red curve) where the parameters were averaged.

Comparing the CFS values of the new 2D model with the original 2D model, we find that the trend of the results is similar. However, the values are overestimated in the deep layers (below 3.5 km) and underestimated in the shallow layers (above 0.5 km). Therefore, when analyzing the results of the 3D model, this must be taken into consideration in the sense that the CFS curves at depth must be closer to each other and have slightly lower values, while in the shallow layers they must have higher values.

Both the 3D and the 2D models display positive pore pressure values that increase with time along the Bisri Fault with the highest values in the shallow layers directly underneath the reservoir (Figure 24). In Figure 24a and Figure 24b, the three curves corresponding to 10, 30 and 60 years become further apart with depth, so the rate of increase of the pore pressure with time in the deep layers is higher than in the shallow ones due to the delayed effect of pore pressure diffusion. To be noted also that the values in the 2D model are higher (about double) than those in the 3D model (Figure 24). This is expected since in the 3D model the pore pressure diffuses along the depth, width and

length of the model versus only along the width and depth in the 2D model. Additionally, the two interconnected damage zones of the Bisri and Roum Faults where high porosity and permeability are assumed to prevail present a medium where pore pressure can diffuse quickly away from the Bisri Fault.

The CFS values are affected mainly by the pore pressure and normal stress values, since the shear stresses are relatively negligible. Therefore, the differences in CFS values between the 3D and 2D models represent the differences observed for normal stress (Figure 25) and pore pressure (Figure 26). Nevertheless, the mechanism of failure is the same. The CFS values are positive and increasing with time due to the increasing tensile normal stresses and diffusing pore pressure. Even if the CFS values are lower in the 3D model, they are still considered a threat since they surpass the threshold of 0.1 MPa (Mulargia and Bizzarri, 2014). Thus, the results of the 3D and 2D models are matching since both models show the same outcome being that impounding the Bisri reservoir lead to the activation of the Bisri Fault.
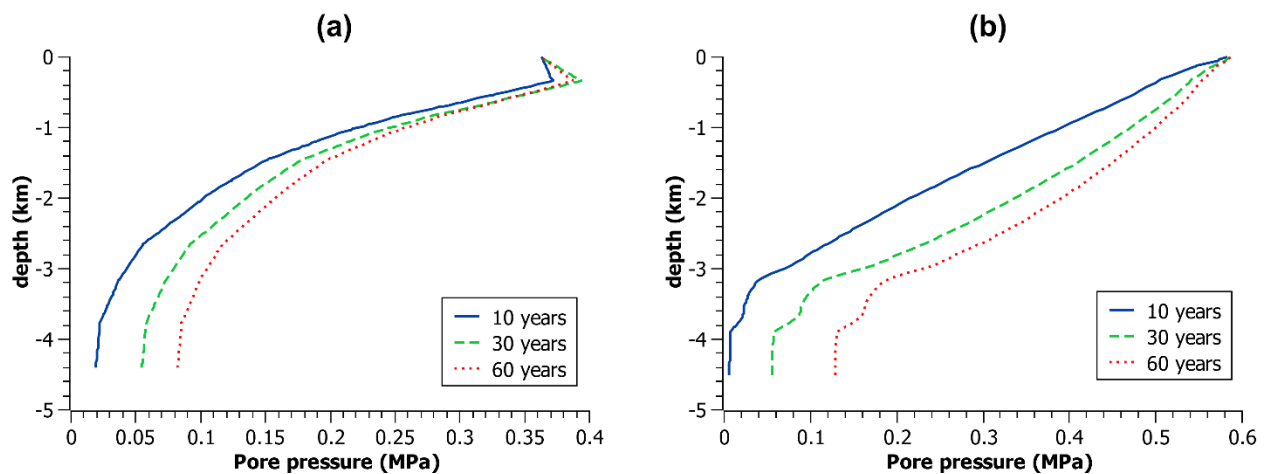
Figure 24. Variation of the pore pressure values with time along the Bisri Fault from the 3D model (a) and the 2D model (b).
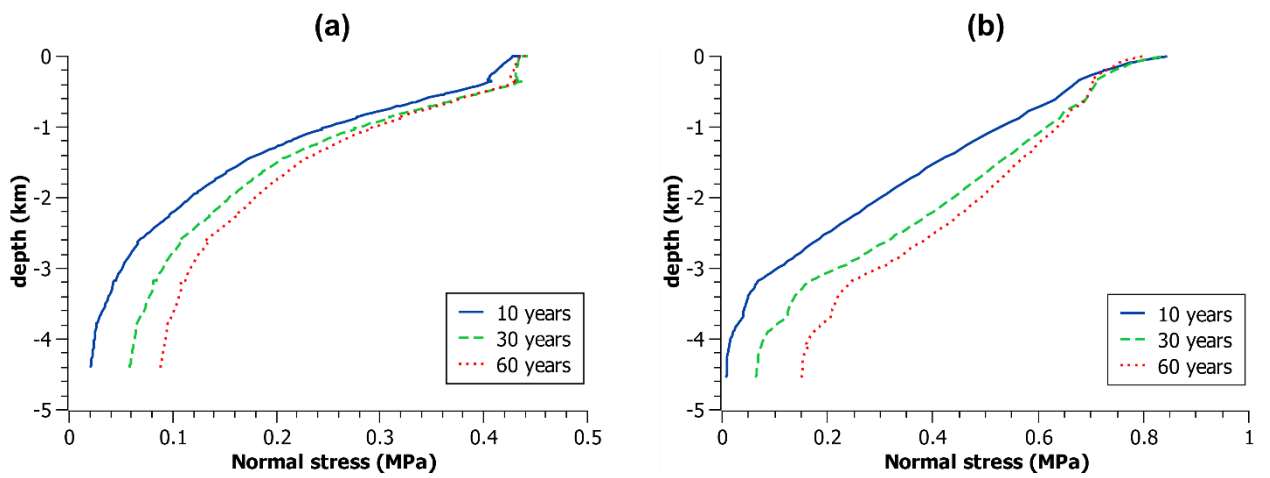
Figure 25. Variation of the normal stress with time along the Bisri Fault in the 3D model (a), and the 2D model (b).
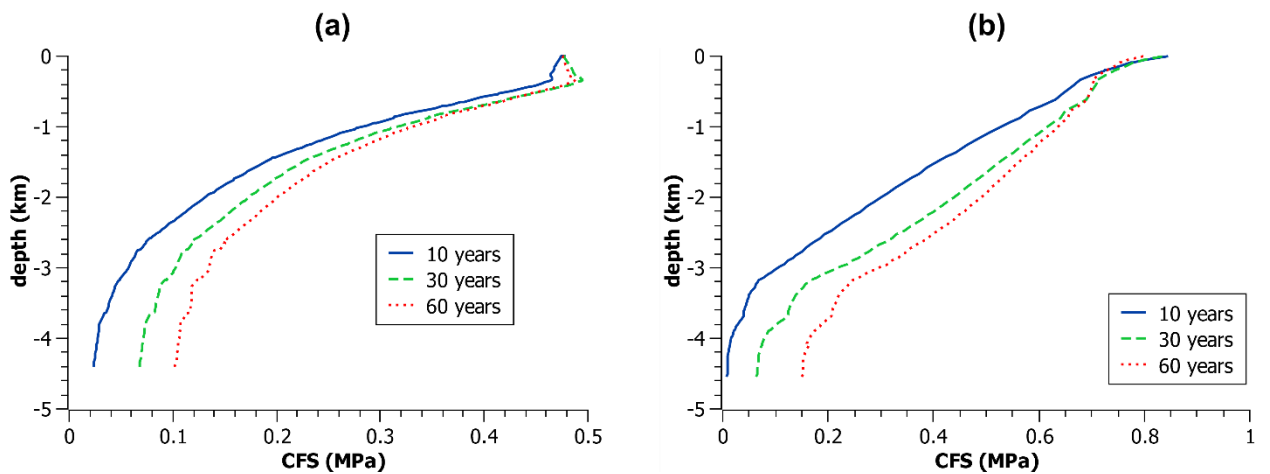
Figure 26. Variation of the CFS with time along the Bisri Fault in the 3D model (a), and the 2D model (b).

5.2.2. The Roum Fault

As suggested by Roeloffs (1988), reservoirs located directly above strike-slip faults tend to have a destabilizing effect on the faults. However, even though the Roum

Fault does not lie directly underneath the Bisri reservoir, its interconnection with the Bisri Fault increases its risk of being destabilized.

The normal stress, CFS, and pore pressure are computed along the Roum Fault to better understand the effect of the Bisri dam and reservoir on it. Figure 27 shows the normal stress, pore pressure, and CFS values computed along the Roum Fault at the intersection with the Bisri Fault. The normal stresses are tensile (positive) and increasing with time. The pore pressure values are also positive and increasing with time owing to pore pressure diffusion and build up. It is important to note that theoretically values of 0.01 MPa and experimentally values of 0.05 MPa of fluid pressure were found capable of triggering earthquakes (Mulargia and Bizzarri, 2014). These values are easily surpassed along the part of the Roum Fault nearest to the reservoir, where pore pressure
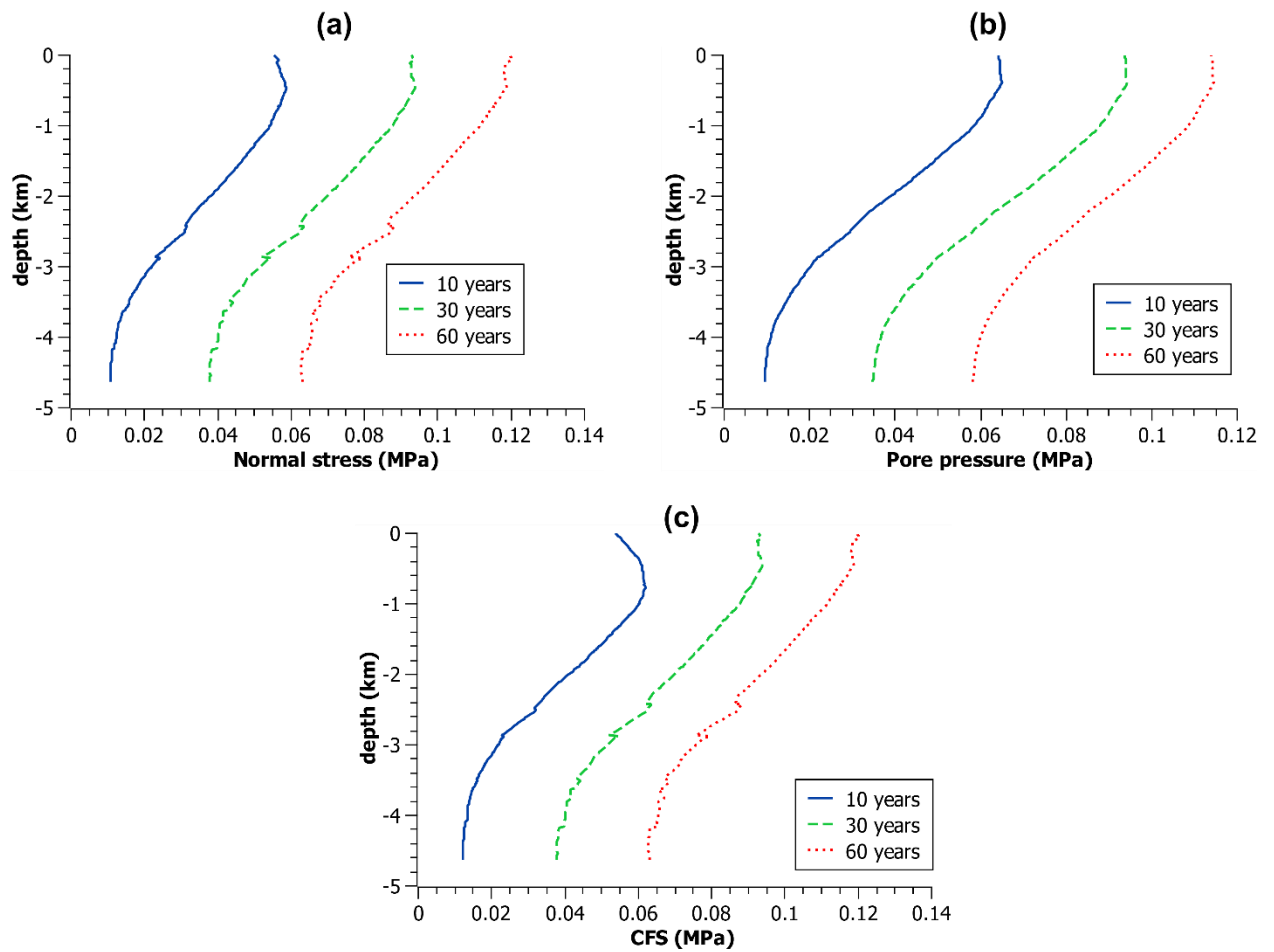
Figure 27. Variation of (a) normal stress, (b) pore pressure, and (c) CFS along the Roum Fault at approximately 2 km away from the Bisri reservoir.

shows values as high as 0.1 MPa several decades after impoundment. As for the CFS values, they are positive and increasing with time as expected from the normal stress and pore pressure values. They also reach the conservative threshold of 0.1 MPa indicated by Mulargia and Bizzarri (2014) at which all faults in the vicinity of anthropogenic activity must be assumed to fail.

Figure 28 shows how the CFS values are distributed along the Roum Fault and the Bisri Fault in 3D. For the Bisri Fault, the largest CFS values occur beneath the reservoir reaching around 5.5 MPa and decrease away from it. As for the Roum Fault, the
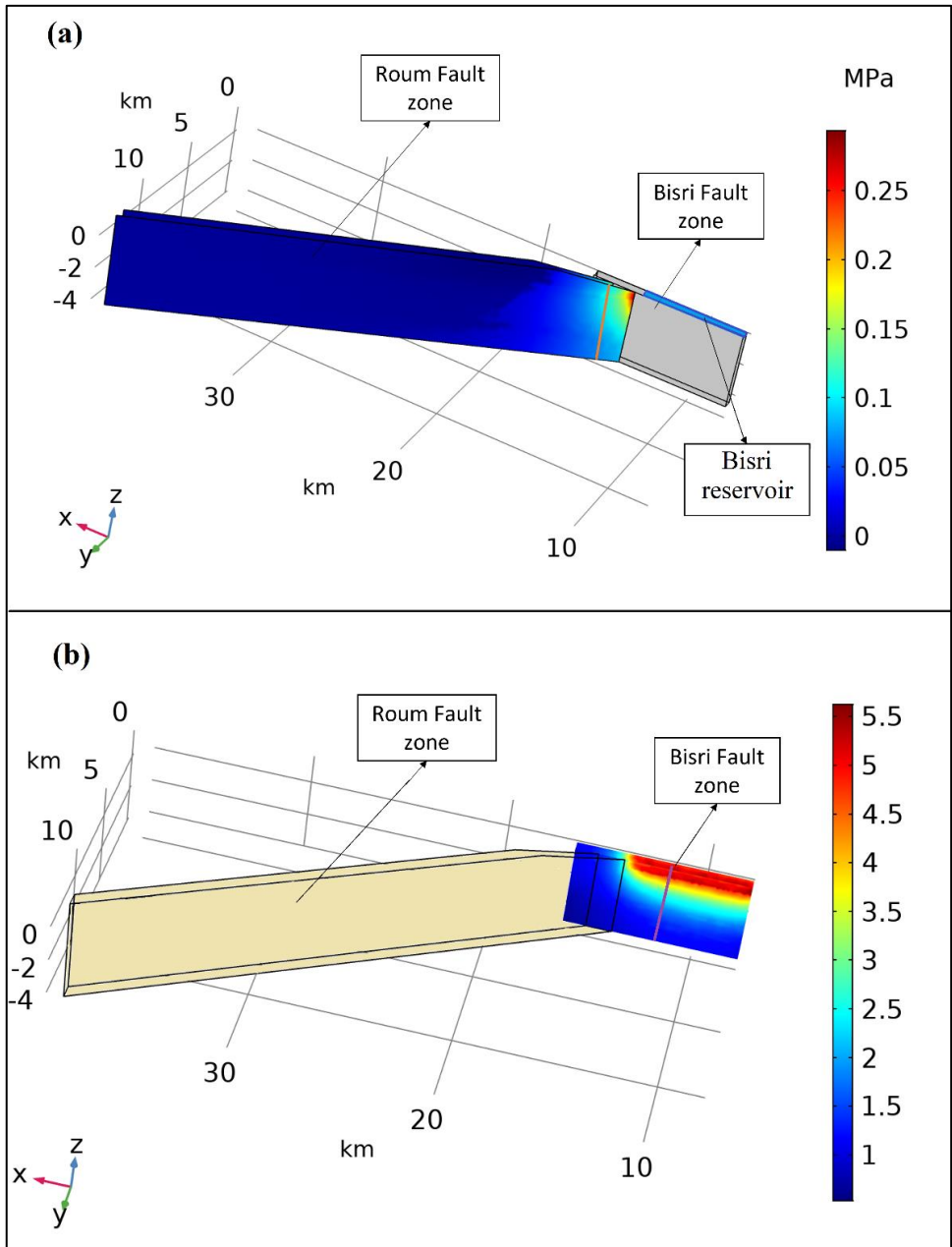
Figure 28. (a) 3-dimensional distribution of CFS values along the Roum Fault 60 years after impoundment, where the two displayed planes represent the boundaries of the Roum Fault damage zone. The Bisri Fault is shown in grey, the part of the Bisri reservoir covering the Bisri Fault is shown in blue, and the orange line along the Roum Fault represents the location where the CFS, normal stress and pore pressure values were computed in Figure 27 and Figure 29. (b) 3-dimensional distribution of CFS values along the Bisri Fault 60 years after impoundment. The Roum Fault is shown in yellow, and the purple line along the Bisri Fault represents the location where the CFS, normal stress and pore pressure values were computed in Figure 24a, Figure 25a, and Figure 26a. Note that the values are plotted separately on the fault surfaces due to the discrepancy in the CFS value ranges.

largest CFS values occur at the corner of the fault where it intersects with the Bisri Fault and reach around 0.28 MPa. Stress changes anywhere on the fault plane, in this case at one shallow end of the Roum Fault, can affect asperities (stuck patches) that would break and propagate throughout the fault plane causing an earthquake. So, regardless of where the perturbation occurs, any generated weakness can eventually stimulate an earthquake. This is known as coseismic slip. In addition, stress changes can be transmitted as they propagate beyond the fluid-pressurized region in a phenomenon known as aseismic slip (Bhattacharya and Viesca, 2019). Thus, estimating the maximum induced earthquake magnitude, with the assumption that the affected volume of the fault zone is only where pore pressure can diffuse to (or the areas with elevated CFS values), can lead to an underestimation.

A sensitivity analysis of the hydraulic parameters of the fault damage zones was conducted in order to see the effect they would entail on the stresses and pore pressure diffusion along the Roum Fault. Assuming the values of porosity and permeability were larger, pore pressure will diffuse faster along the Roum Fault, thus building up more during a shorter period of time. This entails higher normal stress and CFS, which is clear in Figure 29 that shows the comparison of CFS, pore pressure, and normal stress 5 years and 60 years after impoundment when porosity and permeability are increased by 10% and 30%.
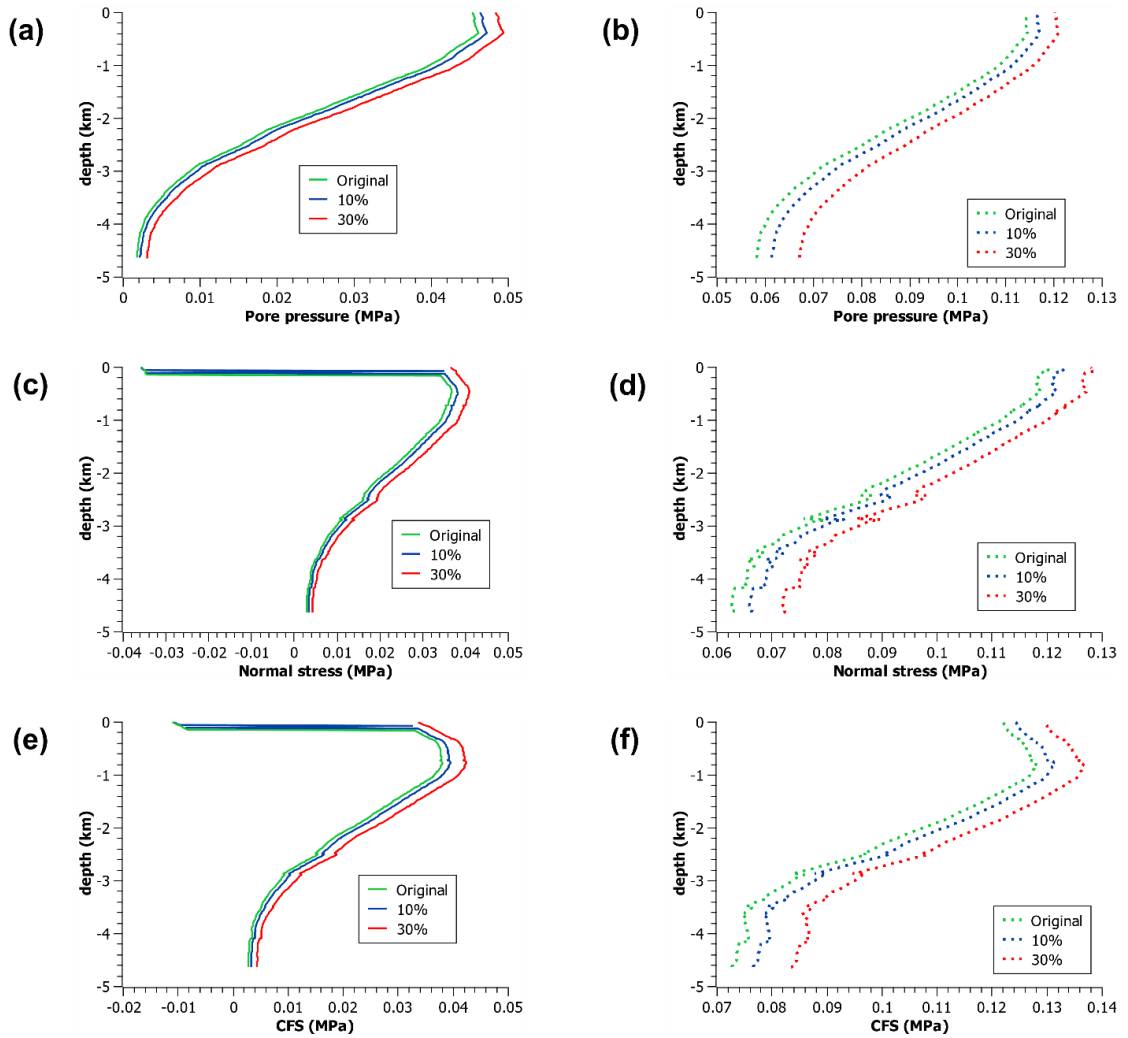
Figure 29. Comparison of pore pressure (a), normal stress (c), and CFS values (e) 5 years after impoundment if porosity and permeability were increased by 10% (blue line) and 30% (red line). A similar comparison 60 years after impoundment is shown in (b), (d), and (f).

5.2.3. Expected maximum earthquake magnitude

In order to calculate the potential maximum earthquake magnitude of a fault upon failure, Mcgarr (1976) came up with the following relation to estimate seismicity from the strain associated with a volume change:

$$\Sigma M_0 = k\mu|\Delta v| \qquad (10)$$

Where ΣM_0 is the sum of seismic moments of an earthquake population, k is a factor near 1 and taken as 1 in this study, μ is the rigidity modulus along the fault, and Δv is the change of volume resulting from ground deformation.

What is meant by a volume change is anything added or removed from the subsurface, such as the volume of injected water or volume of excavated rocks among others. In the case of water impounded behind dams, the pore pressure and normal stress changes induce a volume change along the fault zones that is used to estimate the maximum earthquake magnitude.

Equation (10) was validated in Mcgarr (1976) by comparing the calculated moment to the observed seismic moment from actual seismic data, which were found to be in good agreement. In addition, using Hanks and Kanamori (1979) relationship, the moment magnitude M_w can be calculated from M_0 (dyn.cm) by :

$$M_w = \frac{2}{3} log M_0 - 10.7 \qquad (11)$$

In order to calculate the change in volume (Δv), we divided the volumetric strain across the fault zones (computed in COMSOL Multiphysics) by the affected volume of the fault zone.

The Bisri dam causes a volumetric strain along the fault zones. This strain can be used to estimate the expected maximum earthquake magnitude using equations (10) and (11) over the simulation period.

Figure 30a shows the results for the Bisri Fault. The maximum magnitude reached is about 4.5 and takes place 2 years after impoundment. After that, the values start to decrease, meaning that the effects of initial impoundment start to diminish, signaling the
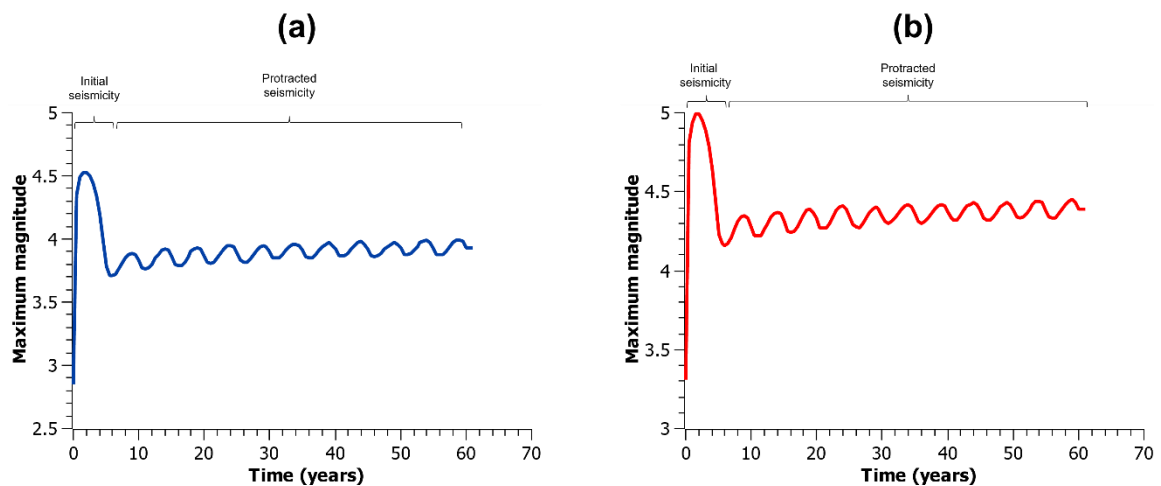
Figure 30. Expected maximum earthquake magnitude along the Bisri Fault (a), and the Roum Fault (b).

end of the initial seismicity. 6.5 years after impoundment, the values start to increase again, signaling the start of the protracted seismicity. The values are lower than in the case of initial seismicity, which is expected. The values oscillate with a period of 5 years, which is due to the time step taken during the simulation. Nevertheless, the values keep on increasing starting with a magnitude of 3.9 at 9 years and reaching a magnitude of 4 after 59 years of impoundment.

As for the Roum Fault, a similar behavior is observed but with higher values (Figure 30b). This is expected since the Roum Fault zone has a much larger volume than the Bisri Fault. Fault dimensions are an important factor controlling the expected earthquake magnitude along a certain fault (Wyss, 1979). This is why the Roum Fault has been a major concern even if it is farther than the Bisri Fault from the dam. Initial seismicity along the Roum Fault prevails for 2 years reaching a magnitude of 5 before it starts diminishing. The expected magnitude starts increasing again 5 years after impoundment signaling the start of protracted seismicity. During this period, the expected

maximum earthquake magnitude increases from 4.3 at 9 years after impoundment, to 4.4 at 59 years after impoundment. The plotted magnitudes are assuming that the faults have not ruptured before at the given times.

The Koyna dam (section 3.1.5.3) had a similar effect on nearby faults. The largest earthquake occurred around 5 years after impoundment and was associated with initial seismicity (Talwani, 1997). In addition, to this date, 22 events of magnitude 5, 220 events of magnitude 4, and thousands of smaller tremors have been induced by this dam (Gupta, 2022). Figure 31 shows that even several decades after the dam construction, earthquakes with magnitudes larger than 4 are still occurring due to this dam. Moreover, a similar behavior is observed at the XFJR dam (section 3.1.5.3), where the largest earthquake magnitude was associated with initial seismicity, and large earthquakes (M ≥ 4) keep on occurring even 60 years after the dam was built (Kuang et al., 2022; Figure 32).
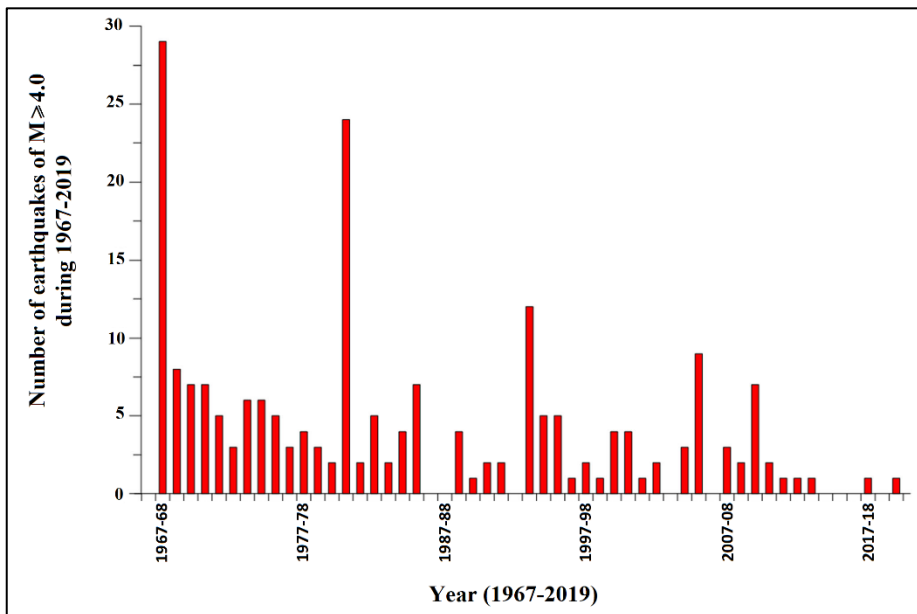
Figure 31. Annual number of earthquakes of an M ≥ 4 in the Koyna region for annual loading and unloading of the reservoir cycle. During the 1967–1968, there were a total of 38 earthquakes of an M ≥ 4 for the period 1 June 1967 to 31 May 1968. Modified from Gupta (2022).
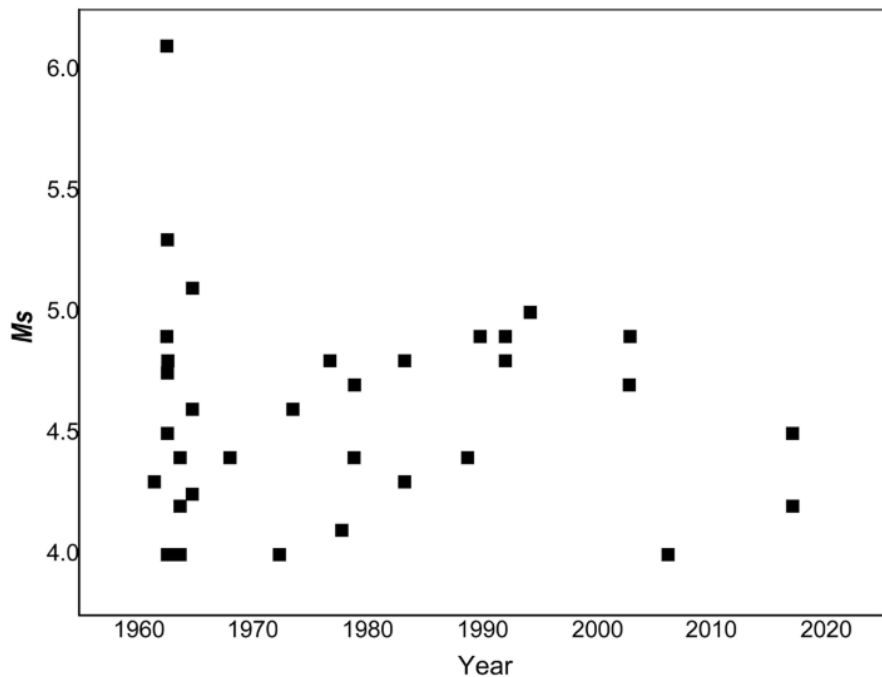
Figure 32. Distribution of earthquake magnitudes with time at the vicinity of the XFJR reservoir since its construction in 1960 and until 2020 (Kuang et al., 2022).

5.2.4. Implications for safety of humans and structures

The reactivation of the Bisri and Roum Faults has the potential to cause an earthquake especially since they are structurally interconnected (Nemer and Meghraoui, 2006; Nemer, 2019). The epicenters of three of the strongest seismic events that occurred in the twentieth century were located in the Roum Fault zone (Khair, 2001), one of which is the previously mentioned 16 March 1956 event (section 2.1). A repeat of such an event would cause extensive damage to the regions of Chouf, Jezzine, Saida and parts of the Beqaa as it has in the past where it killed 140 people, injured 500 others, destroyed 6000 houses, and damaged other infrastructure including roads (Adra, 2014). The safety of the region surrounding the proposed Bisri dam should be the priority, and the risk for induced seismicity should be taken into consideration very seriously by the authorities.

5.3. The Qaraoun dam 2D model

As shown in Figure 33a, the pore pressure increases with time; however, it has very low values (less than 0.04 MPa) compared to the Bisri reservoir case. The normal stresses are negative and decreasing further with time (Figure 33b) indicating compressional stresses, which have a stabilizing effect on faults. This shows that the probability of reservoir induced seismicity is low, which is also indicated by the negative CFS values along the fault (Figure 33c). After 62 years from impoundment, which represents the present-day state of the reservoir, the CFS values are negative, indicating that to this day there is no risk of induced seismicity caused by the Qaraoun Lake on the Yammouneh Fault. The latter result was expected due to the location of the Qaraoun Lake with respect to the strike-slip Yammouneh Fault, as strike-slip faults are generally destabilized when the oscillating reservoir is located directly over the fault (Roeloffs, 1988; Talwani, 1997). However, the location of the Qaraoun reservoir on one side of the Yammouneh Fault would not generate high risk for induced seismicity.

This section was published in Basbous et al. (2022) (Appendix II).

5.4. The Mseilha dam 2D model

The results of the modeling of the Mseilha dam show positive (tensile) normal stresses that increase with time (Figure 34a). The pore pressure values are positive and increasing with time as well, whereby the rate of increase at depth is larger due to pore pressure diffusion (Figure 34b). The resulting CFS values are likewise positive and increasing with time, surpassing the threshold of 0.1 MPa, and indicating a risk for induced seismicity (Figure 34c). The results resemble those of the Bisri dam (Figure 19),

but the values are smaller, which is expected since only a part of the Mseilha reservoir is directly over a part of the Batroun Fault damage zone, unlike the Bisri case where the entire Bisri reservoir would cover the Bisri Fault. In addition, the water level of the Mseilha reservoir is nearly half that of the Bisri reservoir.
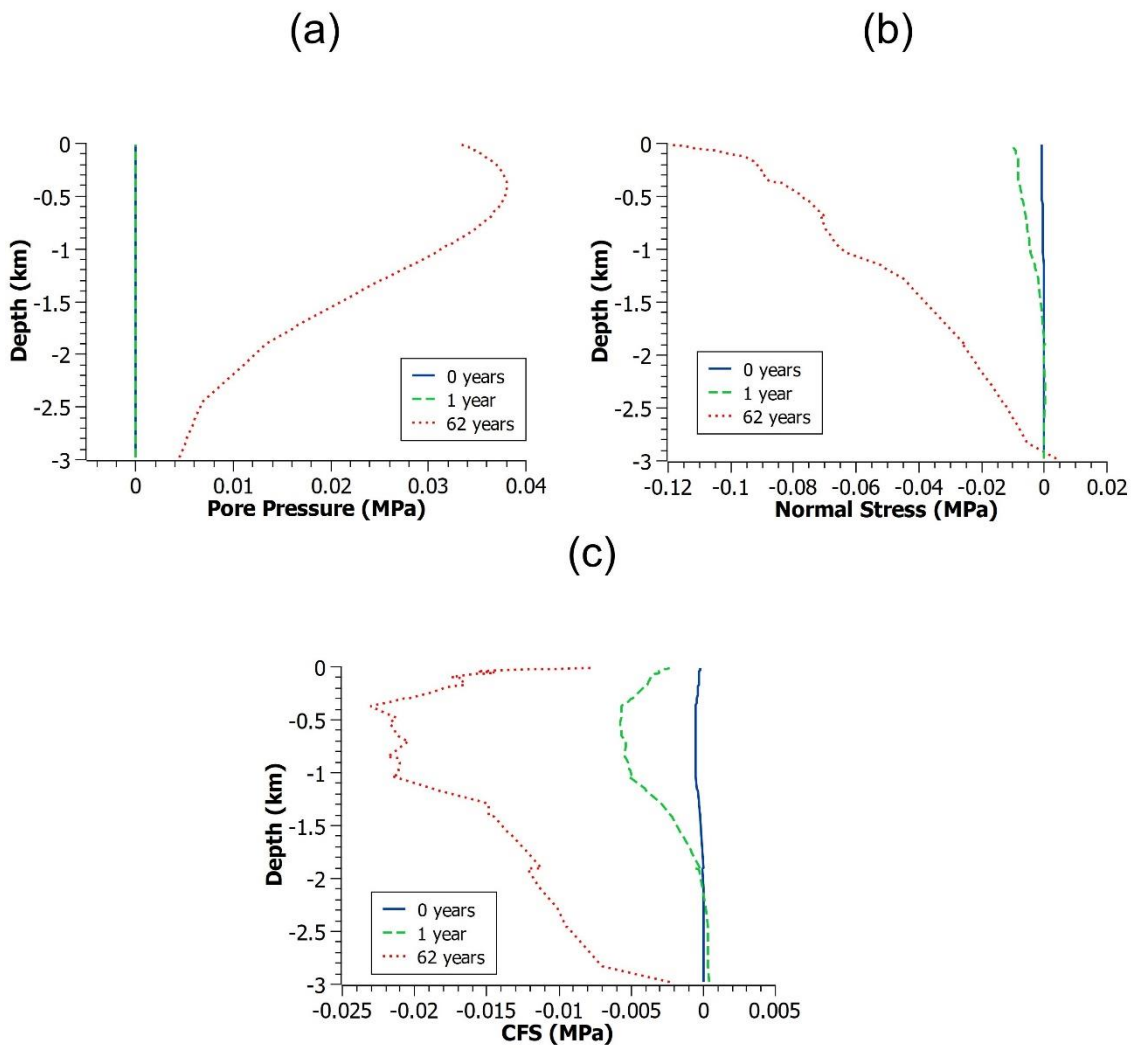
Figure 33. Variation of the pore pressure (a), normal stress (b), and CFS (c) along the Yammouneh Fault at 0 year (blue), 1 year (green), and 62 years (red) after impoundment of the Qaraoun Lake.
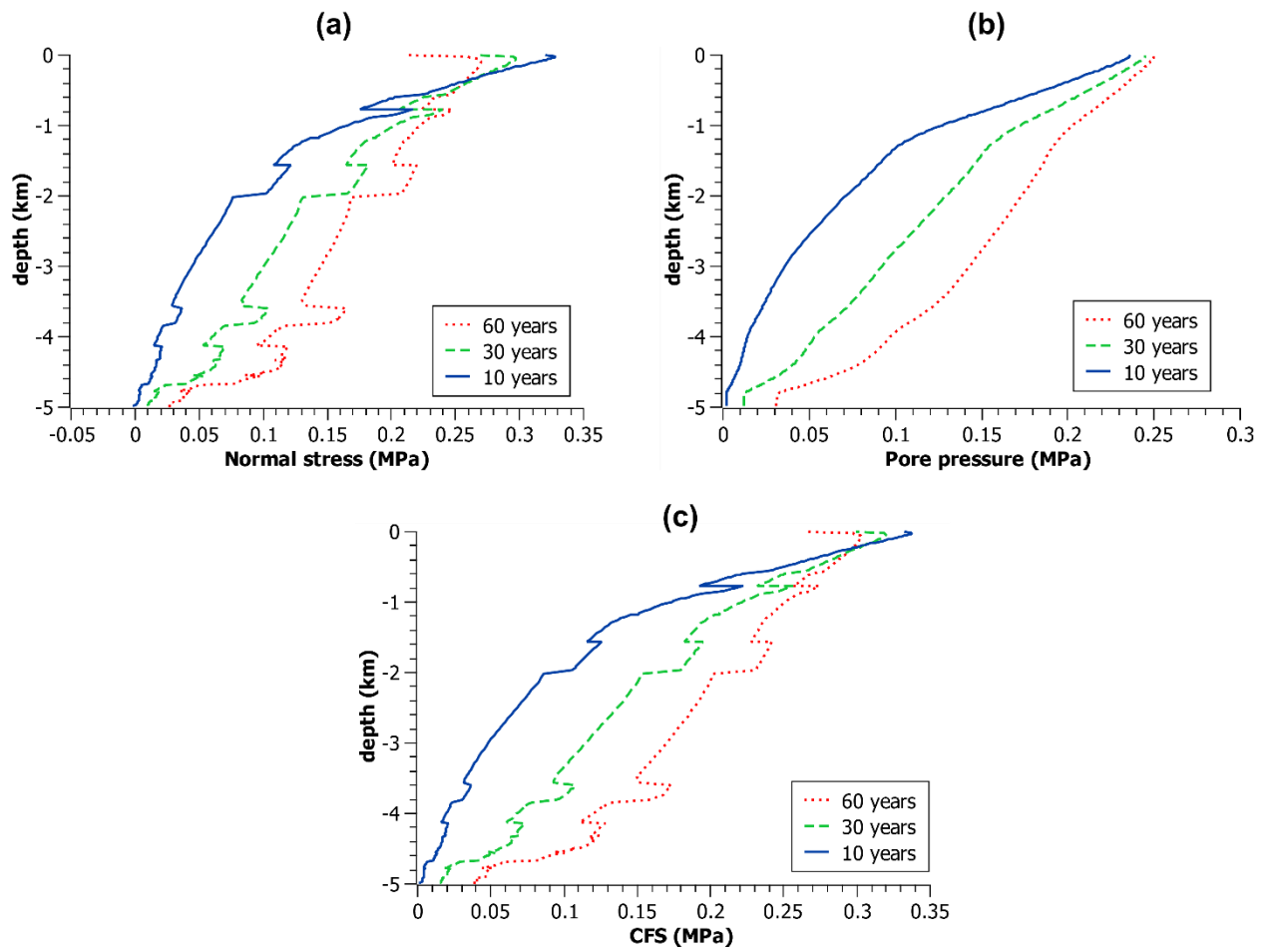
Figure 34. Variation of normal stress (a), pore pressure (b), and CFS (c) along the Batroun Fault.

CHAPTER 6

CONCLUSIONS

This thesis aimed at providing an understanding of the risk of building dams and impounding water in certain areas without taking into consideration the presence of faults in those areas. We studied the reservoir induced seismicity of the planned Bisri reservoir and of the existing Qaraoun and Mseilha reservoirs, in order to understand the potential effect of those reservoirs on the activation of nearby faults.

Our results emphasized the danger of reservoir induced seismicity in Lebanon, and the importance of assessing the risk and conducting proper studies before proceeding with dam projects that can disturb the background stresses in the subsurface and generate earthquakes.

The location of the planned Bisri reservoir directly over the dip-slip Bisri Fault that is connected to the Roum Fault makes the risk of reservoir induced seismicity very high. In effect, the expected pore pressure and tensile normal stresses caused by the Bisri reservoir on the Bisri and the Roum Faults will have a high probability of activating these two faults. This is indicated by the high and positive CFS values (exceeding 0.1 MPa along both faults), the increase in the seismicity rates, and the expected maximum earthquake magnitudes that range between 3.8 and 4.5 along the Bisri Fault and between 4.3 and 5 along the Roum Fault.

On the contrary, to this day, there has been no risk of induced seismicity caused by the Qaraoun Lake on the Yammouneh Fault, mainly because the Qaraoun Lake is located on one side of the fault, and the estimated CFS values are either negative or

negligible. Therefore, the cases of the Bisri and Qaraoun dams in Lebanon are different, whereby it is evident that the Bisri dam would be in an extremely critical area where induced seismicity would be very likely, which puts thousands of people and structures at risk.

As for the Mseilha dam, it presents a risk of induced seismicity along the Batroun Fault. The risk is lower than that of the Bisri dam because in the Mseilha case, the reservoir overlies a part of the damage zone of the fault, and the water level is much lower than that of the Bisri reservoir. Nevertheless, it must be taken into account that all the concerned faults are critical structures, and no major human activities should be undertaken in their vicinity, as the current natural stresses along those faults can be changed and lead to their activation.

Accordingly, based on the presented modeling results in this thesis, it is highly recommended that, before proceeding with any major dam project in Lebanon that can lead to disturbing the state of stresses in the subsurface, seismic hazard assessments must be performed in order to properly evaluate the risk of reservoir induced seismicity along nearby faults. Those faults may be critically stressed and should not be artificially disturbed.

APPENDIX I

LIST OF DAM PROJECTS CORRELATED WITH INDUCED SEISMICITY (AFTER HUMAN-INDUCED EARTHQUAKE DATABASE, HIQUAKE)

Country	Dam name	Start date	Observed maximum magnitude (Mmax)	Year of Mmax	Dam height (m)	Volume (10^6 m3)
USA	Lake Hebgen, Montana	1915	7.1	1959	19	994
India	Gandipet (Osman Sagar)	1920	3.5	1982	36	117
France	Serre-Poncen	1925	3.3	1966		1270
France	Eguzon	1926	3.5		61	
Greece	Marathon	1929	5.7	1938	67	41
Algeria	Oued Fodda	1932	3	1933	101	225
USA	Hoover Dam (Lake Mead)	1935	5	1939	221	36703
USA	Shasta, California	1944	3	1944	183	5615
USA	Anderson, Idaho	1950	4.7	1973	72	111
USA	Coyote Valley (Anderson Dam), California	1950	5.2	1962	72	113
USA	Clark Hill, South Carolina/Georgia	1952	4.3	1974	60	3517
Brazil	Carmo do Cajuru	1954	3.7	1972	23	192
China	Foziling	1954	4.5	1973	74	470
New Zealand	Lake Pukaki	1955	4.6	1978	106	9000
Australia	Eucumbene	1957	5	1959	116	4761
USA	Palisades, Idaho	1957	3.7	1966	82	1500

Country	Dam name	Start date	Observed maximum magnitude (Mmax)	Year of Mmax	Dam height (m)	Volume (10⁶ m3)
USA	Kerr, Montana	1958	4.9	1971	60	1505
Zambia–Zimbabwe	Kariba	1958	6.2	1963	128	152600
Japan	Arimine	1959	3.5		140	222
China	Xinfengjiang (XFJR)	1959	6.1	1962	105	13896
Spain	Camarillas	1960	4.1	1964	49	37
Spain	Canelles	1960	4.7	1962	150	678
Japan	Kurobe	1960	4.9	1961	186	149
Italy	Vajont	1960	3	1960	262	150
Australia	Warragamba (Varragamba)	1960	5.5	1973	142	2031
India	Koyna	1962	6.3	1967	103	2780
France	Monteynard	1962	5.3	1962	155	309
India	Rihand	1962	3		92	10600
Iran	Sefia Rud	1962	4.7	1968	106	1820
Switzerland	Contra	1963	3	1965	220	86
Italy	Pertusillio	1963	2.1		95	155
Egypt	Aswan	1964	5.7	1981	111	164000
New Zealand	Benmore	1964	5	1966	110	2040
Japan	Yuda	1964	3.5			
Ghana	Akosombo	1965	5.3	1964	114	148000
Greece	Kremasta	1965	6.2	1966	160	4750
USA	Lake Meredith	1965	4.1	1966		
Canada	Manicouagan 2, Quebec	1965	3.7	1965	90	340
Italy	Piastra	1965	4.4	1966	93	13

Country	Dam name	Start date	Observed maximum magnitude (Mmax)	Year of Mmax	Dam height (m)	Volume (10⁶ m3)
Serbia	Bajina Basta	1966	4.9	1967	90	340
China	Danjiangkou	1967	4.7	1973	97	16000
Bosnia and Herzegovina	Grancarevo	1967	3	1967	123	1280
Pakistan	Mangla	1967	3.6	1967	135	7200
India	Nagarjuna Sagar	1967	3.5		124	11560
USA	Oroville, California	1967	5.8	1975	236	4400
Australia	Blowering	1968	3.5	1973	112	1628
Greece	Kastraki	1968	4.6	1969	96	1000
France	Vouglans	1968	4.5	1971	130	592
Brazil	Jaguari	1969	3	1985	67	1500
China	Nanchong	1969	2.8	1974	45	15
China	Nanshui	1969	2.3	1970	81	1220
Spain	Almendra	1970	2	1972	202	2500
Brazil	Capivari-Cachoeira	1970	3	1971	61	180
South Africa	Hendrik Verwoerd (Gariep)	1970	2	1971	66	5000
China	Huangshi	1970	2.3	1974	40	610
Japan	Kamafusa	1970	3	1970	47	45
China	Qianjin	1970	3	1971	50	20
Austria	Schlegeis	1970	2	1973	117	128
Uzbekistan	Charvak	1971	5.3	1977	148	2000
USA	Heron, New Mexico	1971	2.7		82	494
USA	Jocassee, South Carolina	1971	3.9	1979	107	1431

Country	Dam name	Start date	Observed maximum magnitude (Mmax)	Year of Mmax	Dam height (m)	Volume (10^6 m3)
Australia	Talbingo	1971	3.5	1973	162	935
India	Mula	1972	1.5	1972	56	1017
Tadjikistan	Nurek	1972	4.6	1972	317	1000
China	Shenwo/Shenwu	1972	5.2	1974	50	540
India	Ukai	1972	3		81	7414
China	Zhelin	1972	3.2	1972	62	7170
Switzerland	Emosson	1973	3.5	1974	180	225
Turkey	Keban	1973	3.5	1973	212	31000
Canada	McNaughton (Mica)	1973	4.7	1973	191	25000
Canada	Mica	1973	4.1	1974	240	24762
Brazil	Porto Colômbia-Volta Grande	1973	4.2	1974	40 and 45	1460
Kyrgyzstan	Toktogul	1973	4.6	1977	215	19500
Thailand	Tsengwen (Zengwen)	1973	3		128	708
Greece	Polyphyto	1974	6.6	1995	112	1220
Pakistan	Tarbela	1974	3		143	13700
Armenia	Tolors	1974	4.2	1982	69	96
India	Idukki	1975	3.5	1977	169	1996
Canada	Manicouagan 3, Quebec	1975	4.1	1975	108	10423
Brazil	Marimbondo	1975	2	1978	90	6150
France	Sainte-Croix	1975	2.2			767
Brazil	Capivara	1976	3.7	1979	60	10500
Brazil	Paraibuna–Paraitinga	1976	3	1977	98 and 104	4740
India	Bhatsa	1977	4.9	1983	88.5	947
Zambia	Itezhi-Tezhi	1977	4.4	1984	62	3900

Country	Dam name	Start date	Observed maximum magnitude (Mmax)	Year of Mmax	Dam height (m)	Volume (10^6 m3)
Brazil	Sobradinho	1977	1.9	1979	43	34100
USA	Monticello (Fairfield), California	1977	2.9	1978	129	500
Thailand	Srinagarind	1977	5.9	1983	140	11750
Georgia	Enguri (Inguri)	1978	4.7		271.5	1093
Albania	Fierza	1978	2.6	1981	167	2800
Canada	LG 2, Quebec	1978	0.9	1979	145	61700
China	Hunanzhen	1979	2.8	1979	129	2060
Japan	Takase	1979	2.7	1982	176	11
China	Wujiangdu	1979	3.4	1985	165	2140
China	Shengjiaxia (Shenjia Xiashuiku)	1980	3.6	1984	35	4
Brazil	Emborcação	1981	2	1984	158	17500
Canada	LG 3, Quebec	1981	3.7	1983	80	30000
Greece	Pournari	1981	5.6	1981		
Italy	Ridracoli	1981	3.5	1988	103	33
China	Dahua	1982	4.5	1993	74.5	420
India	Dhamni	1983	3.8	1994	59	285
India	Sriramsagar	1983	3.2	1984	43	32000
Australia	Thomson	1983	5	1996	165	1100
Greece	Asomata	1984	5.4	1984		
Brazil	Tucuruí	1984	3.6	1998	106	45800
Brazil	Xingó	1984	1.7	1994	140	3800
Brazil	Açu	1985	3	1994	31	2400
Albania	Komani	1985	4.2	1986	130	1600
Greece	Sfikia	1985	5.2	1986		

Country	Dam name	Start date	Observed maximum magnitude (Mmax)	Year of Mmax	Dam height (m)	Volume (10⁶ m3)
China	Dongjing/Dongqing	1986	4.4	2010	150	955
Brazil	Balbina	1987	3.4	1990	42	17500
India	Warna (Warana)	1987	5	1993	80	1260
Vietnam	Hoa Binh	1988	4.9	1989	125	
China	Lubuge	1988	3.4	1988	103	110
India	Kadana	1989	2.5		66	1203
Turkey	Atatürk	1990	5.5	2017	169	48700
India	Killari	1990	6.1	1993	20	125
Italy	Montedoglio	1990	4.3	2001		
Spain	Tous New	1990	4	2000	102.5	700
China	Tongjiezi	1992	2.9	1992	74	30
China	Yantan	1992	3.5	1994	110	2430
Brazil	Nova Ponte	1993	4	1998	142	12800
China	Shuikou	1993	3.2	1994	101	2350
Mexico	Cuchillo, Nuevo León	1994	4.5	2013	42	1785
France	Caramany	1995	3.3			26
Poland	Czorsztyn Lake	1995	3.5	2013	56	234
Lesotho	Katse	1995	3.1	1996	185	1950
Brazil	Serra da Mesa	1996	2.2	1999	150	54400
Brazil	Miranda	1997	2.4	1998	85	1140
Canada	SM 3, Quebec	1998	2.2	2000	171	12500
Brazil	Itá	1999	2.5	1999	130	5100
Brazil	Machadinho	2001	1.8	2001	130	3300
Brazil	Funil	2002	3.2	2011	50	260
Brazil	Itapebi	2002	1.5	2003	117	1000

Country	Dam name	Start date	Observed maximum magnitude (Mmax)	Year of Mmax	Dam height (m)	Volume (10^6 m3)
Brazil	Castanhão	2003	2.3		85	6700
China	Three Gorges	2003	5.1	2013	181	39300
Iran	Karun III	2004	4.3	2006	185	2970
Brazil	Barra Grande	2005	2.5	2005	190	5200
Brazil	Campos Novos	2005	1.8	2005	166	1500
Brazil	Irapé	2005	3	2006	208	5960
Canada	Toulnustouc	2005	1.6	2005	77	3500
China	Zipingpu (Wenchuan earthquake)	2005	7.8	2008	156	1000
China	Longtan	2006	4.2	2007	200	27270
China	Xiaowan	2008	3.9	2012	300	14500
Vietnam	Son La	2010	4.4	2014	137	9260
Vietnam	Song Tranh 2	2010	4.7	2012		740
Costa Rica	Pirrís reservoir	2011	4.8	2014	113	36
China	Xiluodo	2013	5.1	2014	285.5	
Brazil	Jirau	2014	3.2	2014	62	2730
Canada	RO 2	2014	3.1		109	3720
Canada	RO 3	2017	1.6		95	1878
Russia	Bratsk		4.2	1996	100	169
USA	Cabin Creek, Colorado		2	1968		
Italy	Campotosto		5.7	1950		230
Japan	Hitotsuse		3.5		130	261
Romania	Ievorul Muntelui-Bicaz		2			
USA	Keowee, South Carolina		3.8	1971		

Country	Dam name	Start date	Observed maximum magnitude (Mmax)	Year of Mmax	Dam height (m)	Volume (10^6 m3)
Spain	Itoiz		4.6	2004	111	418
India	Kinnersani		5.3	1969		
Cyprus	Kouris		3	1994		
Japan	Kuzuryu		3.5		128	353
Switzerland	Lac de Salanfe		3.5	1953		
Russia	Lake Baikal		4.8			
Japan	Makio		3.5			
India	Mangalam		3	1963		
Japan	Midono		3.5			
Japan	Miomote		3.5			
Japan	Nagawado		3.5			
Japan	Narugo		3.5			
Japan	Ohkura		3.5			
India	Parambikulam		3			69
Italy	Pieve de Cadore		4.4	1960		
India	Sharavathi (Sharavati)		2			
India	Sholayar		2			
Japan	Tohri (Tori)		3.5			
Japan	Uchikawa		3.5			
Romania	Vidra Lotru		2.8			
Romania	Vidraru-Arges		2.8			480
Paraguay	Yacyreta		3.9	2000		

APPENDIX II

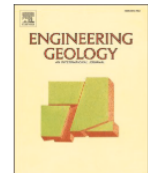# ASSESSING THE POTENTIAL FOR RESERVOIR INDUCED SEISMICITY FROM THE BISRI DAM PROJECT IN LEBANON

Assessing the potential for reservoir induced seismicity from the Bisri dam project in Lebanon

J. Basbous [a], T.S. Nemer [a], A. Yehya [b,c,*], E. Maalouf [d,**]

[a] Department of Geology, Faculty of Arts and Sciences, American University of Beirut, Lebanon
[b] Department of Civil and Environmental Engineering, Maroun Semaan Faculty of Engineering and Architecture, American University of Beirut, Lebanon
[c] Harvard John A. Paulson School of Engineering and Applied Sciences, Harvard University, USA
[d] Baha and Walid Bassatne Department of Chemical Engineering and Advanced Energy, Maroun Semaan Faculty of Engineering and Architecture, American University of Beirut, Lebanon

A B S T R A C T

Reservoir induced seismicity has been observed in multiple cases around the world. The Bisri dam project, planned to be constructed in the Bisri Valley in Lebanon, has overlooked the concerns for safety raised by experts, which puts thousands of people and various structures at risk. In this paper, we study the potential for reservoir induced seismicity from this project. We use a two-dimensional poroelastic model where fluid flow and solid deformation are coupled to estimate the change in Coulomb Failure Stress (CFS) and the rate of seismicity (R). The high permeability damage zone of the Bisri fault lies directly beneath the proposed reservoir, which allows the pore pressure to diffuse into deeper levels, decreasing the effective normal stress, destabilizing the fault, and increasing the seismicity rate. Our results show that the increase in the rate of seismicity remains decades after the initial impoundment indicating a high risk for protracted seismicity. Moreover, the activation of the Bisri fault can cause the reactivation of the Roum fault, which is a major and active branch of the Dead Sea Transform Fault that hosted the epicenters of recent and major seismic events in the region. Hence, the risk for induced seismicity from the Bisri project should be taken into consideration very seriously by the authorities.

1. Introduction

Lebanon lies within a region of high seismic potential where large-magnitude seismic events have been recorded historically (Ambraseys and Jackson, 1998). The Dead Sea Transform Fault (DSTF) is a plate boundary separating the African and Arabian plates along which there is a left-lateral movement. It passes through the entire country of Lebanon where it bends, forming the NNE-trending Lebanese Restraining Bend (LRB) (Hancock and Atiya, 1979). The DSTF branches within this bend into the Yammouneh Fault, which is the main branch, and three other auxiliary branches that are the Roum Fault, the Serghaya Fault, and the Rachaya Fault that are all active faults (Fig. 1) (e.g. Gomez et al., 2003; Nemer et al., 2008a, 2008b; Nemer and Meghraoui, 2006). The Yammouneh Fault is an active fault that extends for 170 km along the LRB and accommodates most of the DSTF motion in a predominantly left-

lateral strike-slip movement. However, no recent major seismic events were related to this fault (Nemer et al., 2008a). The Roum Fault is 35 km long, extends from north of the Hula basin into the Awali River, and accommodates a left-lateral movement as well as a vertical movement that is most prominent in its northern part. This fault is an active seismogenic structure and was the source of multiple large seismic events, including the 16 March 1956 (ML 5.8) earthquake and the 1 January 1837 (Ms 7.1) earthquake, which indicates that it has the potential of large seismic hazard (Nemer and Meghraoui, 2006).

According to the *Bureau Technique pour le Developpement*, a geophysical electrical resistivity survey conducted in the Bisri Valley reported the presence of the east-west striking Bisri Fault that accommodates a tear-like movement (Nemer, 2019). This fault is structurally interrelated to the Roum Fault where the northern segment of the latter intersects the former at an obtuse angle (Fig. 2). In addition, the 16

* Corresponding author at: Department of Civil and Environmental Engineering, Maroun Semaan Faculty of Engineering and Architecture, American University of Beirut, Lebanon.
** Corresponding author at: Baha and Walid Bassatne Department of Chemical Engineering and Advanced Energy, Maroun Semaan Faculty of Engineering and Architecture, American University of Beirut, Lebanon.
E-mail addresses: ay36@aub.edu.lb (A. Yehya), em40@aub.edu.lb (E. Maalouf).

March 1956 earthquake (ML 5.8) epicenter was projected into this interconnection area (Annales Seismologiques de l'Observatoire de Ksara, 1956–1958; Nemer, 2019). In a country like Lebanon, prone to natural and negligence-associated catastrophic events, the latest being the Beirut explosion (Nemer, 2021), it is crucial for research institutions to study and assess the risks of a project proposed by the government, which overlooked the concerns and hazards raised by experts (Nemer, 2019).

In this paper, we analyze the risk of induced seismicity from the Bisri dam that is proposed to be constructed in the Bisri Valley, overlying a large section of the Bisri Fault and close to the Roum Fault. The dam is planned to be built in a critical area that is tectonically active and geologically complex (Nemer, 2019). The paper is organized as follows. In Section 2, the location, dimensions, and geology of the area are described, and the need for the Bisri dam is discussed. Moreover, the model description and the parameters used are given. Section 3 presents the main concepts of reservoir induced seismicity, the poroelastic model, and the governing equations. Section 4 sums up the results and discussions, provides a comparison between the Bisri case and Qaraoun case, the latter being related to an existing dam in Lebanon, and includes a calculation of the rate of seismicity.

2. Material and methods

We build a fully coupled two-dimensional (2D) finite element poroelastic model containing the lithological formations, the Bisri Fault and its damage zone, and the planned reservoir that has an oscillating water level. The coupled model simulates the feedback between fluid flow and rock deformation to estimate the change in the overall Coulomb stresses and evaluate the rate of seismicity. The analysis of the seismicity rate is based on Dieterich (1994) and governed by rate and state friction where a population of earthquake sources accelerate toward instability under the effect of stress perturbation.

2.1. The Bisri dam project

The Bisri dam project is planned to secure clean water for the Greater Beirut and Mount Lebanon area residents (who account for over 1.6 million people), and to reduce their water expenditure. As such, they would no longer need to use alternative water resources like wells, which will in turn decrease coastal salt-water intrusion and restore Beirut's groundwater. In addition, the locals will benefit from many projects and new sources of income like ecotourism and others (The World Bank, 2021).

The proposed Bisri dam is located on the Bisri River that is formed by the Barouk River from the north and merging with Aaray River from the
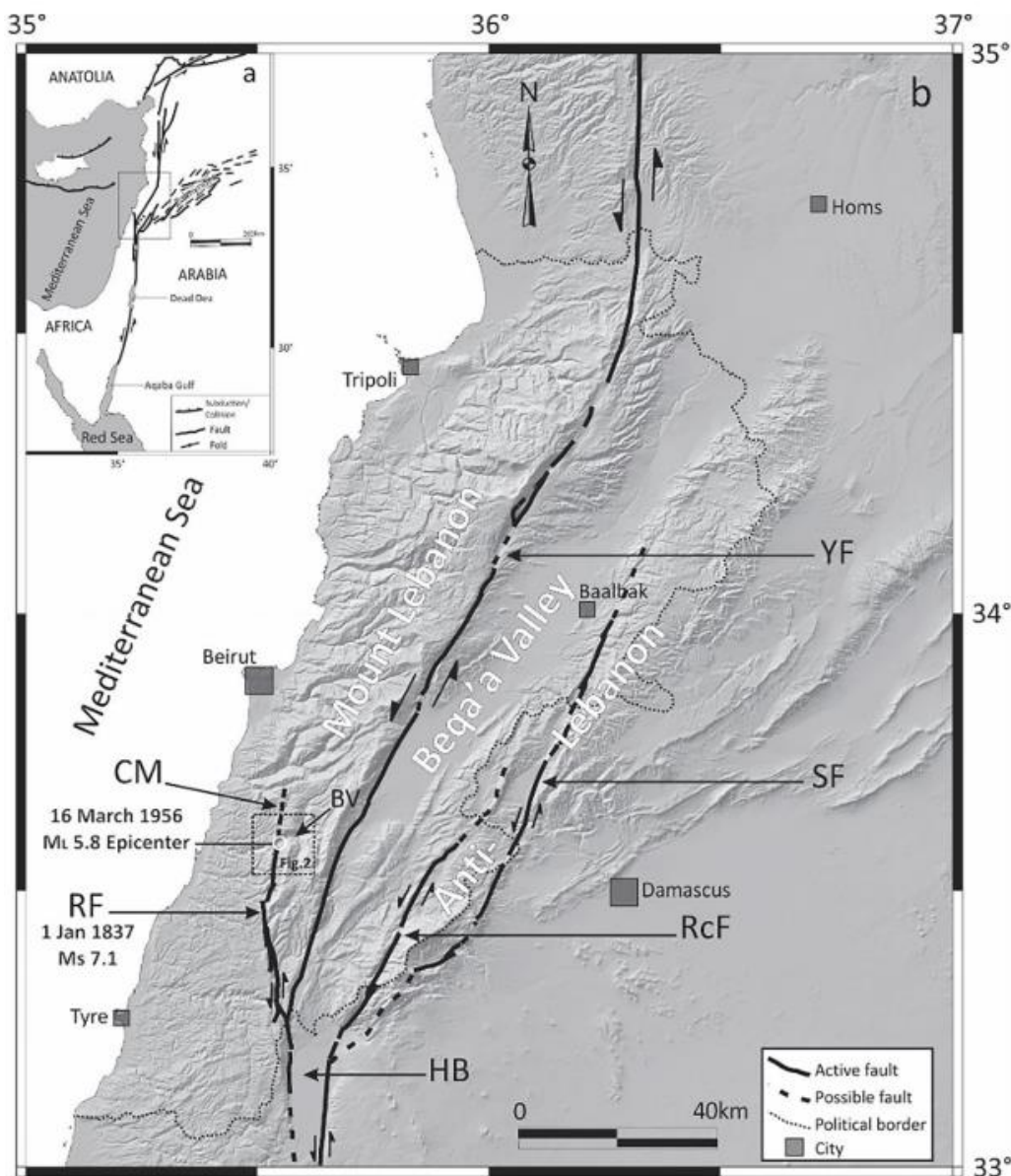
Fig. 1. (a) Arabia and Africa separated by The Dead Sea Transform Fault. (b) Shuttle Radar Topography Mission 90-m-resolution digital elevation model of the Lebanese Restraining Bend showing the main units and structures: BV, Bisri Valley; CM, Chouf monocline; HB, Hula basin; RcF, Rachaya Fault; RF, Roum Fault; SF, Serghaya Fault; YF, Yammouneh Fault. Note the epicenter location of the 1956 earthquake along the Roum Fault that was also associated with the 1837 earthquake. The box delineates the location of Fig. 2. Modified from Nemer (2019).

south. The dam is located about 35 km south of central Beirut, and the reservoir is expected to extend about 4 km upstream of the dam axis. Above the dam, the water surface catchment area extends to about 215 km^2. The maximum height of the dam is 73 m, and the length of the reservoir is 6 km with two 2-km branches, and its width is about 0.5 km (Fig. 2). The area to be inundated is around 4.34 km^2 where the expected maximum water level is at 467 masl, and the minimum water level is at about 420 masl, with an average storage volume of 0.125 km^3 (Council for Development and Reconstruction, 2014).

As for the geology of the area, the exposed stratigraphic section of the reservoir is comprised of the Cretaceous formations, namely the clastic fine grained Chouf Formation (C1) that is the most widely spread, along with the Abieh (C2a), Mdeirej (C2b), Hammana (C3) and Sannine (C4) formations forming interbedded limestones and marls. The Jurassic formations are exposed in limited parts of the area shown in Fig. 2 of Nemer (2019), and they consist of the Bikfaya (J6) and Bhannes (J5) formations consisting mainly of micritic limestone, and the Kesrouane Formation (J4) formed of cliff forming limestones and dolostones. The exposed limestone rocks are found to be highly fractured and karstified (Council For Development and Reconstruction, 2014).

2.2. Model construction

The lithologies of the layers below the Kesrouane Formation were taken from the general chronostratigraphic chart of the Levant margin (Nader et al., 2018), and the parameters used were approximated from acoustic and petrophysical investigations done on core samples collected from different exposed formations at several locations in Lebanon (Salah et al., 2020a, 2020b, 2020c; Salah et al., 2018). The parameters for the deep marine siliciclastic rocks were taken from layers with similar lithologies in the Levant Basin (Marlow et al., 2011), and the parameters for the evaporite layers were taken from Jackson and Hudec (2017), since no local information were available on such rock types. Fan et al. (2019) divided the layers of the region into caprock, overburden and reservoir rocks having a Biot coefficient between 0.7 and 0.79, and crystalline rocks having a Biot coefficient of 0.44. As such, due to the lack of available information for this model, the Biot coefficient is taken as 0.75 for all the sedimentary layers except for the evaporite layer since it is composed of crystalline rocks where the Biot coefficient is taken as 0.44. The simulation parameters used in our model are gathered in Table 1. Fig. 3 shows a 2D cross-section including the Bisri Fault, its damage zone, the Bisri reservoir and the successive lithologic layers.

Generally, fault cores are surrounded by high permeability damage zones that are highly deformed and fractured (Mitchell and Faulkner, 2009). This is a plausible assumption for active faults if microcrack healing, which is usually thermally enhanced and fluid-assisted (Yehya and Rice, 2020), did not occur during the inter-seismic cycle (Yang et al., 2021). According to the Council for Development and Reconstruction (2014), fractured and well jointed limestones are present in the vicinity of the proposed dam, which suggests that the Bisri Fault has a damage zone. A limitation of our model is that the joints and fractures present in the damage zones are not explicitly added, rather, we use average porosity and permeability values, which are taken higher in the damage zones relative to the host rocks. We assume that the cracks within the damage zone partially close when the effective normal stress increasesTherefore, we assume that the permeability of the damage zone decreases with depth. In the model, the porosity of the damage zone is taken as 18% and the permeability as 2 mD, both decreasing linearly with depth to reach the value of the surrounding host rocks. However, for active faults there could be open fractures along the fault that will locally increase the permeability and enhance diffusion, and further increase the estimated risk of seismicity. In addition, rocks in the damage zone are characterized by a lower Young's modulus than the
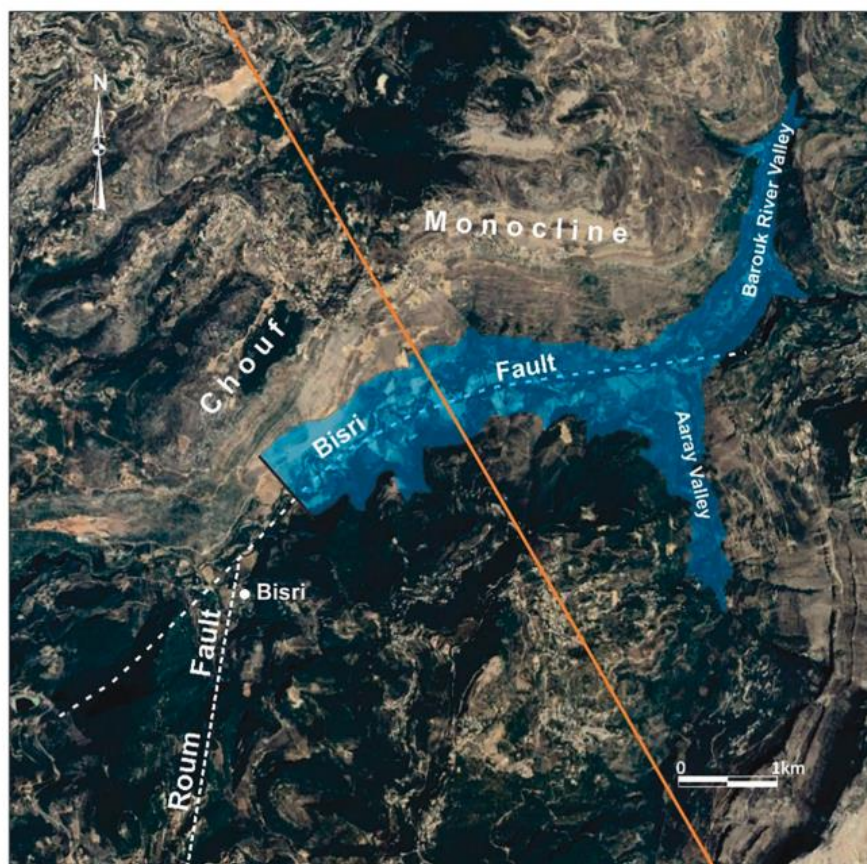

Fig. 2. Aerial view of the Bisri Valley showing the proposed Bisri reservoir, as well as the Roum, and Bisri faults modified from Nemer (2019). The orange line represents the location along which the 2D section in Fig. 3 was constructed.

Table 1
Hydro-mechanical properties of the lithologic layers present at the dam site.

|	Sedimentary Layer	Porosity (fraction)	Permeability (mD)	Bulk Density (kg/m³)	Drained Poisson's Ratio	Young's Modulus (GPa)
1	Sannine Formation	9.40E-04	0.01	2487	0.26	38
2 / 13	Hammana Formation / Marly Limestone	1.80E-03	0.04	2315	0.24	25.2
3 / 10	Mdeirej Formation / Shallow Marine Limestone	0.15	1.75	2630	0.24	70
4	Abieh Formation	0.07	0.25	2730	0.235	60
5 / 12	Chouf Formation / continental deposits	0.15	1.75	2770	0.26	45
6	Bikfaya / Bhannes Formation	0.023	0.043	2660	0.31	61
7 / 9	Kesrouane Formation / Dolomitic Limestone	0.033	0.07	2715	0.2	30
11	Deep Marine siliciclastic rocks	0.001	1.00E-02	2460	0.26	20
8	Evaporites	0.0075	1.00E-05	2165	0.265	44.4
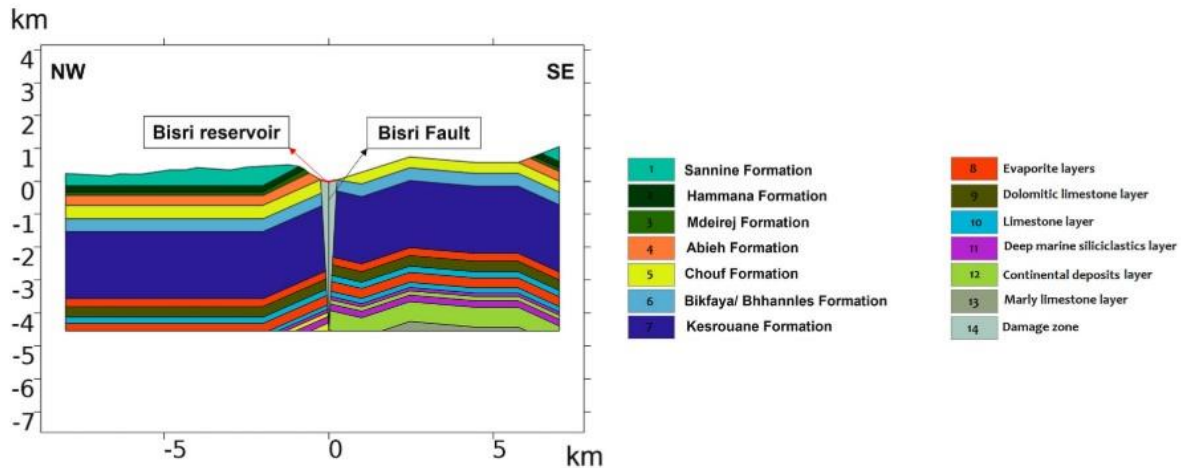
Fig. 3. 2D cross-section taken along the orange line in Fig. 2, and showing the Bisri Fault, its damage zone, and the adjacent country rocks. The origin is taken at the surface where the Bisri Fault is located so that the negative values on the x-axis indicate the distance Northwest of the Bisri Fault, positive values indicate the distance Southeast of the Bisri Fault, and the negative values on the y-axis indicate the depth below the surface.

adjacent country rocks due to higher fracture density (Gudmundsson, 2004; Yehya et al., 2018), therefore, this parameter was decreased by 5 GPa for the damage zone rocks with respect to their corresponding host rocks (Cappa and Rutqvist, 2011; Faulkner et al., 2006; Yehya et al., 2018). The shape of the fault damage zone follows a flower like structure, where the width and fracture density decrease as we go downwards (Ampuero and Mao, 2017; Stefanov and Bakeev, 2015).

To simulate the oscillating dam reservoir, minimum and maximum pressures are applied at the surface corresponding to 13 m and 60 m water levels, respectively, with a lag time of six months in between

(Fig. 4). The pressures are calculated by $p = \rho g h$, where p is the pressure of the water column, ρ is the density of water that is 997 kg/m³, g is the acceleration due to gravity that is 9.8 m/s², and h is the height of the water column. The dam reservoir is expected to fill up naturally during the rainy season that extends for six months (winter and spring), and the accumulated water is to be used during the dry season over the following six months (summer and fall) (Council For Development and Reconstruction, 2014). Hence, the lag time is taken to reflect this assumption.

3. Theory and calculations

3.1. Reservoir induced seismicity (RIS)

Water impounded behind dams has proven to induce seismicity in many cases around the world, several of which have caused extensive damage as in Hsinfengkiang, China; Kremasta, Greece; Kariba, Zambia; Oroville, California, and many others (e.g. Gupta, 1992; Pavlin and Langston, 1983; Tsung-ho et al., 1976). It should be noted that the term "triggered seismicity" is more appropriate in these cases since it involves stress changes that are only a portion of the ambient stresses, while "induced seismicity" involves stress changes that are comparable in magnitude to the ones that can cause slip along faults (McGarr et al., 2002). Nevertheless, "triggered seismicity" is one type of the more general term "induced seismicity" (Mulargia and Bizzarri, 2014). The latter has been used by most authors to describe incremental stress changes that build up to cause failure along faults (e.g., Gupta, 1992; Gupta and Combs, 1976; Kuang et al., 2022; Pavlin and Langston, 1983; Ramasamy et al., 2019; Talwani, 1997; Talwani and Acree, 1984). As such, the seismicity caused by the Bisri dam will be referred to as
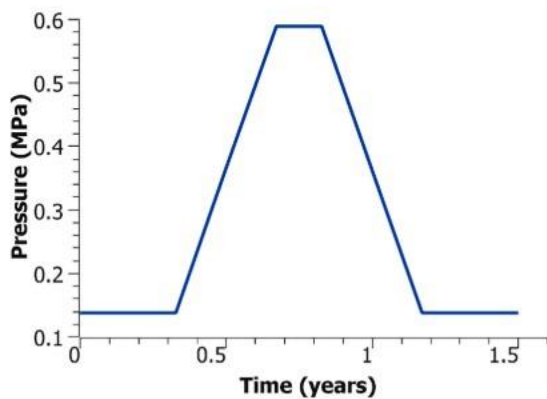

Fig. 4. Change of pressure with time representing the oscillating water level of the Bisri reservoir. 1 cycle is shown in this figure and is repeated throughout the entire simulation (60 years).

"induced" rather than "triggered" in this study.

The Koyna reservoir in India has caused one of the most destructive RIS events where an earthquake of magnitude 6.3 killed over 200 people and destroyed the properties of thousands in December of 1967 (Gupta, 1992).

Reservoir induced seismicity can be divided into two categories: initial and protracted seismicity. The initial seismicity is related to the coupled poroelastic response to the initial impoundment of the reservoir as well as water level changes and an increase in water level beyond any level reached thus far (Gupta and Combs, 1976; Talwani, 1997). This response can be instantaneous whereby changes in the normal and shear stresses are caused by the elastic response of the subsurface due to the loading or unloading. In addition, if the excess pressure caused by loading cannot be drained, there will be a direct increase in the pore pressure added to the instantaneous response until the pressure can be drained and dissipated. On the other hand, this response can be delayed owing to the pore pressure diffusion that increases the pressure at deeper levels. The largest seismic event in this case is recorded mainly after the complete impoundment of the reservoir (Talwani, 1997). The strength changes caused by the coupled poroelastic response can stop over months to few years to pre-impoundment levels, which is revealed by a decay in seismicity (Gómez and Talwani, 2010; Talwani, 1997; Talwani and Acree, 1984).

Several cases have shown a continued seismic activity observed decades after the initial seismicity, as in lake Mead, USA and the Koyna reservoir, India (Talwani, 1997). This seismicity is known as protracted seismicity and it depends on the geometry of the fault with respect to the reservoir, the period of water-level changes, and the hydromechanical properties of the subsurface. This kind of seismicity is likely to occur where the change in water-level is close to the minimum water level or a large fraction of it (Talwani, 1997).

One of the most important factors to consider in RIS is the presence of faults, their nature, and their location with respect to the oscillating reservoir load. 79% of RIS cases were found to be in normal or strike-slip faulting tectonic environments (Qiu and Fenton, 2015). A reservoir existing on the footwall of a reverse or normal fault, or over one block of a strike-slip fault would generally have a stabilizing effect, while a reservoir existing on the hanging wall of a reverse or normal fault, or directly over a vertical strike-slip fault, which is similar to the case of the Bisri reservoir that is located over a vertical dip-slip fault, would have a destabilizing effect (Roeloffs, 1988; Talwani, 1997). From here, the need to assess the risk for induced seismicity caused by the Bisri dam is necessary.

3.2. Poroelastic model and governing eq

3.2.1. Coulomb stress changes

In general, the failure criterion for rupture initiation is expressed by the change in Coulomb Failure Stress (CFS):

$$\Delta CFS = \Delta\tau + f(\Delta\sigma_n + \Delta p) \tag{1}$$

where f is the coefficient of friction, $\Delta\tau$ is the change in the shear stress, $\Delta\sigma_n$ is the total change in the applied normal stress (positive for tensile stresses), and Δp is the change in pore pressure.

Faults in the subsurface are commonly critically stressed, thus any alteration in the pore pressure, normal stress, or shear stress can reactivate them, which is reflected by a positive ΔCFS indicating an increase in the risk for induced seismicity (Segall and Lu, 2015). In other words, any activity that causes an overall positive change in the CFS could induce fault slip leading to an earthquake (Fig. 5).

3.2.2. Coupled poroelastic model

The coupled poroelastic model describes the response of a saturated porous elastic medium to changes in stresses and pore pressure. This model states that any variation in the pore pressure can alter the poroelastic stresses of the medium, which is referred to as fluid-to-solid coupling, and vice versa, the solid-to-fluid coupling where any change in stresses affects the pore pressure (Biot, 1941; Rice and Cleary, 1976; Segall and Lu, 2015; Wang, 2000).

The equilibrium equation under quasi-static condition and no additional body forces gives:

$$\nabla.\sigma = 0 \tag{2}$$

The constitutive equation for a fluid-saturated poroelastic medium, with the approximation of elastic isotropy, can be written as:

$$G\nabla^2 u + \frac{G}{1-2\nu}\nabla\epsilon - \alpha\nabla p = 0 \tag{3}$$

where G is the shear modulus, u is the velocity field, ν is Poisson's ratio, ϵ is the volumetric strain, α is Biot coefficient, and ∇p is the applied pressure gradient.

The pore fluid mass conservation equation can be written in terms of the fluid density ρ, the medium porosity $\varnothing$, and the fluid mass source Q_m as:

$$\frac{\partial}{\partial t}(\varnothing\rho) + \nabla.(\rho u) = Q_m \tag{4}$$

Darcy's Law describes the fluid flow in a porous elastic medium by the equation:
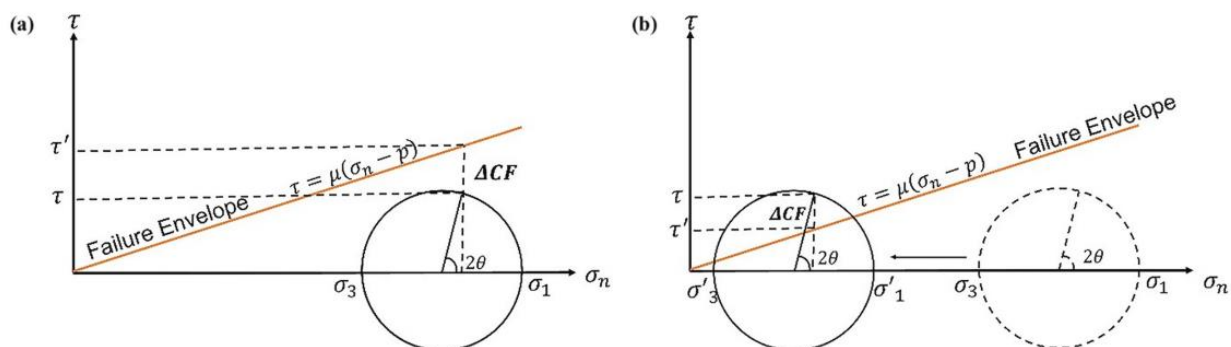
Fig. 5. The Coulomb failure stress (CFS) is represented by the difference in shear stress between the Mohr circle and the envelope of failure. σ_1 is the maximum principal stress, σ_3 is the minimum principal stress, θ is the angle between the direction of σ_1 and the normal to the fault surface, the internal cohesion of the rock is not included since it is negligible for preexisting faults (Steffen et al., 2015). (a) The CFS is negative indicating that the Mohr circle does not intersect the failure envelope, thus no risk of fault slip. (b) The Mohr circle shifted to the left due to a decrease in the effective normal stresses that can be caused by a pore pressure increase. Here the CFS is positive indicating that the Mohr circle intersects the failure envelope revealing a higher probability of failure.

$$u = -\frac{\kappa}{\mu}(\nabla p + \rho g \nabla z) \tag{5}$$

where u is Darcy's velocity, κ is the permeability of the medium, μ is the fluid viscosity, and ∇z is the difference in elevation.

In addition, the poroelastic storage coefficient S is given by:

$$\frac{\partial}{\partial t}(\varnothing\rho) = \rho S \frac{\partial \rho}{\partial t} \tag{6}$$

Then, the mass conservation equation can be re-written as:

$$\rho S \frac{\partial \rho}{\partial t} + \nabla.(\rho \boldsymbol{u}) = Q_m = -\rho \alpha \frac{\partial \epsilon}{\partial t} \tag{7}$$

The increase of the rate of change of the volumetric strain $\frac{\partial \epsilon}{\partial t}$ causes the fluid to sink since there is more space for the fluid to diffuse, hence the negative sign in the mass source term. The equations are solved in 2D, with a plane strain assumption, using COMSOL Multiphysics finite element method. We couple the flow in porous medium module, which solves Darcy's law (Eq. (5)) with the solid mechanics module, which solves the equilibrium equation under quasi-static conditions (Eq. (2)). The poroelastic coupling is done through introducing the Biot coefficient in the constitutive law (Eq. (3)) and the volumetric strain in the mass conservation equation (Eq. (7)). This approach has practical limitations such as: (1) hydraulic and mechanical properties are averaged along domains, (2) the model is not dynamic which means that the hydraulic and mechanical properties remain unchanged throughout the simulation. In reality, the occurrence of seismic events would alter these properties along with the stress state of the fault. Nonetheless, using a coupled poroelastic model is an effective approach to assess the potential for induced seismicity. After building the 2D model, a sensitivity analysis on the model mesh and the model size are performed. The analysis of the simulation results gives an initial assessment for the risk of induced seismicity associated with the dam project, which is necessary for the safety of the surrounding region.

3.3. Initial and boundary conditions

Initially, the displacement vector is assumed null, and the pore pressure is at hydrostatic conditions. For the solid mechanics equations, a roller boundary condition is applied to the left and right sides of the domain prohibiting deformation normal to the boundary. A fixed constraint condition is assigned to the bottom boundary, while a free condition is set to the top boundary making it free to move in all directions (traction-free) (Fig. 6b) (Fan et al., 2016; Segall and Lu, 2015). For the fluid flow equations, a no-flow boundary condition (the velocity component normal to the boundary is zero) is assigned to the bottom of the model. The width of the domain was chosen large enough so that
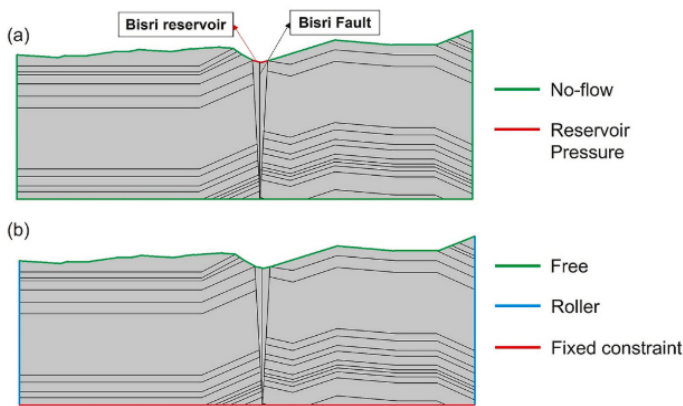

Fig. 6. (a) Fluid flow boundary conditions; no-flow ($-\boldsymbol{n}. \rho\boldsymbol{u} = 0$) reservoir pressur(as per Fig. 4). (b) Solid mechanics boundary conditions; roller ($\boldsymbol{n}. \boldsymbol{u} = 0$), fixed constraint ($\boldsymbol{u} = 0$), where $\boldsymbol{n}$ is the vector normal to the boundary.

there is no pressure build-up at the side boundaries that would affect the pressure at the Bisri Fault. Then, a no-flow boundary condition is assigned to the left and right sides of the domain. As for the upper boundary, where the reservoir is located, a pressure boundary of oscillating values reflecting the minimum and maximum water levels with a 6-month lag is assigned (Fig. 4). Outside of the reservoir location, a no-flow boundary condition is applied (Fig. 6a).

4. Results and discussion

In this section, we discuss the effect of the location of the planned Bisri reservoir on the stability of the faults in the region. In addition, a comparison is made with the effect of the location of the Qaraoun reservoir, which is located behind an existing dam, on the Yammouneh Fault. The comparison is made to answer the argument raised by the Bisri project planners that the Qaraoun reservoir has not witnessed induced seismic activity since its construction in 1959 despite its proximity to a major active fault. We will highlight the difference between the two cases and why the Qaraoun dam does not create a major risk for induced seismicity.

4.1. Bisri reservoir

Fractures in fault damage zones represent the dominant flow pathways in rocks, allowing the pressure to diffuse to deeper layers (Yehya et al., 2018), and they cause the rock mass to become less stable (Witherspoon and Gale, 1977). Fig. 7 shows the diffusion of the pore pressure, caused by the oscillating pressure from the supposed Bisri reservoir, and due to the presence of the damage zone, which causes an increase in pressure along the Bisri Fault. The pressure remains high in the shallower layers, even after pressure diffuses to deeper layers, due to the continuous pressure load of the oscillating water level of the reservoir.

In Fig. 8a, we notice the instantaneous increase in pore pressure at the shallow layers due to the initial impoundment. As the maximum water level is reached after 0.75 years, the pore pressure increases greatly at shallow levels. After 1.25 years, the water level decreases to its minimum, but the pore pressure keeps increasing. At the shallow levels, this increase is due to the undrained effect where the additional pore pressure caused by the reservoir still needs more time to diffuse. Whereby at the deep levels, this increase is due to the delayed effect of pore pressure diffusion from the previous water level. In addition, at a depth of -4.2 km (deep layers), there is a noticeable increase in the pore pressure, because of the initial undrained effect since at this level the porosity and permeability of the rocks become very low. Diffusion is relatively a slow process, hence a pressure perturbation on the surface needs a specific time to create a response at different levels. The time scales are governed by the hydraulic and poroelastic properties of the geologic formations. After 1.75 years of impoundment, at -4.2 km, we notice a decrease in pore pressure with time whereby it reaches values below hydrostatic (negative pressure). This decrease is due to the drained effect where the diffusion of pore pressure outward is greater than the additional pore pressure coming from the reservoir to this depth. Fig. 8b shows the duration between 10 and 30 years after initial impoundment, and indicates that after 10 years, the pressure at the surface does not vary because the additional pore pressure has dissipated. Comparing the three curves we notice that the increase in pore pressure with time is greater in the deeper layers than that in the shallow layers. This is due to the delayed response where the pressure diffuses and builds up at the deeper levels over time near the low permeability basement. Fig. 8c shows the duration between 40 and 60years after initial impoundment. The pressure increases, however, at a slower rate in the shallow layers and at the same rate in the deeper layers due to pore pressure diffusion. We observe a smaller variation of pressure between -3.5 and -4 km for all curves because the evaporite layer has very low porosity and permeability. In summary, the pore pressure tends
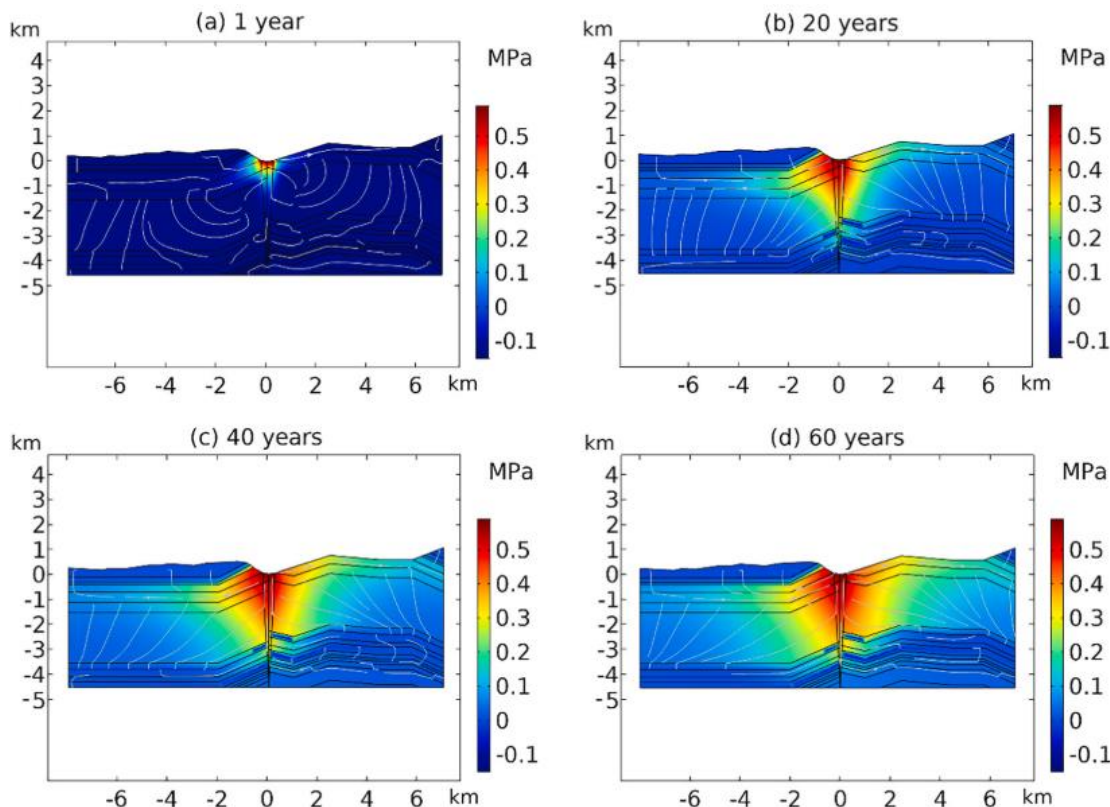
Fig. 7. The change in pore pressure (relative to the initial hydrostatic condition) along the 2D section shown in Fig. 3, after (a) 1 year, (b) 20 years, (c) 40 years and (d) 60 years from impoundment.
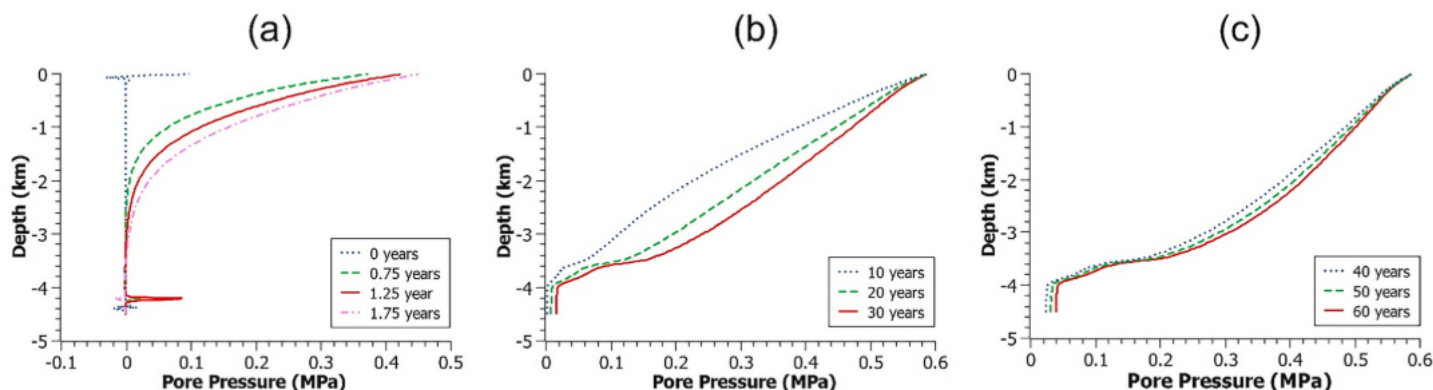

Fig. 8. (a) Variation of the pore pressure with depth at the start of the impoundment (blue curve), 0.75 years after impoundment when the maximum water level is reached (green curve), 1.25 years after impoundment when the water level has reached the minimum (red curve), and 1.75 years after impoundment where the water level is maximum (pink curve). (b) Variation of the pore pressure with depth after 10 years (blue curve), 20 years (green curve), and 30 years (red curve) from impoundment where the water level is average. (c) Variation of the pore pressure with depth after 40 years (blue curve), 50 years (green curve), and 60 years (red curve) from impoundment where the water level is average. (For interpretation of the references to colour in this figure legend, the reader is referred to the web version of this article.)

to have a destabilizing effect on preexisting faults since it decreases the effective normal stress facilitating failure (Fig. 5). This implies that the reservoir has an increasingly and continuously destabilizing effect on the Bisri Fault.

Fig. 9a shows that the normal stresses are positive indicating tensile stresses that have a destabilizing effect on faults, since it places faults under an extensional load. The stresses increase but at a slower rate with time (Fig. 9b). After 30 years, the stresses start to stabilize with little increase (Fig. 9c). The horizontal fluctuations in the curves are representatives of the different layers with different mechanical and hydraulic properties.

Both the pore pressure and the positive normal stresses have a

destabilizing effect on the fault, which is evident in the positive values of the CFS that exceed 0.1 MPa. It is noted from the study on the anthropogenic effect on induced seismicity by Mulargia and Bizzarri (2014) that an increase of 0.1 MPa in the overall stresses can lead to failure in critically stressed faults. The value of 0.1 MPa is considered a conservative threshold above which all faults that are at the vicinity of anthropogenic activity are assumed to fail (Mulargia and Bizzarri, 2014). The CFS values increase with time because of the combined effect of the pore pressure and tensile normal stresses (Fig. 10). As such, the CFS curves follow the trend of the normal stress curves but with a higher value due to the additional effect of the pore pressure. For example, after 40 years (Fig. 10c) the CFS values stabilize at the shallow layers owing to
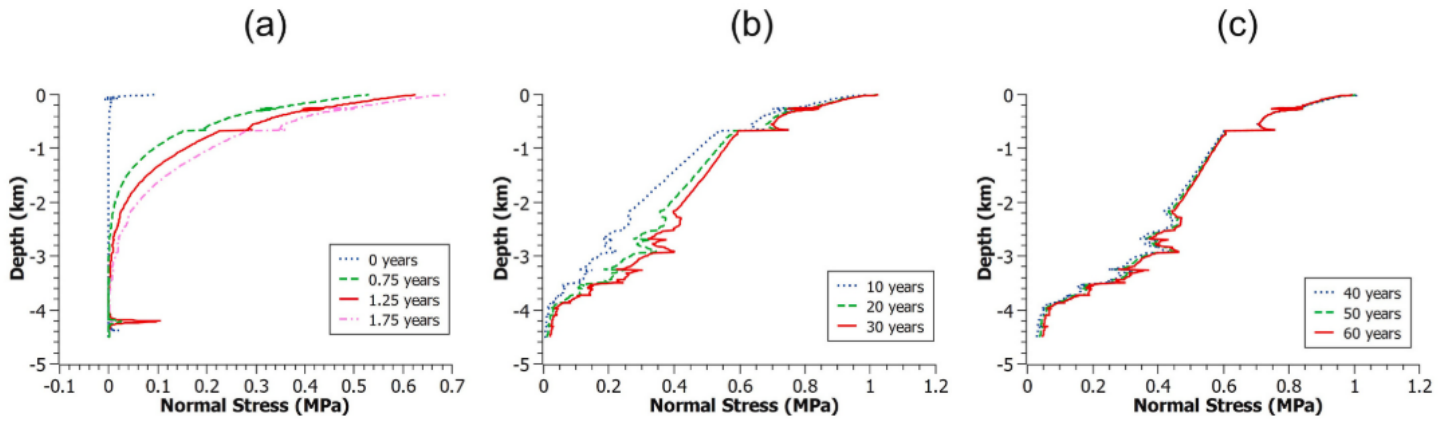
Fig. 9. (a) Variation of the normal stress with depth after the start of the reservoir impoundment (blue curve), 0.75 years after impoundment (green curve), 1.25 years after impoundment (red curve) and 1.75 years (pink curve) after impoundment. (b) Variation of the normal stress with depth after 10 years (blue curve), 20 years (green curve), and 30 years (red curve) from impoundment. (c) Variation of the normal stress with depth after 40 years (blue curve), 50 years (green curve), and 60 years (red curve) from impoundment. (For interpretation of the references to colour in this figure legend, the reader is referred to the web version of this article.)
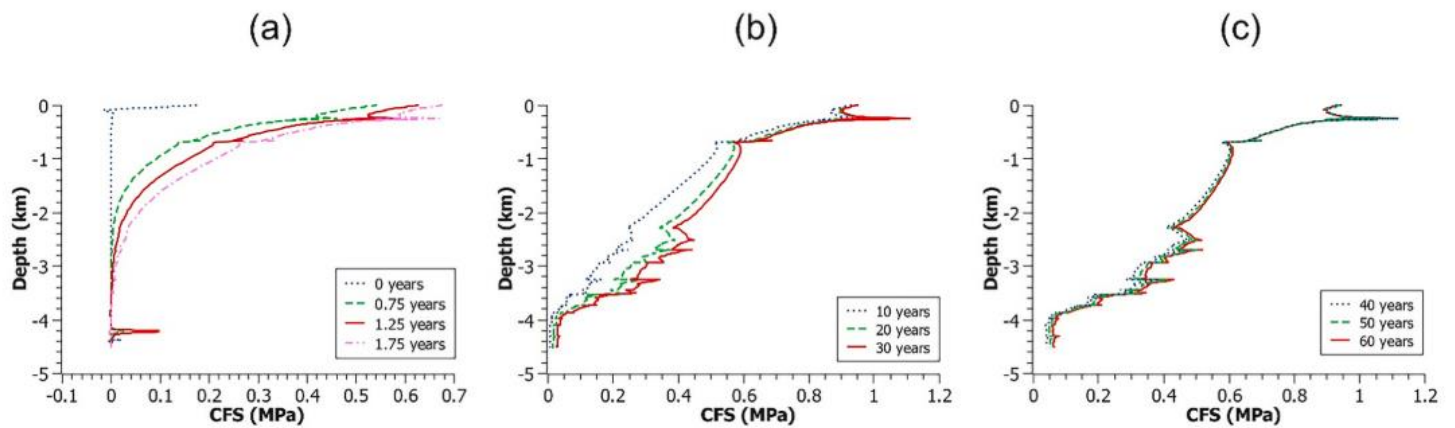
Fig. 10. (a) Variation of the CFS with depth after the start of the reservoir impoundment (blue curve), 0.75 years after impoundment (green curve), 1.25 years after impoundment (red curve) and 1.75 years (pink curve) after impoundment. (b) Variation of the CFS with depth after 10 years (blue curve), 20 years (green curve), and 30 years (red curve) from impoundment. (c) Variation of the CFS with depth after 40 years (blue curve), 50 years (green curve), and 60 years (red curve) from impoundment. (For interpretation of the references to colour in this figure legend, the reader is referred to the web version of this article.)

the limited increase in the normal stresses but increase with depth because of the pore pressure diffusion. This relation is better seen in Fig. 11 that shows the variation of the CFS, pore pressure, and normal stress with time in parallel at 3 different depths. The CFS values keep increasing for decades indicating protracted seismicity. To further

investigate the effect of the overall Coulomb stresses, we evaluate the change in the seismicity rate in Section 4.3.

Note that a 2D model was considered for this study, hence the 3-dimensional extent of the reservoir, fault zone and formations are not considered. It is expected that the trend of variation of the CFS remains
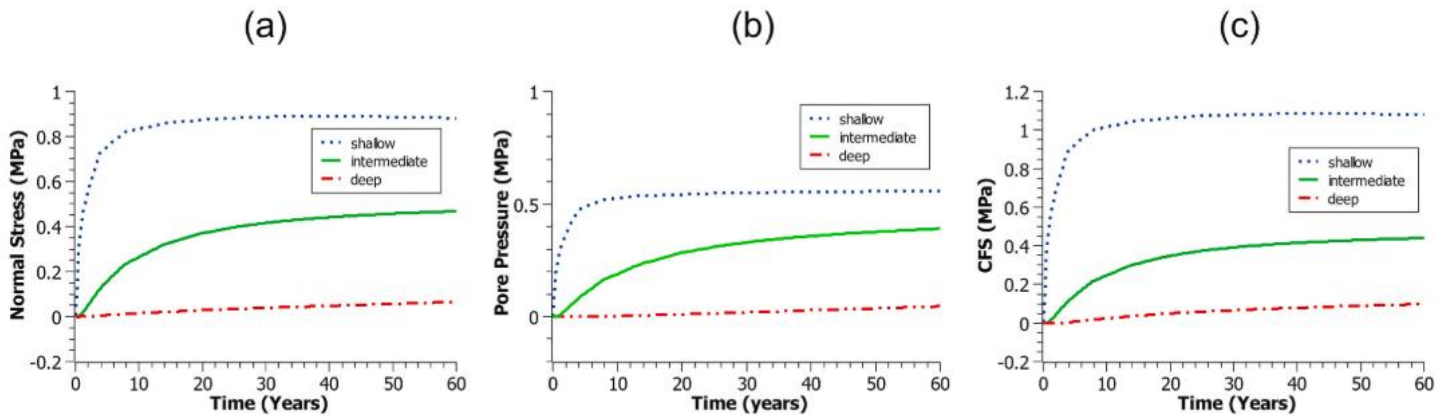

Fig. 11. Variation with time of (a) the normal stress, (b) the pore pressure, and (c) the CFS, at shallow (−0.3 km), deep (−4.1 km), and intermediate (−2.2 km) depths. The negative sign indicates depth below the surface.

the same over time for a 3D model, however, the CFS values will change due to the diffusion of pore pressure along the fault length and not only to deeper levels. The 2D assumption is valid for locations that are chosen away from the intersection between the Bisri Fault with the Roum Fault. In locations near the intersection, a 3D model is deemed necessary to investigate the induced seismicity on the Roum Fault as result of an increase in pore pressure caused by the fluid diffusion through the intersection between the two faults. Furthermore, the size of the Roum Fault is larger than that of the Bisri Fault, which affects the expected earthquake magnitude if the fault is activated.

4.2. Qaraoun reservoir: A case for comparison

The Qaraoun dam was built in 1959 in the southwest of the Beqa'a Valley, Lebanon, at an elevation of about 800 masl. The maximum water level of the Qaraoun Lake is at 858 masl with a maximum storage of 0.222 km^3, and the minimum water level is at 838 masl with a minimum storage of 0.053 km^3 (The Litani River Authority, 2021). The dam has a length of 1090 m, a width of 162 m, and a height of 60 m (The Litani River Authority, 2021). The exposed geologic formations in the area display a great offset due to the Yammouneh Fault that is located at approximately 2.4 km west of the Qaraoun Lake (Fig. 12). To the West of the fault, the karstic limestones of the Kesrouane Formation are exposed,

and adjacent to it to the East of the fault, the Mdeirej Formation is mainly exposed. These rocks are found to be extremely fractured, jointed, and friable, indicating a damage zone that is a few kilometers wide (Fig. 13). All the parameters used for this simulation are the same for the Bisri dam simulation above since the same formations are present.

As shown in Fig. 14a, the pore pressure increases with time; however, it has very low values (less than 0.04 MPa) compared to the Bisri reservoir case. The normal stresses are negative and decreasing further with time (Fig. 14b) indicating compressional stresses, which have a stabilizing effect on faults. This shows that the probability of reservoir induced seismicity is low, which is also indicated by the negative CFS values along the fault (Fig. 14c). After 62 years from impoundment, which represents the present-day state of the reservoir, the CFS values are negative, indicating that to this day there is no risk of induced seismicity caused by the Qaraoun Lake on the Yammouneh Fault. The latter result was expected due to the location of the Qaraoun Lake with respect to the strike-slip Yammouneh Fault, as strike-slip faults are generally destabilized when the oscillating reservoir is located directly over the fault (Roeloffs, 1988; Talwani, 1997). However, the location of the Qaraoun reservoir on one side of the Yammouneh Fault would not generate high risk for induced seismicity.
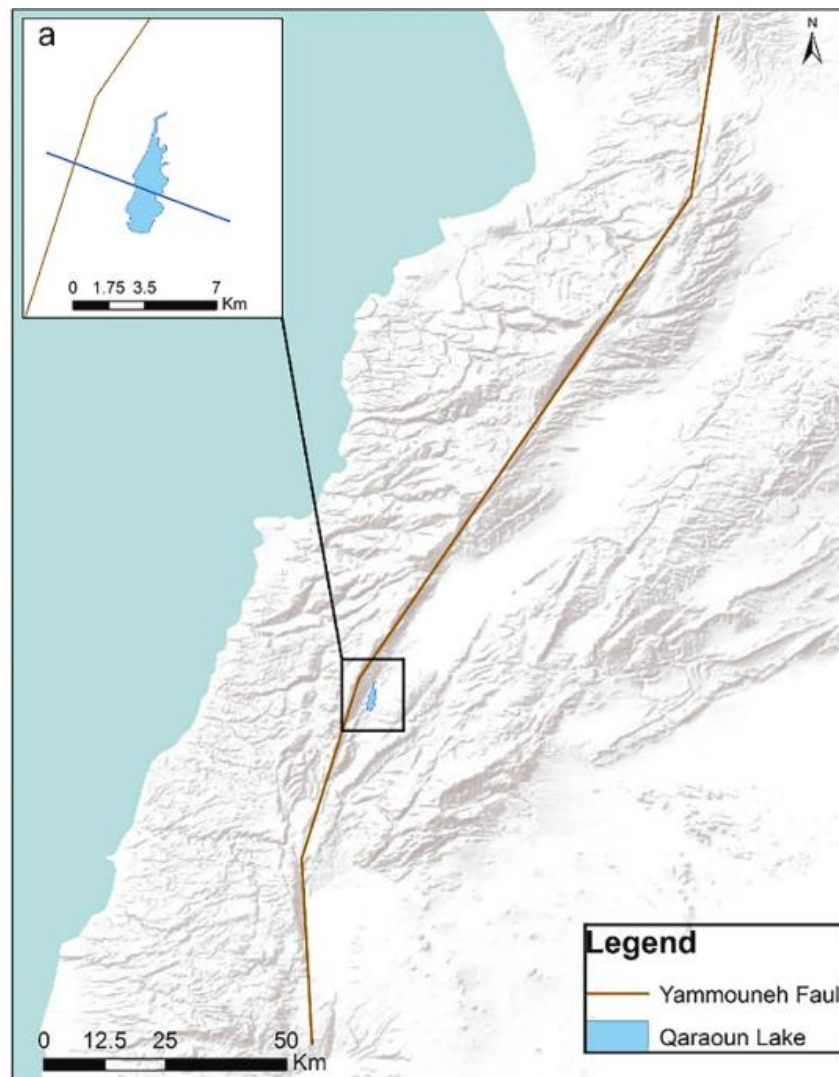

Fig. 12. Digital elevation model of Lebanon showing the Yammouneh Fault and the Qaraoun Lake. The blue line in (a) represents the location along which the 2D section in Fig. 13 was constructed. (For interpretation of the references to colour in this figure legend, the reader is referred to the web version of this article.)
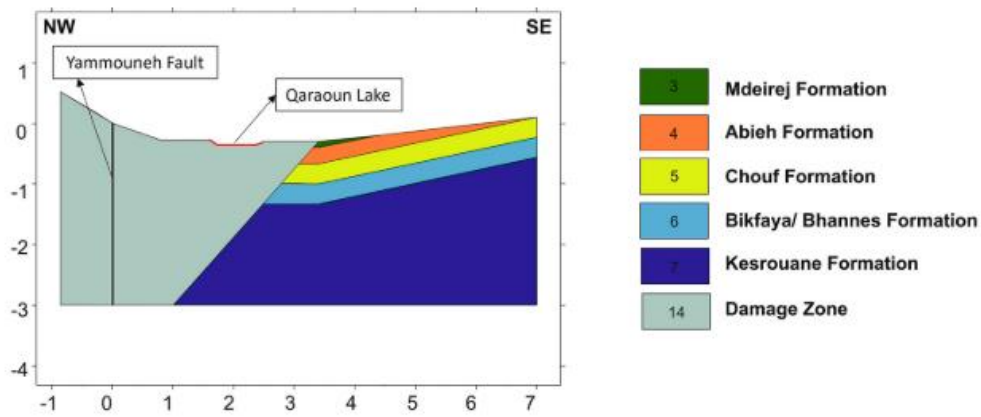
Fig. 13. 2D cross-section (taken along the blue line in Fig. 12a) showing the Qaraoun reservoir in red, the Yammouneh Fault, its damage zone, and the adjacent country rocks. (For interpretation of the references to colour in this figure legend, the reader is referred to the web version of this article.)
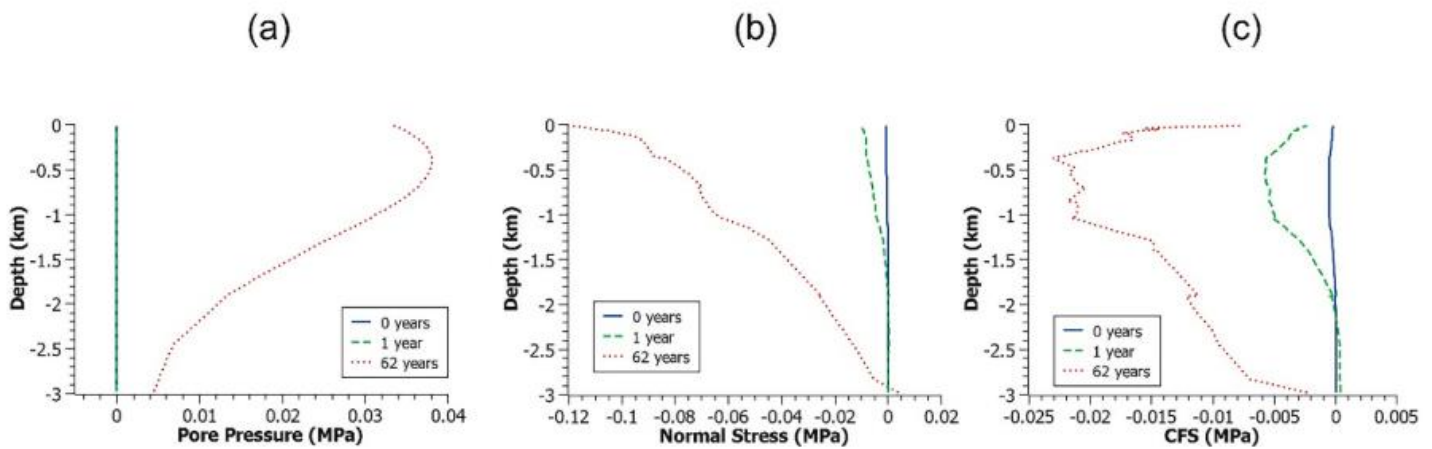

Fig. 14. Variation of the (a) pore pressure, (b) normal stress, and (c) CFS along the Yammouneh Fault at 0 (blue), 1 (green), and 62 years (red) after impoundment of the Qaraoun Lake. (For interpretation of the references to colour in this figure legend, the reader is referred to the web version of this article.)

4.3. Rate of seismicity

Besides calculating the change in the overall Coulomb Failure Stress along faults, predicting the rate of seismicity is another way to assess the potential for induced seismicity (Chang and Yoon, 2018; Segall and Lu, 2015; Wenzel, 2015). Dieterich (1994) developed a seismicity rate model relating the rate of earthquake nucleation to changes in coulomb stress and governed by rate and state friction. In the absence of any stress perturbation, the rate of seismicity will remain constant with time, otherwise under stress perturbation, an increase in this rate is expected. The rate of seismicity R can be calculated relative to a background stressing rate by:

$$\frac{dR}{dt} = \frac{R}{t_a} \left(\frac{\dot{\tau}}{\dot{\tau}_0} - R \right) \tag{8}$$

$\dot{\tau}_0$ being the background stressing rate, $\dot{\tau}$ the Coulomb stressing rate, and $t_a \equiv a \frac{\bar{\sigma}}{\dot{\tau}}$ the characteristic relaxation time, where a is the constitutive parameter in the rate state friction law quantifying the direct effect on slip.

In this study, $\bar{\sigma}$ is taken as 18.8 MPa (Markou and Papanastasiou, 2018), $\dot{\tau}$ as 0.001 MPa/year corresponding to a cumulative stress drop of 1 MPa every 1000 years, and a as 0.003 (Chang and Yoon, 2018; Segall and Lu, 2015). The resulting characteristic relaxation time t_a becomes 56.4 years which is comparable to the simulation duration for this study. However, we will discuss other values of the relaxation time to highlight the sensitivity of R to this parameter, and how that affects the risk assessment. The initial value of R is 1 and from Eq. (8), R returns to this value when time $t \gg t_a$. Fig. 15 shows the results for Eq. (8) for three points along the Bisri Fault, taken at three distinct depths: shallow, intermediate, and deep. At a shallow depth we find that the rate of induced seismicity rises rapidly to very high values, which is expected due to the initial effect of reservoir impoundment as well as the early undrained response, but then decreases gradually to steady state after around 20 years as the pore pressure diffuses to deeper levels. As we go deeper along the fault, the values of R decrease but take a longer time to restore back to steady state which is due to the delayed effect of pore pressure diffusion. We note that in very deep regions the rate of seismicity is close to the initial rate, which is set to 1, and this indicates that the potential of seismicity becomes higher in the shallower regions. Also, at times much greater than t_a, the rate of seismicity will decay to reach 1. The Eq. (8), thus, reaches a steady state solution and shows Omori-like decay when rapid change in stress occurs (Segall and Lu, 2015). However, its limitation is its inability to predict the earthquake magnitude, but it can give a good indication of the potential for induced seismicity for the Bisri Fault. Hence, the risk for induced seismicity for the shallow regions of the Bisri Fault is mainly in the first 10 years, however, the risk in the deeper regions near the stiff basement, which can lead to higher magnitude earthquakes, is after 10 years of its initial impoundment and continues to several decades later. When R is calculated for the Qaraoun case, no increase in the rate of seismicity is obtained because there is no stress perturbation rate above the background stress rate.

For a comparative analysis for the Bisri Fault response, we take different assumptions for the relaxation time (Fig. 16), and we find that a lower t_a (30 years) leads to a higher seismicity rate, but the seismicity
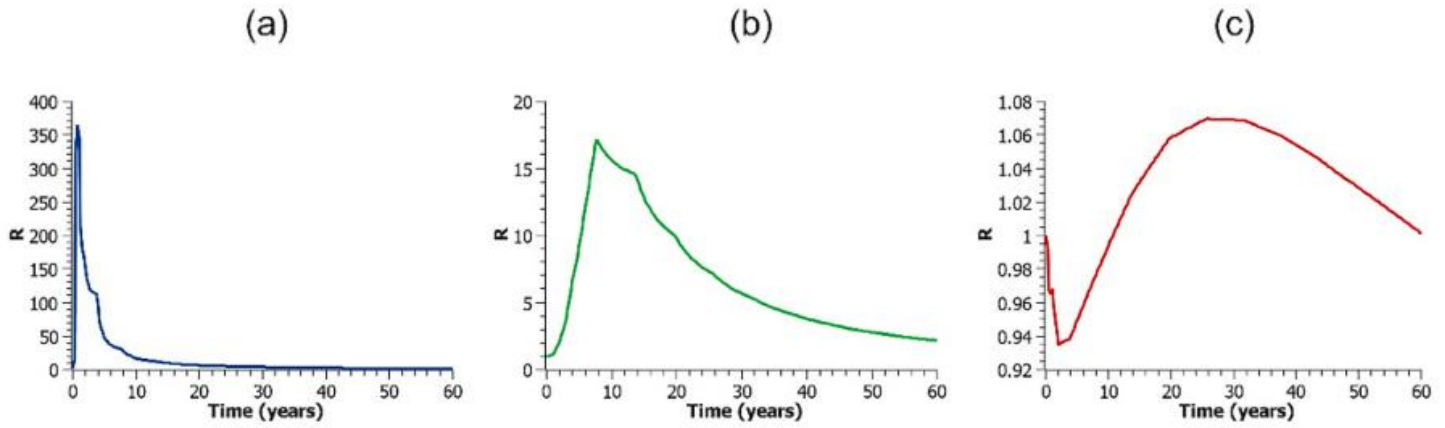
Fig. 15. Variation of the induced rate of seismicity with time at three different depths along the Bisri Fault: (a) at −0.3 km, (b) at −2.2 km and (c) at −4.1 km.
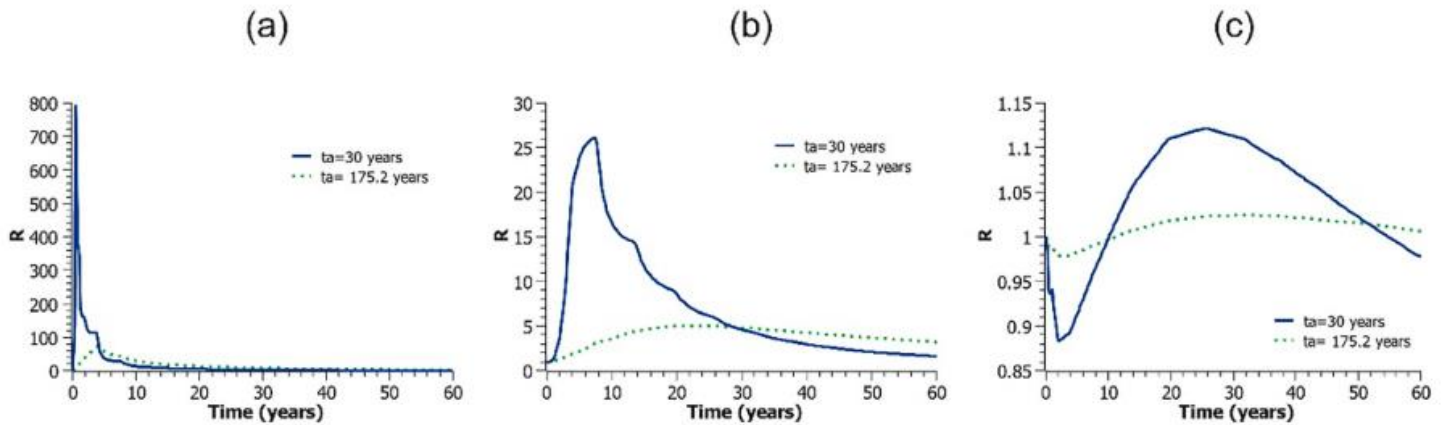

Fig. 16. Variation of the seismicity rate with time considering two characteristic times (ta = 30 and ta = 175.2 years) at depths (a) -0.3 km (shallow), (b) -2.2 km (intermediate) and (c) -4.1 km (deep) along the Bisri Fault.

restores back to steady state faster. On the other hand, if we consider a higher t_a (175 years), the seismicity rate takes much longer to restore back to steady state, but the values of R are lower. In all cases, building the Bisri dam disrupts the steady state of the existing Bisri Fault, and it would need many decades to be restored.

The dip angle of the Bisri Fault was taken as 90° in this study, but changes in fault orientation can influence the calculated CFS values. A geophysical electrical resistivity survey conducted in the Bisri valley (Bureau Technique pour le Developpement, Beirut, 1983) provided that the shallow part of the Bisri fault is probably vertical with little information about its deep part. However, from the geological point of view, and from studying the displacement and structures associated with this fault we can infer that the fault is vertical (Nemer, 2019). Despite that, we can evaluate the effect of orientation on the CFS values. Larger orientation in the dip (lower dip angle) will slow the pressure diffusion process to deeper regions and affect the CFS values, and hence it is more likely to decrease the rate of seismicity.

4.4. Implications for safety of humans and structures

The reactivation of the Bisri Fault has the potential to cause an earthquake since it is structurally connected to the Roum Fault (Nemer and Meghraoui, 2006; Nemer, 2019). The epicenters of three of the strongest seismic events that occurred in the twentieth century were located in the Roum Fault zone (Khair, 2001), one of which is the previously mentioned March 16th, 1956 event. A repeat of such an event would cause extensive damage to the regions of Chouf, Jezzine, Saida and parts of the Beqa'a as it has in the past where it killed 140 people, injured 500 others, destroyed 6000 houses, and damaged other

infrastructure including roads (Adra, 2014). The safety of the region surrounding the proposed Bisri dam should be the priority, and the risk for induced seismicity should be taken into consideration very seriously by the authorities.

5. Conclusions

The location of the planned Bisri reservoir directly over the dip-slip Bisri Fault makes the risk for reservoir induced seismicity very high. As such, the expected pore pressure and tensile normal stresses caused by the Bisri reservoir on the Bisri Fault will have a high probability of reactivating this fault, which is also indicated by the high and positive CFS values that largely exceed 0.1 MPa along the Bisri Fault and the increase in the seismicity rates. On the contrary, to this day, there is no risk of induced seismicity caused by the Qaraoun reservoir on the Yammouneh Fault, mainly because the Qaraoun Lake is located on one side of the fault, and the estimated CFS values are either negative or negligible. Therefore, the cases of the Bisri and Qaraoun dams in Lebanon are different, whereby it is evident that the Bisri dam would be in an extremely critical area where induced seismicity would be very likely, which puts thousands of people and structures at risk. More extensive studies should be made to assess the risk of the activation of the Bisri Fault on the interconnected Roum Fault, which hosted the epicenters of three of the strongest seismic events that occurred in the region during the twentieth century.

Declaration of Competing Interest

The authors declare that they have no known competing financial

interests or personal relationships that could have appeared to influence the work reported in this paper.

References

Adra, J., 2014. Lebanon ' s 1956 earthquake what if it Struck Today ? Mon. Mag. 1–2.

Ambraseys, N.N., Jackson, J.A., 1998. Faulting associated with historical and recent earthquakes in the Eastern Mediterranean region. Geophys. J. Int. 133, 390–406. https://doi.org/10.1046/j.1365-246X.1998.00508.x.

Ampuero, J.P., Mao, X., 2017. Upper Limit on damage Zone Thickness Controlled by Seismogenic Depth. In: Thomas, M., Mitchell, T., Bhat, H. (Eds.), Fault Zone Dynamic Processes: Evolution of Fault Properties during Seismic Rupture. John Wiley & Sons, Inc, pp. 243–253. https://doi.org/10.1002/9781119156895.ch13.

Biot, M.A., 1941. General theory of three-dimensional consolidation. J. Appl. Phys. 12, 155–164. https://doi.org/10.1063/1.1712886.

Bureau Technique pour le Developpement, Beirut, 1983. Prospection geophysique du site du barrage sur le Bisri. Office National du Litani, Liban (58p).

Cappa, F., Rutqvist, J., 2011. Modeling of coupled deformation and permeability evolution during fault reactivation induced by deep underground injection of CO_2. Int. J. Greenh. Gas Control 5, 336–346. https://doi.org/10.1016/j.ijggc.2010.08.005.

Chang, K.W., Yoon, H., 2018. 3-D Modeling of Induced Seismicity along Multiple Faults: Magnitude, Rate, and Location in a Poroelasticity System. J. Geophys. Res. Solid Earth 123, 9866–9883. https://doi.org/10.1029/2018JB016446.

Council for Development and Reconstruction, 2014. Greater Beirut Water Supply Augmentation Project Environmental and Social Impact Assessment, Dar al-handasha.

Dieterich, J., 1994. A constitutive law for rate of earthquake production and its application to earthquake clustering. J. Geophys. Res. 99, 2601–2618. https://doi.org/10.1029/93JB02581.

Fan, Z., Peter, E., Gale, J.F.W., 2016. Geomechanical analysis of fluid injection and seismic fault slip for the Mw4.8 Timpson, Texas, earthquake sequence. J. Geophys. Res. Solid Earth 3782–3803. https://doi.org/10.1002/2015JB012608.Received.

Fan, Z., Eichhubl, P., Newell, P., 2019. Basement Fault Reactivation by Fluid Injection into Sedimentary Reservoirs: Poroelastic Effects. J. Geophys. Res. Solid Earth 124, 7354–7369. https://doi.org/10.1029/2018JB017062.

Faulkner, D.R., Mitchell, T.M., Healy, D., Heap, M.J., 2006. Slip on "weak" faults by the rotation of regional stress in the fracture damage zone. Nature 444, 922–925. https://doi.org/10.1038/nature05353.

Gómez, I., Talwani, P., 2010. Reservoir-induced seismicity associated with the Itoiz Reservoir, Spain: a case study. Geophys. J. Int. 181, 343–356. https://doi.org/10.1111/j.1365-246X.2009.04462.x.

Gomez, F., Meghraoui, M., Darkal, A.N., Hijazi, F., Mouty, M., Suleiman, Y., Sbeinati, R., Darawcheh, R., Al-Ghazzi, R., Barazangi, M., 2003. Holocene faulting and earthquake recurrence along the Serghaya branch of the dead sea fault system in Syria and Lebanon. Geophys. J. Int. 153, 658–674. https://doi.org/10.1046/j.1365-246X.2003.01933.x.

Gudmundsson, A., 2004. Effects of Young's modulus on fault displacement. Comptes Rendus - Geosci. 336, 85–92. https://doi.org/10.1016/j.crte.2003.09.018.

Gupta, H.K., 1992. Worldwide distribution of reservoir-induced seismicity. In: The Present Status of Reservoir Induced Seismicity Investigations with Special Emphasis on Koyna Earthquakes. Elsevier Science, pp. 257–279. https://doi.org/10.1016/B978-0-444-88906-5.50008-9.

Gupta, H.K., Combs, J., 1976. Continued seismic activity at the Koyna reservoir site, India. Eng. Geol. 10, 307–313. https://doi.org/10.1016/0013-7952(76)90029-6.

Hancock, P.L., Atiya, M.S., 1979. Tectonic significance of mesofracture systems associated with the Lebanese segment of the Dead Sea transform fault. J. Struct. Geol. 1 https://doi.org/10.1016/0191-8141(79)90051-8.

Jackson, M., Hudec, M., 2017. Salt Tectonics. Cambridge University Press, Texas.

Khair, K., 2001. Geomorphology and seismicity of the Roum fault as one of the active branches of the Dead Sea fault system in Lebanon. J. Geophys. Res. Solid Earth 106, 4233–4245. https://doi.org/10.1029/2000jb900287.

Kuang, J., Qi, S., Hu, X., Liu, Z., 2022. Mechanism of reservoir - induced seismicity. Nat. Hazards 111, 2059–2076. https://doi.org/10.1007/s11069-021-05129-2.

Markou, N., Papanastasiou, P., 2018. Petroleum geomechanics modelling in the Eastern Mediterranean basin: Analysis and application of fault stress mechanics. Oil Gas Sci. Technol. 73 https://doi.org/10.2516/ogst/2018034.

Marlow, L., Kornpihl, K., Kendall, C.G.S.C., 2011. 2-D basin modeling study of petroleum systems in the Levantine Basin, Eastern Mediterranean. GeoArabia 16, 17–42.

McGarr, A.F., Simpson, D., Seeber, L., 2002. Case Histories of Induced and Triggered Seismicity, in: Case Histories of Induced and Triggered Seismicity. Elsevier, pp. 647–661.

Mitchell, T.M., Faulkner, D.R., 2009. The nature and origin of off-fault damage surrounding strike-slip fault zones with a wide range of displacements: a field study from the Atacama fault system, northern Chile. J. Struct. Geol. 31, 802–816. https://doi.org/10.1016/j.jsg.2009.05.002.

Mulargia, F., Bizzarri, A., 2014. Anthropogenic triggering of large earthquakes. Sci. Rep. 4, 1–7. https://doi.org/10.1038/srep06100.

Nader, F.H., Inati, L., Ghalayini, R., Hawie, N., Daher, S.B., 2018. Key geological characteristics of the Saida-Tyr Platform along the eastern margin of the Levant Basin, offshore Lebanon: Implications for hydrocarbon exploration. Oil Gas Sci. Technol. 73 https://doi.org/10.2516/ogst/2018045.

Nemer, T.S., 2019. The Bisri dam project: a dam on the seismogenic Roum fault, Lebanon. Eng. Geol. 261, 105270 https://doi.org/10.1016/j.enggeo.2019.105270.

Nemer, T.S., 2021. The Beirut port explosion: a geoscience perspective. Seismol. Res. Lett. xx 1–6. https://doi.org/10.1785/0220210051.

Nemer, T., Meghraoui, M., 2006. Evidence of coseismic ruptures along the Roum fault (Lebanon): a possible source for the AD 1837 earthquake. J. Struct. Geol. 28, 1483–1495. https://doi.org/10.1016/j.jsg.2006.03.038.

Nemer, T., Gomez, F., Al Haddad, S., Tabet, C., 2008a. Coseismic growth of sedimentary basins along the Yammouneh strike-slip fault (Lebanon). Geophys. J. Int. 175, 1023–1039. https://doi.org/10.1111/j.1365-246X.2008.03889.x.

Nemer, T., Meghraoui, M., Khair, K., 2008b. The Rachaya-Serghaya fault system (Lebanon): Evidence of coseismic ruptures, and the AD 1759 earthquake sequence. J. Geophys. Res. 113, 1–12. https://doi.org/10.1029/2007JB005090.

Pavlin, G.B., Langston, C.A., 1983. An integrated study of reservoir-induced seismicity and Landsat imagery at Lake Kariba, Africa. Photogramm. Eng. Remote Sens. 49, 513–525.

Qiu, X., Fenton, C., 2015. Factors Controlling the Occurrence of Reservoir-Induced Seismicity. In: Lollino, G., Giordan, D., Thuro, K., Carranza-Torres, C., Wu, F., Marinos, P., Delgado, C. (Eds.), Engineering Geology for Society and Territory. Springer International Publishing, London, pp. 567–570.

Ramasamy, S.M., Gunasekaran, S., Rajagopal, N., Saravanavel, J., Kumanan, C.J., 2019. Flood 2018 and the status of reservoir-induced seismicity in Kerala. India. Nat. Hazards 99, 307–319. https://doi.org/10.1007/s11069-019-03741-x.

Rice, J.R., Cleary, M.P., 1976. Some basic stress diffusion solutions for fluid-saturated elastic porous media with compressible constituents. Rev. Geophys. 14, 227–241. https://doi.org/10.1029/RG014i002p00227.

Roeloffs, E.A., 1988. Fault stability changes induced beneath a reservoir with cyclic variations in water level. J. Geophys. Res. 93, 2107. https://doi.org/10.1029/jb093ib03p02107.

Salah, M.K., Alqudah, M., El-Aal, A.K.A., Barnes, C., 2018. Effects of porosity and composition on seismic wave velocities and elastic moduli of lower cretaceous rocks, Central Lebanon. Acta Geophys. 66, 867–894. https://doi.org/10.1007/s11600-018-0187-1.

Salah, M.K., Alqudah, M., David, C., 2020a. Petrophysical and acoustic assessment of carbonate rocks, Zahle area, Central Lebanon. Bull. Eng. Geol. Environ. 79, 5455–5475. https://doi.org/10.1007/s10064-020-01900-0.

Salah, M.K., Alqudah, M., David, C., 2020b. Acoustics and petrophysical investigations on upper cretaceous carbonate rocks from northern Lebanon. J. African Earth Sci. 172, 103955 https://doi.org/10.1016/j.jafrearsci.2020.103955.

Salah, M.K., Alqudah, M., Monzer, A.J., David, C., 2020c. Petrophysical and acoustic characteristics of Jurassic and cretaceous rocks from Central Lebanon. Carbonates Evaporites 35. https://doi.org/10.1007/s13146-019-00536-w.

Segall, P., Lu, S., 2015. Injection-induced seismicity: Poroelastic and earthquake nucleation effects. J. Geophys. Res. Solid Earth 120, 5082–5103. https://doi.org/10.1002/2015JB012060.

Stefanov, Y.P., Bakeev, R.A., 2015. Formation of flower structures in a geological layer at a strike-slip displacement in the basement. Phys. Solid Earth 51, 81–93. https://doi.org/10.1134/S1069351315040114.

Steffen, R., Steffen, H., Wu, P., Eaton, D.W., 2015. Stress and fault parameters affecting fault slip magnitude and activation time during a glacial cycle. Tectonics 34, 2359–2366. https://doi.org/10.1002/2015TC003992.

Talwani, P., 1997. On the Nature of Reservoir-induced Seismicity. Pure Appl. Geophys. 150, 473–492. https://doi.org/10.1007/978-3-0348-8814-1_8.

Talwani, P., Acree, S., 1984. Pore pressure diffusion and the mechanism of reservoir-induced seismicity. Pure Appl. Geophys. PAGEOPH 122, 947–965. https://doi.org/10.1007/BF00876395.

The Litani River Authority, 2021. The Qaraoun Lake & Dam [WWW Document]. URL. http://www.litani.gov.lb/en/?page_id=91.

The World Bank, 2021. Lebanon Water Supply Augmentation Project (Bisri Dam), pp. 1–10.

Tsung-ho, H., Hsueh-hai, L., Tu-hsin, H., Cheng-jung, Y., 1976. Strong-motion observation of water-induced earthquakes at Hsinfengkiang reservoir in China. Eng. Geol. 10, 315–330. https://doi.org/10.1016/0013-7952(76)90030-2.

Wang, H.F., 2000. Theory of Linear Poroelasticity with Applications to Geomechanics and Hydrogeology.

Wenzel, F., 2015. Induced Seismicity using Dieterich's Rate and State Theory and Comparison to the critical pressure Theory. Energy Procedia 76, 282–290. https://doi.org/10.1016/j.egypro.2015.07.863.

Witherspoon, P.A., Gale, J.E., 1977. Mechanical and hydraulic properties of rocks related to induced seismicity. Eng. Geol. 11, 23–55. https://doi.org/10.1016/0013-7952(77)90018-7.

Yang, Z., Yehya, A., Iwalewa, T.M., Rice, J.R., 2021. Effect of Permeability Evolution in Fault damage zones on Earthquake Recurrence. J. Geophys. Res. Solid Earth. https://doi.org/10.1029/2021jb021787.

Yehya, A., Rice, J.R., 2020. Influence of Fluid-Assisted Healing on Fault Permeability Structure. J. Geophys. Res. Solid Earth 125. https://doi.org/10.1029/2020JB020553.

Yehya, A., Yang, Z., Rice, J.R., 2018. Effect of Fault Architecture and Permeability Evolution on Response to Fluid Injection. J. Geophys. Res. Solid Earth 123, 9982–9997. https://doi.org/10.1029/2018JB016550.

REFERENCES

Adra, J., 2014. Lebanon ' s 1956 Earthquake What If It Struck Today ? Mon. Mag. 1–2.

Ampuero, J.P., Mao, X., 2017. Upper Limit on Damage Zone Thickness Controlled by Seismogenic Depth, in: Thomas, M., Mitchell, T., Bhat, H. (Eds.), Fault Zone Dynamic Processes: Evolution of Fault Properties During Seismic Rupture. John Wiley & Sons, Inc, pp. 243–253. https://doi.org/10.1002/9781119156895.ch13

Bao, X., Eaton, D.W., 2016. Fault activation by hydraulic fracturing in western Canada. https://doi.org/10.1126/science.aag2583

Barbour, A.J., Norbeck, J.H., Rubinstein, J.L., 2017. The effects of varying injection rates in osage county, Oklahoma, on the 2016 Mw 5.8 Pawnee Earthquake. Seismol. Res. Lett. 88, 1040–1053. https://doi.org/10.1785/0220170003

Basbous, J., Nemer, T.S., Yehya, A., Maalouf, E., 2022. Assessing the potential for reservoir induced seismicity from the Bisri dam project in Lebanon. Eng. Geol. 304, 1–13. https://doi.org/10.1016/j.enggeo.2022.106679

Bell, M.L.E.E., Nur, A., 1978. Strength Changes Due to Reservoir-Induced Pore Pressure and Stresses and Application to Lake Oroville. J. Geophys. Res. 83, 4469–4483.

Beydoun, Z.R., 1977. The Levantine countries: The geology of Syria and Lebanon (Maritime Regions), in: Nairn, A.E.M., Kanes, W.H., Stehli, F.G. (Eds.), The Ocean Basins and Margins. Springer, Boston, MA, pp. 319–353. https://doi.org/https://doi.org/10.1007/978-1-4684-3036-3_8

Bhattacharya, P., Viesca, R.C., 2019. Fluid-induced aseismic fault slip outpaces pore-fluid migration. sciencemag 364, 464–468.

Biot, M.A., 1941. General theory of three-dimensional consolidation. J. Appl. Phys. 12, 155–164. https://doi.org/10.1063/1.1712886

Bischoff, M., Cete, A., Fritschen, R., Meier, T., 2010. Coal Mining Induced Seismicity in the Ruhr Area , Germany. Pure Appl. Geophys. 167, 63–75. https://doi.org/10.1007/s00024-009-0001-8

Brudzinski, M.R., Kozłowska, M., 2019. Seismicity induced by hydraulic fracturing and wastewater disposal in the Appalachian Basin, USA: a review. Acta Geophys. 67, 351–364. https://doi.org/10.1007/s11600-019-00249-7

Cappa, F., Rutqvist, J., 2011. Modeling of coupled deformation and permeability evolution during fault reactivation induced by deep underground injection of CO2. Int. J. Greenh. Gas Control 5, 336–346. https://doi.org/10.1016/j.ijggc.2010.08.005

Chang, K.W., Yoon, H., 2018. 3-D Modeling of Induced Seismicity Along Multiple Faults: Magnitude, Rate, and Location in a Poroelasticity System. J. Geophys. Res. Solid Earth 123, 9866–9883. https://doi.org/10.1029/2018JB016446

Cough, D.I., Gough, W.I., 1970. Load-induced Earthquakes at Lake Kariba-11. J.Earth Syst. Sci. 21, 79–101.

Council for Development and Reconstruction, 2014. Greater Beirut Water Supply Augmentation Project Environmental and Social Impact Assessment, Dar al-handasha.

Cueto-felgueroso, L., 2020. Geomechanical Constraints on Hydro-Seismicity : Tidal

Forcing and Reservoir Operation 1–23. https://doi.org/10.3390/w12102724

Davies, R., Foulger, G., Bindley, A., Styles, P., 2013. Induced seismicity and hydraulic fracturing for the recovery of hydrocarbons. Mar. Pet. Geol. 45, 171–185. https://doi.org/10.1016/j.marpetgeo.2013.03.016

Deichmann, N., Giardini, D., 2009. Earthquakes Induced by the stimulation of an enhanced geothermal system below Basel (Switzerland). Seismol. Res. Lett. 80, 784–798. https://doi.org/10.1785/gssrl.80.5.784

Dieterich, J., 1994. A constitutive law for rate of earthquake production and its application to earthquake clustering. J. Geophys. Res. 99, 2601–2618. https://doi.org/10.1029/93JB02581

Doglioni, C., 2018. A classification of induced seismicity. Geosci. Front. 9, 1903–1909. https://doi.org/10.1016/j.gsf.2017.11.015

Dubertret, 1955. Carte géologique du Liban: République Libanaise. République Libanaise, Ministère des Trav. Publiques.

Emanov, A.F., Emanov, A.A., Fateev, A. V, Leskova, E. V, Shevkunova, E. V, Podkorytova, V.G., 2014. Mining-Induced Seismicity at Open Pit Mines in Kuzbass (Bachatsky Earthquake on June 18 , 2013) 50, 224–228. https://doi.org/10.1134/S1062739114020033

Fan, Z., Eichhubl, P., Newell, P., 2019. Basement Fault Reactivation by Fluid Injection Into Sedimentary Reservoirs: Poroelastic Effects. J. Geophys. Res. Solid Earth 124, 7354–7369. https://doi.org/10.1029/2018JB017062

Fan, Z., Peter, E., Gale, J.F.W., 2016. Geomechanical analysis of fluid injection and

seismic fault slip for the Mw4.8 Timpson, Texas, earthquake sequence. J. Geophys. Res. Solid Earth 3782–3803. https://doi.org/10.1002/2015JB012608.Received

Faulkner, D.R., Mitchell, T.M., Healy, D., Heap, M.J., 2006. Slip on "weak" faults by the rotation of regional stress in the fracture damage zone. Nature 444, 922–925. https://doi.org/10.1038/nature05353

Firoozabadi, A., Cheng, P., 2010. Prospects for Subsurface CO2 Sequestration. AIChE J. 56, 1398–1405. https://doi.org/10.1002/aic

Foulger, G.R., Wilson, M.P., Gluyas, J.G., Julian, B.R., Davies, R.J., 2018. Earth-Science Reviews Global review of human-induced earthquakes. Earth-Science Rev. 178, 438–514. https://doi.org/10.1016/j.earscirev.2017.07.008

Freund, R., Garfunkel, M., Zak, I., Goldberg, M., Weissbrod, T., Derin, B., 1970. A discussion on the structure and evolution of the Red Sea and the nature of the Red Sea, Gulf of Aden and Ethiopia rift junction - The shear along the Dead Sea rift. R. Soc. Publ. 12–14.

Ge, S., Liu, M., Lu, N., Godt, J.W., Luo, G., 2009. Did the Zipingpu Reservoir trigger the 2008 Wenchuan earthquake ? Geophys. Res. Lett. 36, 3–7. https://doi.org/10.1029/2009GL040349

Gedeon, M., 1999. Structural Analysis of Latitudinal Faults in the Mount Lebanon North of Beirut: Their Kinematics and Their Role in the Tectonic Evolution of Lebanon. American University of Beirut.

Gomez, F., Meghraoui, M., Darkal, A.N., Hijazi, F., Mouty, M., Suleiman, Y., Sbeinati,

R., Darawcheh, R., Al-Ghazzi, R., Barazangi, M., 2003. Holocene faulting and earthquake recurrence along the Serghaya branch of the dead sea fault system in Syria and Lebanon. Geophys. J. Int. 153, 658–674. https://doi.org/10.1046/j.1365-246X.2003.01933.x

Gong, F., Guo, T., Sun, W., Li, Z., Yang, B., Chen, Y., Qu, Z., 2020. Evaluation of geothermal energy extraction in Enhanced Geothermal System (EGS) with multiple fracturing horizontal wells (MFHW). Renew. Energy 151, 1339–1351. https://doi.org/10.1016/j.renene.2019.11.134

González, P.J., Tiampo, K.F., Palano, M., Cannavó, F., Fernández, J., 2012. The 2011 Lorca earthquake slip distribution controlled by groundwater crustal unloading. Nat. Geosci. 5, 821–825. https://doi.org/10.1038/ngeo1610

Gudmundsson, A., 2004. Effects of Young's modulus on fault displacement. Comptes Rendus - Geosci. 336, 85–92. https://doi.org/10.1016/j.crte.2003.09.018

Gupta, Harsh K., 2022. Koyna , India : A very prominent site of artificial water reservoir-triggered seismicity. J.Earth Syst. Sci. 131, 1–30. https://doi.org/10.1007/s12040-021-01780-2

Gupta, H.K., 2021. Artificial Water Reservoir - Triggered Seismicity (RTS): Most Prominent Anthropogenic Seismicity, Surveys in Geophysics. Springer Netherlands. https://doi.org/10.1007/s10712-021-09675-z

Gupta, H.K., 1992. Worldwide distribution of reservoir-induced seismicity, in: The Present Status of Reservoir Induced Seismicity Investigations with Special Emphasis on Koyna Earthquakes. Elsevier Science, pp. 257–279. https://doi.org/10.1016/B978-0-444-88906-5.50008-9

Gupta, H.K., Combs, J., 1976. Continued seismic activity at the Koyna reservoir site, India. Eng. Geol. 10, 307–313. https://doi.org/10.1016/0013-7952(76)90029-6

Haidar, H., Barada, A., Halwani, J., Wehbi, I., Zahrdeen, L., 2022. Sustainable design consideration in the construction of earth dams in Lebanon. Geomech. Geoengin. 17, 358–371. https://doi.org/10.1080/17486025.2020.1755462

Hancock, P.L., Atiya, M.S., 1979. Tectonic significance of mesofracture systems associated with the Lebanese segment of the Dead Sea transform fault. J. Struct. Geol. 1. https://doi.org/10.1016/0191-8141(79)90051-8

Hanks, T.C., Kanamori, H., 1979. A Moment Magnitude Scale. J. Geophys. Res. 84, 2348–2350.

Hasegawa, S., Gendzwill, N.J., 1989. Induced Seismicity in Mines in Canada-An Overview 129.

Hincks, T., Aspinall, W., Cooke, R., Gernon, T., 2018. Oklahoma's induced seismicity strongly linked to wastewater injection depth. Science (80-.). 359, 1251–1255.

HiQuake, 2022. The Human-Induced Earthquake Database [WWW Document]. URL www.inducedearthquakes.org (accessed 6.11.22).

Hitzman, M., 2013. Induced Seismicity Potential of Energy Technologies.

Jackson, M., Hudec, M., 2017. Salt Tectonics. Cambridge University Press, Texas.

Keranen, K.M., Weingarten, M., 2018. Induced Seismicity. Annu. Rev. Earth Planet. Scieces 149–174.

Khair, K., 2001. Geomorphology and seismicity of the Roum fault as one of the active

branches of the Dead Sea fault system in Lebanon. J. Geophys. Res. Solid Earth 106, 4233–4245. https://doi.org/10.1029/2000jb900287

Khair, K., Khawlie, M., Haddad, F., Barazangi, M., Seber, D., Chaimov, T., 1993. Bouguer gravity and crustal structure of the Dead Sea transform fault and adjacent mountain belts in Lebanon. Geology 21, 739–742. https://doi.org/10.1130/0091-7613(1993)021<0739:BGACSO>2.3.CO;2

Klose, C.., 2007. NASA / ADS Coastal land loss and gain as potential earthquake trigger mechanism in SCRs, in: Proceedings of the Fall Meeting of the American Geophysical Union Abstract T51D-0759. San Francisco.

Kuang, J., Qi, S., Hu, X., Liu, Z., 2022. Mechanism of reservoir - induced seismicity in the Xinfengjiang reservoir area, Guangdong, China. Nat. Hazards 111, 2059–2076. https://doi.org/10.1007/s11069-021-05129-2

Langenbruch, C., Zoback, M.D., 2017. Response to Comment on "How will induced seismicity in Oklahoma respond to decreased saltwater injection rates?" Sci. Adv. 3, 1–10. https://doi.org/10.1126/sciadv.aao2277

Li, T., Cai, M.F., Cai, M., 2007. A review of mining-induced seismicity in China. Int. J. Rock Mech. Min. Sci. 44, 1149–1171. https://doi.org/10.1016/j.ijrmms.2007.06.002

Lin, C., 2005. Seismicity increase after the construction of the world ' s tallest building : An active blind fault beneath the Taipei 101 32, 1–4. https://doi.org/10.1029/2005GL024223

Liu, M., Stein, S., Wang, H., 2011. 2000 years of migrating earthquakes in North

China : How earthquakes in midcontinents differ from those at plate boundaries. Lithosphere 3, 128–132. https://doi.org/10.1130/L129.1

Majer, E.L., Baria, R., Stark, M., Oates, S., Bommer, J., Smith, B., Asanuma, H., 2007. Induced seismicity associated with Enhanced Geothermal Systems. Geothermics 36, 185–222. https://doi.org/10.1016/j.geothermics.2007.03.003

Manchao, H., Ribeiro, S., Tiago, M., Gualong, Z., 2015. Rockburst laboratory tests database — Application of data mining techniques. Eng. Geol. 185, 116–130.

Markou, N., Papanastasiou, P., 2018. Petroleum geomechanics modelling in the Eastern Mediterranean basin: Analysis and application of fault stress mechanics. Oil Gas Sci. Technol. 73. https://doi.org/10.2516/ogst/2018034

Marlow, L., Kornpihl, K., Kendall, C.G.S.C., 2011. 2-D basin modeling study of petroleum systems in the Levantine Basin, Eastern Mediterranean. GeoArabia 16, 17–42.

Mcgarr, A., 1976. Seismic Moments and Volume Changes. J. Geophys. Res. 81, 1487–1494.

McGarr, A.F., Simpson, D., Seeber, L., 2002. Case Histories of Induced and Triggered Seismicity, in: Case Histories of Induced and Triggered Seismicity. Elsevier, pp. 647–661.

McKeown, F.A., Dickey, D.D., 1969. Fault Displacements And Motion Related To Nuclear Explosions. Bull. Sebmolog~cal Soc. Am. 59, 2253–2269.

Milev, A.M., Spottiswoode, S.M., 2002. Effect of the rock properties on mining-induced seismicity around the Ventersdorp Contact Reef, Witwatersrand Basin,

South Africa. Pure Appl. Geophys. 159, 165–177. https://doi.org/10.1007/978-3-0348-8179-1_8

Mitchell, T.M., Faulkner, D.R., 2009. The nature and origin of off-fault damage surrounding strike-slip fault zones with a wide range of displacements: A field study from the Atacama fault system, northern Chile. J. Struct. Geol. 31, 802–816. https://doi.org/10.1016/j.jsg.2009.05.002

Mulargia, F., Bizzarri, A., 2014. Anthropogenic triggering of large earthquakes. Sci. Rep. 4, 1–7. https://doi.org/10.1038/srep06100

Murray, K.E., Holland, A.A., 2014. Subsurface fluid injection in oil and gas reservoirs and wastewater disposal zones of the midcontinent. AAPG 2014 Annu. Conv. Exhib. 80377, 1–8.

Nader, F.H., Inati, L., Ghalayini, R., Hawie, N., Daher, S.B., 2018. Key geological characteristics of the Saida-Tyr Platform along the eastern margin of the Levant Basin, offshore Lebanon: Implications for hydrocarbon exploration. Oil Gas Sci. Technol. 73. https://doi.org/10.2516/ogst/2018045

Nemer, T., Gomez, F., Al Haddad, S., Tabet, C., 2008a. Coseismic growth of sedimentary basins along the Yammouneh strike-slip fault (Lebanon). Geophys. J. Int. 175, 1023–1039. https://doi.org/10.1111/j.1365-246X.2008.03889.x

Nemer, T., Meghraoui, M., 2006. Evidence of coseismic ruptures along the Roum fault (Lebanon): a possible source for the AD 1837 earthquake. J. Struct. Geol. 28, 1483–1495. https://doi.org/10.1016/j.jsg.2006.03.038

Nemer, T., Meghraoui, M., Khair, K., 2008b. The Rachaya-Serghaya fault system (

Lebanon): Evidence of coseismic ruptures , and the AD 1759 earthquake sequence. J. Geophys. Res. 113, 1–12. https://doi.org/10.1029/2007JB005090

Nemer, T.S., 2019. The Bisri dam project: A dam on the seismogenic Roum fault, Lebanon. Eng. Geol. 261, 105270. https://doi.org/10.1016/j.enggeo.2019.105270

Nemer, T.S., Meghraoui, M., 2020. A non-active fault within an active restraining bend : The case of the Hasbaya fault , Lebanon. J. Struct. Geol. 136, 104060. https://doi.org/10.1016/j.jsg.2020.104060

Pavlin, G.B., Langston, C.A., 1983. An integrated study of reservoir-induced seismicity and Landsat imagery at Lake Kariba, Africa. Photogramm. Eng. Remote Sens. 49, 513–525.

Peduzzi, P., Harding, R., 2013. Gas fracking: can we safely squeeze the rocks? Environ. Dev. 6, 86–99. https://doi.org/10.1016/j.envdev.2012.12.001

Pennington, B.Y.W.D., Davis, S.D., Carlson, S.M., Dupree, J., Ewing, T.E., 1986. The Evolution Of Seismic Barriers And Asperities Caused By The Depressuring Of Fault Planes In Oil And Gas Fields Of South Texas. Bull. Seismol. Soc. Americ 76, 939–948.

Ramasamy, S.M., Gunasekaran, S., Rajagopal, N., Saravanavel, J., Kumanan, C.J., 2019. Flood 2018 and the status of reservoir-induced seismicity in Kerala , India. Nat. Hazards 99, 307–319. https://doi.org/10.1007/s11069-019-03741-x

Rice, J.R., Cleary, M.P., 1976. Some basic stress diffusion solutions for fluid-saturated elastic porous media with compressible constituents. Rev. Geophys. 14, 227–241. https://doi.org/10.1029/RG014i002p00227

Roeloffs, E.A., 1988. Fault stability changes induced beneath a reservoir with cyclic

    variations in water level. J. Geophys. Res. 93, 2107.

    https://doi.org/10.1029/jb093ib03p02107

Salah, M.K., Alqudah, M., David, C., 2020a. Acoustics and petrophysical investigations

    on upper cretaceous carbonate rocks from northern Lebanon. J. African Earth Sci.

    172, 103955. https://doi.org/10.1016/j.jafrearsci.2020.103955

Salah, M.K., Alqudah, M., David, C., 2020b. Petrophysical and acoustic assessment of

    carbonate rocks, Zahle area, central Lebanon. Bull. Eng. Geol. Environ. 79, 5455–

    5475. https://doi.org/10.1007/s10064-020-01900-0

Salah, M.K., Alqudah, M., El-Aal, A.K.A., Barnes, C., 2018. Effects of porosity and

    composition on seismic wave velocities and elastic moduli of lower cretaceous

    rocks, central Lebanon. Acta Geophys. 66, 867–894.

    https://doi.org/10.1007/s11600-018-0187-1

Salah, M.K., Alqudah, M., Monzer, A.J., David, C., 2020c. Petrophysical and acoustic

    characteristics of Jurassic and Cretaceous rocks from Central Lebanon. Carbonates

    and Evaporites 35. https://doi.org/10.1007/s13146-019-00536-w

Saripalliab, K.P., Sharmaa, M.., Bryantb, S.L., 2000. Modeling injection well

    performance during deep-well injection of liquid wastes. elsevier 227, 41–55.

Scanlon, B.R., Weingarten, M.B., Murray, K.E., Reedy, R.C., 2019. Managing Basin-

    Scale Fluid Budgets to Reduce Injection-Induced Seismicity from the Recent U . S

    . Shale Oil Revolution 171–182. https://doi.org/10.1785/0220180223

Schultz, R., Skoumal, R.J., Brudzinski, M.R., Eaton, D., Baptie, B., Ellsworth, W.,

2020. Hydraulic fracturing-induced seismicity. Rev. Geophys. 58, 1–43. https://doi.org/10.1029/2019RG000695

Schultz, R., Wang, R., 2020. Newly emerging cases of hydraulic fracturing induced seismicity in the Duvernay East Shale Basin. Tectonophysics 779, 228393. https://doi.org/10.1016/j.tecto.2020.228393

Segall, P., Lu, S., 2015. Injection-induced seismicity: Poroelastic and earthquake nucleation effects. J. Geophys. Res. Solid Earth 120, 5082–5103. https://doi.org/10.1002/2015JB012060

Simpson, D.W., Leith, W.S., Scholz, C.H., 1988. Two Types Of Reservoir-Induced Seismicity. Bull. Seismol. Soc. Am. 78, 2025–2040.

Stefanov, Y.P., Bakeev, R.A., 2015. Formation of flower structures in a geological layer at a strike-slip displacement in the basement. Phys. Solid Earth 51, 81–93. https://doi.org/10.1134/S1069351315040114

Steffen, R., Steffen, H., Wu, P., Eaton, D.W., 2015. Stress and fault parameters affecting fault slip magnitude and activation time during a glacial cycle. Tectonics 34, 2359–2366. https://doi.org/10.1002/2015TC003992

Talwani, P., 1997. On the Nature of Reservoir-induced Seismicity. Pure Appl. Geophys. 150, 473–492. https://doi.org/10.1007/978-3-0348-8814-1_8

Talwani, P., Acree, S., 1984. Pore pressure diffusion and the mechanism of reservoir-induced seismicity. Pure Appl. Geophys. PAGEOPH 122, 947–965. https://doi.org/10.1007/BF00876395

The Litani River Authority, 2021. The Qaraoun Lake & Dam [WWW Document]. URL

http://www.litani.gov.lb/en/?page_id=91

The World Bank, 2021. Lebanon Water Supply Augmentation Project (Bisri Dam) 1–
10.

Thoms, L.J., 1974. An introduction to mining, International Journal of Rock Mechanics
and Mining Sciences & Geomechanics Abstracts. https://doi.org/10.1016/0148-
9062(74)91552-6

Tiwari, D.K., Jha, B., Kundu, B., Gahalaut, V.K., Vissa, N.K., 2021. Groundwater
extraction - induced seismicity around Delhi region ,. Sci. Rep. 1–14.
https://doi.org/10.1038/s41598-021-89527-3

Valco, P., Economides, M., 2001. Hydraulic fracture mechanics. John Wiley & Sons,
Chichester.

Verdon, J.P., Stork, A.L., 2016. Journal of Rock Mechanics and Geotechnical
Engineering Carbon capture and storage , geomechanics and induced seismic
activity. J. Rock Mech. Geotech. Eng. 8, 928–935.
https://doi.org/10.1016/j.jrmge.2016.06.004

Vilarrasa, V., Carrera, J., Olivella, S., Rutqvist, J., Laloui, L., 2019. Induced seismicity
in geologic carbon storage 1 Introduction 2 Triggering mechanisms. EGU 1–14.

Wang, H.F., 2000. Theory of Linear Poroelasticity with Applications to Geomechanics
and Hydrogeology.

Wenzel, F., 2015. Induced Seismicity Using Dieterich's Rate and State Theory and
Comparison to the Critical Pressure Theory. Energy Procedia 76, 282–290.
https://doi.org/10.1016/j.egypro.2015.07.863

Wilson, M.P., Foulger, G.R., Gluyas, J.G., Davies, R.J., Julian, B.R., 2017. HiQuake: The Human-Induced Earthquake Database. Seismol. Res. Lett. 1–19. https://doi.org/10.1785/0220170112

Witherspoon, P.A., Gale, J.E., 1977. Mechanical and hydraulic properties of rocks related to induced seismicity. Eng. Geol. 11, 23–55. https://doi.org/10.1016/0013-7952(77)90018-7

Wyss, M., 1979. Estimating maximum expectable magnitude of earthquakes from fault dimensions. Geology 7, 336–340.

Yang, Z., Yehya, A., Iwalewa, T.M., Rice, J.R., 2021. Effect of Permeability Evolution in Fault Damage Zones on Earthquake Recurrence. J. Geophys. Res. Solid Earth. https://doi.org/10.1029/2021jb021787

Yehya, A., Rice, J.R., 2020. Influence of Fluid-Assisted Healing on Fault Permeability Structure. J. Geophys. Res. Solid Earth 125. https://doi.org/10.1029/2020JB020553

Yehya, A., Yang, Z., Rice, J.R., 2018. Effect of Fault Architecture and Permeability Evolution on Response to Fluid Injection. J. Geophys. Res. Solid Earth 123, 9982–9997. https://doi.org/10.1029/2018JB016550

Zang, A., Oye, V., Jousset, P., Deichmann, N., Gritto, R., McGarr, A., Majer, E., Bruhn, D., 2014. Analysis of induced seismicity in geothermal reservoirs - An overview. Geothermics 52, 6–21. https://doi.org/10.1016/j.geothermics.2014.06.005